N° d'ordre : D. U : 2800
EDSPI : 794

UNIVERSITE BLAISE PASCAL – CLERMONT II
U.F.R Sciences et Technologies

ECOLE DOCTORALE DES SCIENCES POUR L'INGENIEUR

THESIS

by

Zhenning DONG

to obtain the grade of

DOCTORATE Of UNIVERSITY

Specialty: Materials and components for electronics

Synthesis of GaAs nanowires and nanostructures by HVPE on Si substrate. Application to a microbial fuel cell based on GaAs nanowires.

Public oral defense on March 15, 2017, with the following commission:

Prof. Anna FONTCUBERTA I MORRAL	Reporting judge
Dr. (HDR) Lisa MICHEZ	Reporting judge
Prof. Vladimir G. DUBROVSKII	Examiner
Prof. Christine LEROUX	Examiner
Dr. (HDR) Christelle VARENNE	Examiner
Dr. (HDR) Fabrice AUDONNET	Examiner
Prof. Evelyne GIL	Thesis director
Dr. (HDR) Yamina ANDRE	Supervisor
Dr. (HDR) Pierre FONTANILLE	Supervisor

Acknowledgement

I would like to express my gratitude to all those who helped me during the writing of this thesis.

My deepest gratitude goes first and foremost to Prof. Evelyne Gil and Dr. (HDR) Yamina André, for their constant encouragement and guidance. They have walked me through all the stages of the writing of this thesis. Without their consistent and illuminating instruction, this thesis could not have reached its present form.

Second, I would like to express my heartfelt gratitude to Dr. (HDR) Fabrice Audonnet and Prof. Vladimir G.Dubrovskii, who contributed a lot for the final results in this thesis.

I am also greatly indebted to the professors and researchers at Institut Pascal: Mr. Dominique Castelluci, Dr. Guillaume Monier, Dr. (HDR) Christelle Varenne, Prof. Christine Robert-Goumet, Dr. (HDR) Pierre Fontanille, Prof. Agnès Trassoudaine, who have instructed and helped me a lot in the past three years. And a special gratitude for Mrs. Anne-Marie Gélinaud from 2MAtech, who gave her patient with me in front a black and white screen during three years.

I also owe my sincere gratitude to my friends, Geoffrey, Aymen, Réda, Elissa, who gave me their help and time in listening to me and helping me work out through these years.

Last my thanks would go to my beloved family for their loving considerations and great confidence in me all through these years. It was a great honor that my parents attended my thesis defense. Mengjie and Léo, this is all you.

Table of contents

Introduction

Predicting the evolution of semiconductor, Moore's law [1] has guided researchers for the last 50 years. Conventional semiconductor devices are generally based upon films of semiconductor materials, usually silicon, but the demand for improvement of the device performance requires the use of novel materials and non-planar device architectures [2].

III-V semiconductor nanowires show excellent electrical and optical properties in laterally confined geometry which is very promising for monolithic integration of photonic nanodevices with silicon. The vapor-liquid-solid (VLS) growth method enables sophisticated bottom-up design of morphologies and crystal structures influencing the resulting properties of nanowires. Gold catalyst droplets have been used to seed the III-V nanowire growth, however, gold may contaminate nanowires and is not well suited for integration with silicon electronic platforms. Consequently, there has been considerable effort in developing gold-free growth techniques where the VLS process is catalyzed by group III metals rather than gold.

The HVPE process, used during my PhD, has been developed in the Institut Pascal (former LASMEA and LPMC) since the 1970s for the growth of III-V planar layers. In the last decade, Institut Pascal has demonstrated the successful growth of GaAs nano-objects by SAG-HVPE (selective area growth-HVPE) [3] and GaAs nanowires by Au catalyst-assisted-HVPE [4] on GaAs substrate. GaAs nanowires will be the kernel of this report from their growth mechanism, crystallographic structure to their possible application in biology. The manuscript is organized into two chapters.

The first chapter introduces the state-of-the-art of self-catalyzed GaAs nanowires and nano-structures on silicon substrate. The growth of GaAs nanowires, especially self (gallium)-catalyzed GaAs nanowires on silicon, was the major objective my thesis. Gallium-catalyzed VLS growth of GaAs nanowires by molecular beam epitaxy (MBE) was introduced by Colombo *et al*. [5]. Since then, remarkable progress has been achieved toward MBE synthesis [6-10], theoretical understanding [11-14], tailoring of physical properties [8-10] and device implementation [15] of such nanowires. In particular, one can take advantage of well-developed techniques of SiO_x/Si preparation and processing that influence the nanowire morphology [6-7], obtain high crystal phase purity (zincblende (ZB)) [11], and modulate the nanowire diameter by tuning the As/Ga flux ratio [8]. In this competitive scientific context, chapter 1 gives first an overview of the physics of HVPE growth that will be implemented for the self-catalyzed growth of GaAs nanowires, which is then detailed in a second section. We report the first gallium-catalyzed HVPE growth of long (more than 10 µm) GaAs nanowires on Si(111) substrate with a high integrated growth rate up to 60 µm/h and pure zincblende crystal structure. The growth is achieved by combining a low temperature of 600 °C with high gaseous GaCl/As flow ratios. Then, we present a model that explains the peculiar growth mechanism in which the gallium droplets nucleate and rapidly swell on the silicon surface but then are gradually consumed to reach a stationary size. The last section of chapter 1 presents regular nanometer scale GaAs polyhedrons as by-products grown on the same substrate beside the nanowires. The initial nucleation of these structures is discussed and Wulff construction was built to model the crystallographic mechanism that governs the growth of these nano-polyhedrons. In the last part of this section, we have investigated the feasibility of hybrid HVPE/CBE or MOVPE processes.

Chapter 2 proposes the design of a Microbial Fuel Cell (MFC) prototype based on GaAs nanowire samples. The experiments presented in this chapter were performed within the project LabEx IMobS^3 (Innovative Mobility: Smart and Sustainable Solutions) under challenge 3, dedicated to the development of processes for the production of energy for mobility. Before my PhD, a collaboration had been initiated within Institut Pascal in order to combine the knowledge in physics, electronics, electrochemistry and biology. The work presented in this chapter is the outcome of a close collaboration between several researchers of Institut Pascal from GePEB (Process, chemical and thermodynamic Engineering, and Biosystems) department, and PHOTON (Photonics, Waves, Nanomaterials) department. We describe the functionality of a MFC which uses an active microorganism as a biocatalyst in an anaerobic anode compartment for the production of bioelectricity [16-19]. A brief history of MFC will be presented followed by the test of biocompatibility with GaAs electrode. The second part of the chapter is devoted to the assembling of the first MFC prototype and its electrochemical characterizations based on Nernst potential measurement. The working electrode chosen here is a commercial doped-

GaAs substrate in contact with a biological medium. The measurements allowed to validate the presence of an electron exchange between a bacterium biofilm and the GaAs doped-anode electrode at 2.0×10^{18} cm^{-3}. A standard electrochemical solution containing ions (Fe^{3+}/Fe^{2+}) at a controlled pH was used to identify the oxidation-reduction reactions that take place on the surface of the GaAs semiconductor. Finally, a last part is dedicated to measurements by impedance spectroscopy, to model the electron exchange at the interface either on the surface of a GaAs planar layer or on GaAs nanowires, in aqueous medium. The feasibility of *n*- and *p*-doping of these nanowires is also addressed.

References

[1] G. E. Moore, “Cramming more components onto integrated circuits, Reprinted from Electronics, volume 38, number 8, April 19, 1965, pp.114 ff.,” *Solid-State Circuits Soc. Newsl. IEEE*, vol. 11, no. 5, pp. 33–35, Sep. 2006.

[2] K. A. Dick, “A review of nanowire growth promoted by alloys and non-alloying elements with emphasis on Au-assisted III–V nanowires,” *Prog. Cryst. Growth Charact. Mater.*, vol. 54, no. 3–4, pp. 138–173, Sep. 2008.

[3] E. Gil, Y. André, M. R. Ramdani, C. Fontaine, A. Trassoudaine, and D. Castelluci, “Record high-aspect-ratio GaAs nano-grating lines grown by Hydride Vapor Phase Epitaxy (HVPE),” *J. Cryst. Growth*, vol. 380, pp. 93–98, Oct. 2013.

[4] E. Gil *et al.*, “Record Pure Zincblende Phase in GaAs Nanowires down to 5 nm in Radius,” *Nano Lett.*, vol. 14, no. 7, pp. 3938–3944, Jul. 2014.

[5] C. Colombo, D. Spirkoska, M. Frimmer, G. Abstreiter, and A. Fontcuberta i Morral, “Ga-assisted catalyst-free growth mechanism of GaAs nanowires by molecular beam epitaxy,” *Phys. Rev. B*, vol. 77, no. 15, Apr. 2008.

[6] F. Matteini, G. Tütüncüoglu, H. Potts, F. Jabeen, and A. Fontcuberta i Morral, “Wetting of Ga on SiO $_x$ and Its Impact on GaAs Nanowire Growth,” *Cryst. Growth Des.*, p. 150529153811003, May 2015.

[7] F. Matteini, G. Tütüncüoğlu, D. Rüffer, E. Alarcón-Lladó, and A. Fontcuberta i Morral, “Ga-assisted growth of GaAs nanowires on silicon, comparison of surface SiOx of different nature,” *J. Cryst. Growth*, vol. 404, pp. 246–255, Oct. 2014.

[8] G. Priante, S. Ambrosini, V. G. Dubrovskii, A. Franciosi, and S. Rubini, “Stopping and Resuming at Will the Growth of GaAs Nanowires,” *Cryst. Growth Des.*, vol. 13, no. 9, pp. 3976–3984, Sep. 2013.

[9] F. Matteini, V. G. Dubrovskii, D. Rüffer, G. Tütüncüoğlu, Y. Fontana, and A. F. I. Morral, “Tailoring the diameter and density of self-catalyzed GaAs nanowires on silicon,” *Nanotechnology*, vol. 26, no. 10, p. 105603, Mar. 2015.

[10] A. M. Munshi *et al.*, “Position-Controlled Uniform GaAs Nanowires on Silicon using Nanoimprint Lithography,” *Nano Lett.*, vol. 14, no. 2, pp. 960–966, Feb. 2014.

[11] V. G. Dubrovskii, G. E. Cirlin, N. V. Sibirev, F. Jabeen, J. C. Harmand, and P. Werner, “New Mode of Vapor−Liquid−Solid Nanowire Growth,” *Nano Lett.*, vol. 11, no. 3, pp. 1247–1253, Mar. 2011.

[12] F. Glas, M. R. Ramdani, G. Patriarche, and J.-C. Harmand, “Predictive modeling of self-catalyzed III-V nanowire growth,” *Phys. Rev. B*, vol. 88, no. 19, Nov. 2013.

[13] V. G. Dubrovskii *et al.*, “Self-Equilibration of the Diameter of Ga-Catalyzed GaAs Nanowires,” *Nano Lett.*, vol. 15, no. 8, pp. 5580–5584, Aug. 2015.

[14] J. Tersoff, “Stable Self-Catalyzed Growth of III–V Nanowires,” *Nano Lett.*, vol. 15, no. 10, pp. 6609–6613, Oct. 2015.

[15] P. Krogstrup *et al.*, “Single-nanowire solar cells beyond the Shockley–Queisser limit,” *Nat. Photonics*, vol. 7, no. 4, pp. 306–310, Mar. 2013.

[16] M. Rahimnejad, A. A. Ghoreyshi, G. Najafpour, and T. Jafary, “Power generation from organic substrate in batch and continuous flow microbial fuel cell operations,” *Appl. Energy*, vol. 88, no. 11, pp. 3999–4004, Nov. 2011.

[17] B. H. Kim, D. H. Park, P. K. Shin, I. S. Chang, and H. J. Kim, *Mediator-less biofuel cell*. Google Patents, 1999.

[18] H. J. KIM, S. H. MOON, and H. K. BYUNG, “A Microbial Fuel Cell Type Lactate Biosensor Using a Metal-Reducing Bacterium, Shewanella putrefaciens,” *J. Microbiol. Biotechnol.*, vol. 9, no. 3, pp. 365–367, 1999.

[19] N. Mokhtana, W. R. W. Daud, M. Rahimnejad, and G. D. Najafpouv, “Bioelectricity generation in biological fuel cell with and without mediators,” *World Appl. Sci. J.*, vol. 18, no. 4, pp. 559–567, 2012.

Chapter 1: Self-catalyzed growth of GaAs nanowires on silicon by hydride vapor phase epitaxy (HVPE)

1.1 Introduction

The growth of GaAs nanowires, especially self-catalyzed GaAs nanowires on silicon, is one of the goals of my thesis. In the last decade, Institut Pascal has demonstrated the successful growth of GaAs nano-objects by SAG-HVPE (selective area growth-HVPE) [1] and GaAs nanowires by Au catalyst-assisted HVPE [2] on GaAs substrate. The demand for integration of III-V semiconductors on a silicon platform has been constant since III-V structures have been routinely synthesized. Institut Pascal is the appropriate laboratory where growth of GaAs nanowires on silicon can be studied by means of the HVPE process. We will focus on the self-catalyzed growth of GaAs nanowires on Si. In this chapter, we give an overview of the physics of the HVPE process; then the experimental study of the self-catalyzed growth of GaAs nanowires by HVPE is detailed. The last part will address the theoretical modeling of GaAs nanowires growth.

1.2 Overview of the HVPE process

Vapor phase epitaxy (VPE) processes using chloride gaseous precursors were developed in the 1960s for the growth of the first III-V semiconductor epilayers [3-7]. Both the anion and cation elements are transported by chlorides in *halide* or *chloride* VPE, like $AsCl_3$ or PCl_3 and GaCl or InCl. For *Hydride* vapor phase epitaxy (HVPE), the element V is supplied by hydride gas such as AsH_3, PH_3 or NH_3. For HVPE, the III-Cl precursors are no longer obtained by introducing V-Cl_3 gas over group III liquid sources like in *halide* VPE, but are independently produced by flowing separate HCl fluxes over *in-situ* gallium and indium liquid sources. This independent supply was necessary for the growth of alloys such as $Ga_xIn_{1-x}As_yP_{1-y}$ with a large range of controllable compositions.

Pioneering groups, such as *Philips Laboratoire d'Electronique et de Physique Appliquée* in Europe, *V.S. Ban* and *C.H. Park's* groups in the United States, worked to develop the *halide* and *hydride* processes for the growth of III-V heterostructures [8-15]. However, the HVPE process faces a major technological limitation: as the elements III are produced inside the hot wall quartz reactor, related abrupt composition variations are difficult to manage, for any classic technical solutions used to quickly switch external gas sources cannot be implemented. Chloride VPE and HVPE were indeed considered as complex processes that lack versatility and reproducibility despite convincing demonstrations of the growth of GaInAs heterostructures with controlled interfaces [8] [16]. Also, it is very difficult to control de growth of alloys containing aluminum. The use of Cl-based aluminum precursors requires a severe control of the temperature profile along the reactor, the overall pressure, and the Cl composition in the vapor phase [17-18] to avoid parasitic deposition on the wall of the reactor. This is why HVPE has been progressively phased out in favor of metalorganic vapor phase epitaxy (MOVPE) and molecular beam epitaxy (MBE) for the growth of III-V low-dimensionality heterostructures.

Yet the use of chloride precursors gives HVPE its particular features, such as its fast growth property. With a 30-50 µm/h standard growth rate for condensation, high quality growth at 100 µm/h or record 300 µm/h was demonstrated for GaAs [19]. High growth rates are often associated with the use of high supersaturation conditions in the mind of growth physicists. Another statement is that HVPE is a near-equilibrium growth process, a notion that needs to be clarified. The fast growth property was the reason why HVPE had been reintroduced in laboratories at the end of the 1990s, for the growth of thick GaN epilayers to be used as quasi-substrates. Among some 44 000 papers published on the growth of III-V and nitride compounds since 1990, only 3.2% are related to HVPE, with 75% of those focusing on nitrides.

HVPE is the only VPE process operating close to the equilibrium of the deposition reactions as it will be discussed later. Its central advantages are: 1) the growth rate, which can be modulated at will to match the requirements for millimeter to submicrometer 2D layer growth; 2) the unequaled flexibility for selective and localized growth on patterned substrates; and 3) the possibility to exploit a huge growth anisotropy for shaping 3D structures with unusual aspect ratios. Apart from the obvious relevance driven by nitride compound issues, for which HVPE is a key process for implementing morphology-controlled SAG, HVPE deserves a renewed interest for the III-V. Whether for the growth of metamorphic buffers [20-21], photovoltaic applications [22], or monolithic integration on Si [23], HVPE, that involves a high mass input of precursors, is a suitable cost-effective and low polluting mass production process.

1.2.1 The HVPE reactor of Institut Pascal

First of all, to give a global vision and facilitate understanding of the following content, a reactor plan is given in Fig.1.1. The whole reactor is made of quartz, and it can be heated up to 900 °C. The HVPE reactor of IP is home-made. It has been chosen to divide it into three parts: the first part (shown in yellow) is the source zone where the liquid gallium holder (and the indium holder if needed) is placed. The H_2/N_2vector flow is introduced in this zone, as well as an additional HCl flow which is used to vary the supersaturation of the vapor phase. The second zone is the mixing zone, where the two III (GaCl/InCl) and V (AsH_3/PH_3) precursors meet and are mixed together. The doping elements are introduced in this central mixing area with gaseous SiH_4 and DEZ (di-ethyl zinc) as precursors for Si (n) and Zn (p) doping of III-V compounds. The source and mixing zones are connected through a manual-controlled drawer-valve. This valve actually separates the source zone from the mixing and the deposition areas, and prevents the early exposure of the substrate from unstable flux and unprepared precursors. The last part of the reactor is the growth zone, where the substrate is placed. The total flow and the geometry of the reactor are adjusted to ensure a homogeneous mixture in the vapor phase and a laminar flow over the substrate. The chloride precursors are produced at high temperature (> 700°C) in the source zone and they have to be transported to the growth area at high temperature. That is why HVPE facilities are hot-wall reactors. This requires smart technological solutions to fastly exhaust the gas flows and control the transient phases [24].

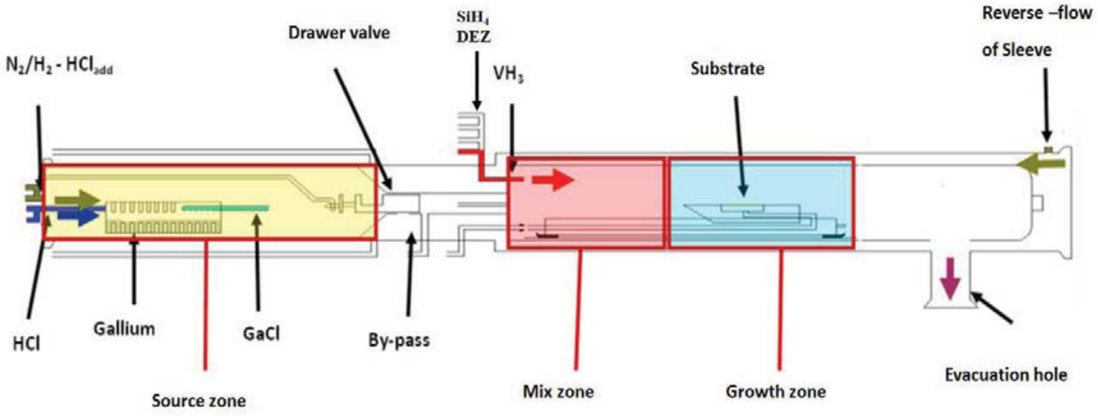

Fig.1.1: Schematic of the HVPE reactor of Institut Pascal for the growth of III-V semiconductors at atmospheric pressure.

To prevent parasitic deposition on the wall of the reactor, and so control the supersaturation over the substrate, the furnace temperature is not uniform throughout its length. A “bell” like temperature profile is used so that the temperature of the deposition zone is below the temperature of the central zone. Indeed, the deposition reaction of GaAs is exothermic, as all chemical reactions involving Cl-III and H_3-As or -P species. Deposition on the substrate is thus favored at the coolest location in the reactor, and not in the upward central zone set at a higher temperature. Six thermocouples are distributed in different areas of the furnace (source, mixing and growth zones) and allow the accurate control and setting of various temperature profiles.

1.2.2 Thermodynamics of HVPE

The growth of GaAs by HVPE involves gaseous GaCl molecules synthesized inside the quartz reactor by the use of a HCl flow reacting with a Ga liquid source at high temperature. The element V is supplied by arsine (AsH_3). When entering the hot-wall reactor, this hydride decomposes completely in the vapor phase at the usual profile temperature into $As_2 \leftrightharpoons As_4$ molecules [25] [26]. The global growth reaction for GaAs in H_2 atmosphere can be given as:

$$GaCl_g + \frac{1}{4}As_{4g} + H_{2g} \leftrightharpoons GaAs + HCl_g + \frac{1}{2}H_{2g} \tag{1.1}$$

Thermodynamics determines the driving force of the reaction and is only concerned with the energy of the system in the initial and final equilibrium states. It gives valuable informations: the temperature range when growth (or etching of the solid) occurs, the magnitude of the driving force, and the endothermic or exothermic property of the reaction. When a non-equilibrium situation is created by *supersaturating* the vapor phase in $GaCl_g$ and As_{4g} species, the system is driven to produce the solid. The maximum quantity of solid that can be produced is given by the amount that would re-establish the equilibrium. The supersaturation of the vapor phase γ is related to the thermodynamic force to restore equilibrium, that is the excess of chemical potential with respect to equilibrium of the reaction at temperature *T* [27-28]:

$$\Delta\mu = k_B T \ln\left[\frac{\left(\dfrac{\prod\limits_{reactants} a_{i,reactant}}{\prod\limits_{products} a_{i,product}}\right)}{\left(\dfrac{\prod\limits_{reactants} a_{i,reactant}}{\prod\limits_{products} a_{i,product}}\right)_{eq}}\right] = k_B T \ln(\gamma + 1) \tag{1.2}$$

where a_i is the chemical activity of species *i*, being $a_{reactant}$ (on the left side of Reaction (1.1)) or $a_{product}$ (on the right side of Reaction (1.1)). Chemical activities can be approximated by partial pressures for gaseous species. At equilibrium, the ratio of the activities is equal to the equilibrium constant of the reaction $K_{eq}(T)$, which gives for reaction (1.1):

$$K_{eq}(T) = \left(\frac{a_{HCl_g} a_{GaAs}}{a_{GaCl_g} a_{As_{4g}}^{1/4} a_{H_{2g}}^{1/2}}\right)_{eq} = \frac{[HCl]_{eq}}{[GaCl]_{eq}[As_4]_{eq}^{1/4}[H_2]_{eq}^{1/2}} \tag{1.3}$$

where $[i]_{eq}$ is the partial pressure of gaseous species *i* at equilibrium; $a_{GaAs} = 1$ for partial pressures in bar. We can write $K_{eq}(T)$ as a function of $\Delta G(T)$, the Gibbs free energy of the reaction at temperature T:

$$K_{eq}(T) = \exp\left(\frac{-\Delta G(T)}{kT}\right) \tag{1.4}$$

Then, the supersaturation γ is simply calculated as follows:

$$\gamma + 1 = \frac{[HCl]K_{eq}(T)}{[GaCl][As_4]^{1/4}[H_2]^{1/2}} \tag{1.5}$$

where *[i]* is the growth partial pressure of species *i*. Whether you consider Eqn (1.2) or Eqn (1.5) for interpretation, a null supersaturation means that the partial pressures in the reactor are those that promote a perfect equilibrium with the substrate. Such a stationary state can be achieved experimentally. A positive supersaturation implies that the reactants-to-products ratio of the partial pressures in the reactor is higher than the ratio at equilibrium.

Return to equilibrium is achieved by producing the solid. This corresponds to an excess of chemical potential with respect to equilibrium. HVPE is an amazing process because the reverse situation can be actually controlled: one can promote an inverse return to equilibrium (i.e., an etching of the substrate) by increasing the partial pressure of HCl in the reactor. HVPE reactors are often equipped with an independent line of additional HCl flow, which is used to vary the supersaturation parameter (see Fig. 1.1). The most powerful parameters for varying the supersaturation are the temperature and additional HCl.

Keq(T) is typically calculated from the thermodynamic data of the heat capacity of the species involved in the reaction at temperature *T*, that give the Gibbs free energy difference Δ*G(T)* between standard reactants and products. Within this framework, we can now discuss the notion of near-equilibrium process. According to Stringfellow's work [29-30], MOVPE and MBE exhibit Δ*G(T)* that is approximately eight times higher than for HVPE at 1000 *K*. As shown in Fig. 1.2, comparing with the extremely non-equilibrium technique like MOVPE (also for MBE), the thermodynamic driving force for growth (i.e., the chemical potential difference between the liquid/or gaseous and solid phases) by LPE and HVPE is relatively small.

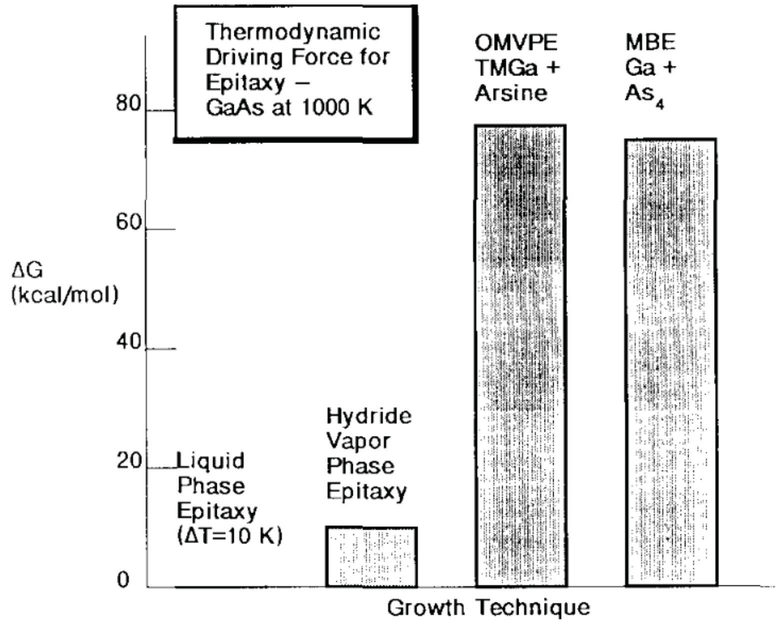

Fig. 1.2: Estimated thermodynamic driving force, Gibbs free energy difference between reactants and products, for several epitaxial growth processes. All calculations are for the growth of GaAs at 1000 K [29].

One point of view is to say that when the thermodynamic driving force for growth is small, then the process operates at near-equilibrium conditions: thermodynamics governs or limits growth. If we look at the experimental results, a wide range of growth rates, from 3 to more than 100 µm/h, can be obtained by immediate influence of an increase (or a decrease) of the vapor phase supersaturation. On increasing the supersaturation, the dechlorination frequency is high enough to avoid kinetic limitation; the return to equilibrium, which produces the solid, then takes place quickly [18] [31]. On decreasing the supersaturation, a reversible process occurs at the interface due to the volatility of the chlorides. That is supposed to characterize a near-equilibrium process, which has the interesting possibility of modulating the growth rate by drawing from variations of the mass input rate of the reactants. Hereby, HVPE should be able to match the requirements for growing structures from the micrometer scale (including several tens of microns) down to the nanometer scale.

If we consider supersaturation values, according to Stringfellow, MOVPE can be controlled by thermodynamic factors despite high supersaturation of the input vapor phase: near-equilibrium conditions may prevail near the solid–vapor interface because of mass transport limitation to the substrate surface. In that case, the growth is considered to proceed at near-equilibrium because there is a small supersaturation interacting with the surface. In the HVPE system, kinetics (surface reaction rates) and mass transport are fast enough to establish equilibrium at all times; this is true whatever the supersaturation of the vapor phase is, either low or high. HVPE growth is driven to equilibrium, which gives the maximum amount of solid that can be produced.

The Gibbs free energy difference that sustains the stationary state between solid GaAs, vapor composed As_2/As_4, and volatile GaCl elements at 1000 K is about 450 cal/mol. To activate growth in the HVPE system, a free-energy driving force ranging from 3500 cal/mol to some 7000 cal/mol is sufficient. In other words, standard low supersaturation conditions ($\gamma \leq 5$) up to medium supersaturation conditions ($\gamma \approx 30$) are needed for HVPE.

Thermodynamics does not provide information about the time required to restore equilibrium, neither does it identify the various steps involved toward the lowest energy state, nor the rates of the step processes. A kinetic study is necessary, even if it is difficult to achieve for such a dynamic complex system with inhomogeneous phases, provided it has been proven that the growth regime is indeed governed by *surface kinetics*. As a matter of fact, whatever the material, the growth rate exhibits a strong dependence on the temperature [3] [7] [27] [32-33] and substrate orientation [3] [7] [32], which denotes that the HVPE growth is mainly limited by surface kinetics. So, it is necessary to discuss about HVPE kinetics modeling in order to understand the physics of HVPE growth.

1.2.3 Kinetics modeling of HVPE

Pioneering work was performed by R. Cadoret, who applied the theory of rate-limited processes to HVPE growth [34]. The model was revisited for a generalization of the model of Burton, Cabrera and Frank (BCF) of step flow epitaxial growth in multicomponent systems for both reversible (HVPE) and irreversible (MOVPE) surface reactions [28] [35]. The model decomposes the global growth reaction into adsorption steps of elements V and III, a dechlorination step where several mechanisms are proposed as a function of the composition of the vapor phase, and surface diffusion steps.

The most important feature is the build-up of a stable chemisorbed V-IIICl layer after adsorption of group V elements on vacant sites of element III of the surface. The next step corresponds to the chlorine desorption: it is the slowest, so it determines the kinetics of the whole process. Two dechlorination mechanisms have been identified for GaAs growth [36-37]. They can be described as i) desorption of the Cl atom as HCl_g with the help of H_{2g}, and ii) desorption of Cl as $GaCl_{3g}$. This second mechanism takes place at low growth temperature or high GaCl partial pressure, as it involves a second GaCl adsorption layer on top of GaCl ad-species on the surface. The temperatures and vapor phase compositions that were used for the growth experiments presented in my PhD work, are those corresponding to growth governed by the first H_2 mechanism.

Adsorption and desorption fluxes of each identified species are determined after statistical thermodynamic analysis of the surface-vapor dynamics. Equations related to the conservation of matter for each species allow one to write the surface diffusion fluxes of the ad-species as a function of the net adsorption rate and their disappearance in the dechlorination reaction. The vertical growth rate is then written by considering the time needed for covering a terrace in the quasi-static assumption (stationary steps) upon incorporation of crystal units to the steps, either on vicinal substrates or on exact (001) orientation from emerging etch pit density (EPD). Mass transfer is taken into account by computing a one-dimensional (1D) boundary model, in which the thickness of the diffusion boundary layer is the same as the velocity gradient thickness of the Poiseuille regime, which corresponds to the standard mean global gas velocity conditions in HVPE reactors [36] [38].

We now describe the kinetic modeling generally discussed above for GaAs growth: mathematic calculations and schemes from a microscopic point of view.

Arsenic atoms are produced by the AsH_3 molecules decomposition. AsH_3 molecules as introduced into the HVPE reactor cracked into As_{2g}/As_{4g} molecules for temperature greater than 600°C, according to the following reactions:

$$AsH_3 \leftrightharpoons \frac{1}{2}As_{2g} + \frac{3}{2}H_{2g} \qquad (1.6)$$

$$\frac{1}{2}As_{2g} \leftrightharpoons \frac{1}{4}As_{4g} \qquad (1.7)$$

We have mentioned that all GaAs growth experiments reported in this manuscript were governed by the dechlorination kinetics of the H_2 mechanism, which is presented schematically in Fig 1.3. Consider a reference gallium (100) plane. In this simple model, the gallium atoms are covered by arsenic atoms on which the GaCl molecules are adsorbed to give a layer of AsGaCl molecules. Then, each adsorbed GaCl loses its chlorine atom (Cl) by hydrogen desorption. The overall reaction of GaAs deposition HVPE can thus be divided into three steps:

$$2V + As_{2g} \leftrightharpoons 2As \quad \text{and} \quad 4V + As_{4g} \leftrightharpoons 4As \qquad (1.8)$$

$$As + GaCl_g \leftrightharpoons AsGaCl \qquad (1.9)$$

$$AsGaCl + H_{2g} \leftrightharpoons AsGa_c + HCl_g + \frac{1}{2}H_{2g} \qquad (1.10)$$

The index g indicates gaseous species, c is for incorporated crystal. The adsorbed species carry no index and V represents a vacant site on the surface.

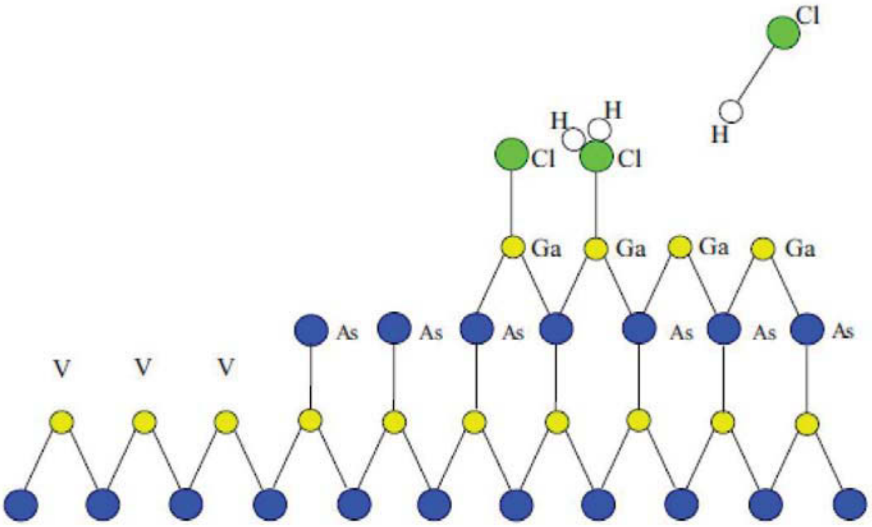

Fig 1.3: Scheme of H_2-AsGaCl ad-species dechlorination mechanism, V is a vacant site.

We now present a phenomenological model based on R. Ramdani's thesis [39]. This model gives the mathematical expression of the growth rate on GaAs (100) facet.

The kinetic modeling takes into account the adsorption flux J_{+i} and desorption flux J_{-i} of each element, and their surface diffusion flux J_{di} towards the incorporation sites at the steps on the surface (shown in Fig. 1.4).

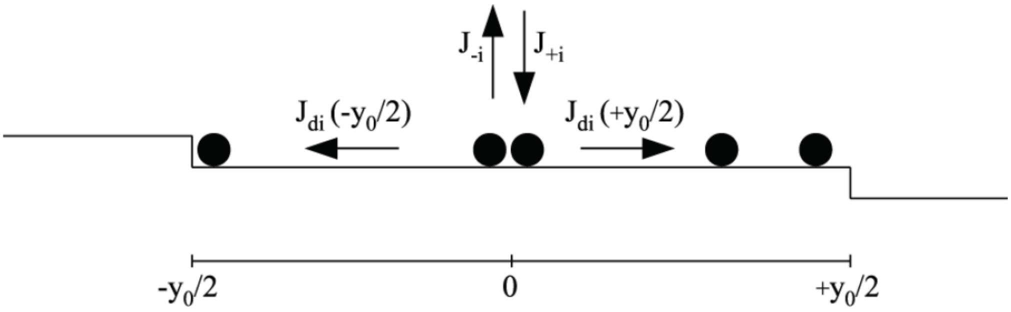

Fig 1.4: Scheme of the surface processes for the step-flow growth modeling on a vicinal substrate presenting terraces of width equal to y_0.

Adsorption flux of element i is written as $J_{+i} = k_{+i}\, F_i\, \theta_{vacant}$ (1.11)

with

F_i: adding material, considered as element i's partial pressure,

θ_{vacant}: the surface coverage in vacant sites,

k_{+i}: the kinetic constant, written as

$$k_{+i} = C_{+i}(T) exp\left(\frac{-E_{+i}}{k_B T}\right) \quad \text{and} \quad C_{+i} = \frac{1}{\sqrt{2\pi m_i k_B T}} \qquad (1.12)$$

with the pre-exponential C_{+i} term being the classical Hernst-Knudsen term.

Desorption flux of ad-species i is written as $J_{-i} = k_{-i}\, \theta_i$ (1.13)

with θ_i: the surface coverage of occupied sites with i type ad-species,

and k_{-i} the kinetic constant where $k_{-i} = C_{-i}(T) exp\left(\frac{-E_{-i}}{k_B T}\right)$

and $C_{-i} \propto \prod z$ (1.14)

expressed from the partition functions z of the species involved in the desorption process.

The net adsorption flux of As and GaCl elements can thus be written as a function of the difference between their respective adsorption and desorption fluxes:

$$J_i = J_{+i} - J_{-i} \qquad (1.15)$$

where

for reaction (1.8) $J_{As} = J_{+(As)} - J_{-(As)}$ (1.16) for reaction (1.9) $J_{As-GaCl} = J_{+(As-GaCl)} - J_{-(As-GaCl)}$ (1.17)

The net flux of AsGa is dominated by the dechlorination reaction (1.10) as:

$$J_{AsGa} = J_{+(AsGa)} - J_{-(AsGa)} \quad (1.18)$$

The equation of conservation of matter for element i allows to link its surface diffusion flux and the surface-vapor dynamics of element i as:

$$div(J_{di}) = J_i - J_{i+1} \quad (1.19)$$

J_{di} represents the diffusion flux of ad-species i towards one step, J_i and J_{i+1} are the net adsorption fluxes of species i, as involved in reactions. This equation means: what diffuses on the surface is what is present on the surface. What is present on the surface for species i depends on the net adsorption flux (adsorption − desorption) J_i of species i according to reaction i, and how species i disappears from the surface because it is involved in reaction $i+1$ where species $i+1$ adsorbs on species i according to the net adsorption flux J_{i+1}.

That is:

$div(J_{d2}) = J_2 - J_3 = (J_{+2} - J_{-2}) - (J_{+3} - J_{-3})$ for species $2 = As$

As adsorbing on vacant site of the surface − As disappearing because covered by GaCl

$div(J_{d3}) = J_3 - J_4 = (J_{+3} - J_{-3}) - (J_{+4} - J_{-4})$ for species $3 = AsGaCl$

GaCl adsorbing on As − AsGaCl disappearing because of Cl desorption

Then for (R_4), there is only one term:

$div(J_{d4}) = J_4 = (J_{+4} - J_{-4})$ for species $4 = AsGa$

As we have two unknowns: the concentration C_{AsGaCl} of species AsGaCl (acting as source of GaAs) and the concentration C_{AsGa} of species GaAs, then we need two equations:

$$J_3 - J_4 = div(J_{d3}) \quad (1.20)$$

$$J_4 = div(J_{d4}) \quad (1.21)$$

In this model, the diffusion of ad-species is considered as faster than the progression of steps (considered as stationary according to the quasi-static assumption).

J_{di} are expressed by Fick's law considering the surface concentration C_i of ad-species i (with $C_i = N_S\theta_i$, N$_s$ is the number of sites per surface unit) and D_i as diffusion coefficient of ad-species i:.

$$J_{di} = -D_i \frac{\partial C_i}{\partial y} \quad (1.22)$$

We introduce the adsorption v_{+i} and desorption v_{-i} frequencies as:

$$v_{\pm i} = \frac{J_{\pm i}}{C_i} \tag{1.23}$$

These frequencies are illustrated in Fig 1.5 for GaAs crystal.

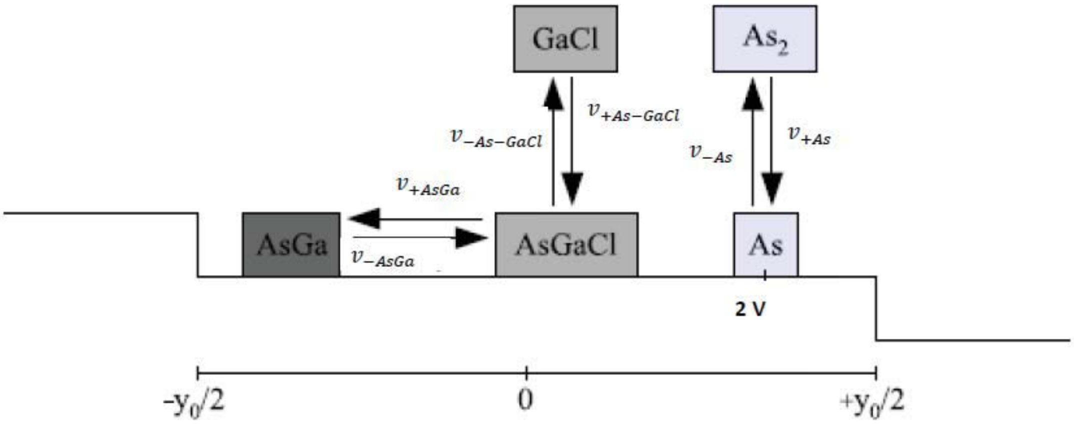

Fig 1.5: Schematic steps of GaAs growth from As_{2g} and $GaCl_g$. Adsorption and desorption frequencies of As and GaCl element were represented as v_{+As}, v_{-As} , $v_{+As-GaCl}$ and $v_{-As-GaCl}$ (from reactions 1.9 and 1.10), and v_{+AsGa} as dechorination frequency, v_{-AsGa} as chlorination frequency (equation 1.11).

That allows to obtain the following system of coupled equations:

$$\upsilon_{+3}C_{As} - \upsilon_{-3}C_{AsGaCl} - (\upsilon_{+4}C_{AsGaCl} - \upsilon_{-4}C_{AsGa}) = -D_{AsGaCl}\frac{\partial^2 C_{AsGaCl}}{\partial y^2}$$

$$\upsilon_{+4}C_{AsGaCl} - \upsilon_{-4}C_{AsGa} = -D_{AsGa}\frac{\partial^2 C_{AsGa}}{\partial y^2} \tag{1.24}$$

The growth rate V is determined by considering the time needed for covering the terraces. The coverage of terraces occurs because the steps move forward:

$$V = \frac{h}{t} = h\frac{\dot{y}}{y_0} = \frac{\Omega}{y_0} \times \left[-J_{di}\left(-\frac{y_0}{2}\right) + J_{di}\left(+\frac{y_0}{2}\right)\right] \tag{1.25}$$

with h the step height, $t = \frac{y_0}{\dot{y}}$ the time for covering one terrace, Ω the molecular volume of GaAs, and J_{dAs-Ga} the diffusion flux of As-Ga ad-species to the step.

Equation (1.25) can be written as a function of the concentration of AsGa:

$$V = \frac{\Omega}{y_0} \times \left[D_{AsGa} \frac{\partial c_{AsGa}}{\partial y}\bigg|_{-\frac{y_0}{2}} - D_{AsGa} \frac{\partial c_{AsGa}}{\partial y}\bigg|_{+\frac{y_0}{2}} \right] \tag{1.26}$$

The resolution of system (1.24) gives the concentration of AsGa, which allows to solve equation (1.26) after fitting experimental growth rate points [40]. As a result, the variation of the growth rate of GaAs as a function of the temperature is shown in Fig.1.6 (a): it follows a typical *bell curve*. At low temperature, growth is limited by the desorption, decomposition (that is dechlorination) and surface diffusion steps, which are inhibited. The surface is saturated with undecomposed AsGaCl species. This low temperature domain is where kinetics limitation is restrictive; it is the part described as a kinetically controlled regime by Shaw [41].

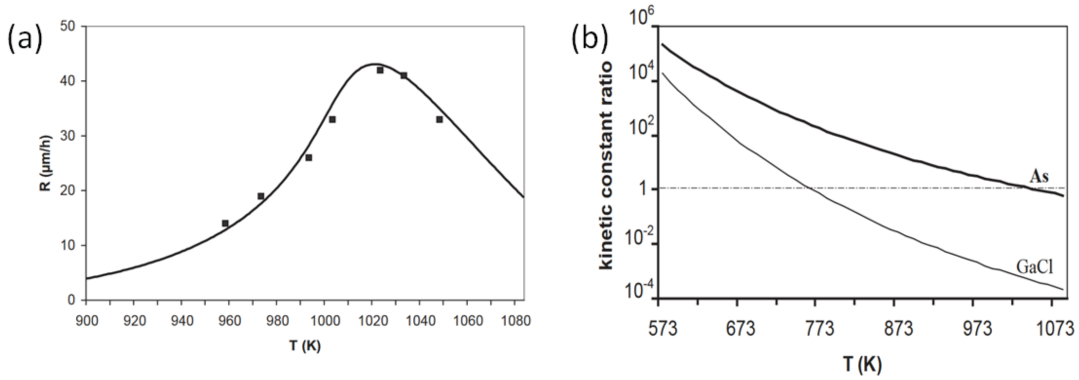

Fig.1.6: (a) (001) GaAs growth rate R in µm/h as a function of the temperature T for standard experimental conditions (III/V=4.5, γ=4). The squares are the experimental points; the full line is the computed theoretical curve according to the modeling described in [36]. (b) Variations of the adsorption/desorption kinetic constant ratio k+i/k-i for GaCl (thin solid line) and As (thick solid line) as a function of T. The kinetic constants are part of the adsorption $J_{ads} = k_{+i}[i]\theta_v$ and desorption $J_{des}= k_{-i}\theta_i$ fluxes of species i = GaCl or As, with [i] being the partial pressure of gaseous species i, θ_v the surface coverage ratio in vacant sites, and θi the surface coverage ratio of ad-species i. The k+i/k-i ratio gives the contribution of the microscopic states involved in the dynamic surface-vapor system [36]. The actual Jads/Jdes ratio should include the input mass of species i ([i]), which ensures sufficient adsorption of GaCl up to 1040 K.

When the temperature increases, desorption is favored; there is no further blocking of the adsorption sites as the thermal-activated dechlorination step is enhanced. Growth rate normally increases up to a maximum that takes place at 1023 K, which is predicted by the thermodynamic study. At high growth temperatures, HVPE exhibits the thermodynamically controlled growth regime and the growth rate is determined by the mass input rate of the reactants [41]. On the high temperature side of the curve, thermodynamics foretells sublimation of the solid, which is indeed observed with a dramatic fall of the growth rate, where Ga desorption (through GaCl) becomes significant. As a matter of fact, the adsorption/desorption kinetic constant ratio for GaCl is two orders of magnitude lower than the equivalent ratio for As, which is consistent with the high Ga-Cl binding energy (Fig.1.5 (b)). Arsenious-related processes are not limiting for the growth of (001) GaAs, which is governed by the adsorption of GaCl. The shaping of 3D structures with various morphologies is carried out under the kinetically controlled regime (low-temperature side of the bell curve), where the growth rates on various crystallographic planes differ as a consequence of the variations of the adsorption/desorption fluxes and dechlorination frequency from one face to the other for given identical experimental conditions.

An overview of the thermodynamics and kinetics of HVPE growth has been discussed in this section, focusing on GaAs crystal. These physical considerations will be useful to discuss growth of GaAs nanowires and micro- and nano-polyedrons, as we now move to the presentation of the self-catalyzed growth of such structures.

1.3 Self-catalyzed growth of GaAs nanowires: state of the art

In this section, we present the HVPE growth of GaAs nanowires by self-catalyzed, i.e., Ga-catalyzed, vapor-liquid-solid (VLS) growth. This HVPE investigation is new, for Institut Pascal is the only laboratory developing HVPE for GaAs nanowire growth in the world. The study also brings an interesting contribution to VPE processes, see MOVPE, when it comes to overcome the issues related to creating a liquid phase from a complex chemical vapor. Some basic questions in regards to nanowires are first clarified briefly.

1.3.1 Why investigating nanowires?

Nanowires show quasi-one-dimensional geometry which exhibits a high anisotropy between their diameter and length. Nanowires have received significant attention in the last decade for their unique physical and (opto)electronic properties, which may find commercial applications in various devices and systems. These intrinsic properties are related to their one-dimensional structure, and make them different from planar epitaxial layers.

We can resume the merits of III-V nanowires in three points:

(1) Stress relaxation property for high crystalline quality

One of the major advantages of III-V nanowires compared to 2D layers is that they can be grown on high lattice mismatch-substrates, even presenting a high thermal expansion coefficient difference, while maintaining a very high structural quality [40] [42]. F. Glas [43] and Ertekin [44] both showed that for a certain percentage of misfit between the substrate/nanowire materials, there is a critical diameter of the nanowire below which it should be dislocation-free. The most extreme example could be the growth of high quality InAs nanowires on silicon substrate with a lattice mismatch of about 11.6% where the maximum epitaxial nanowire diameter is 26 nm [45].

(2) Development of devices with a new geometry

Nanowires offer a versatile platform in designing active devices. 1D geometry makes it possible to consider new core/shell type heterostructures in addition to the usual axial heterostructures known for 2D layers. From a geometrical point of view, radial heterostructures of high form factor provide larger active area for the same amount of substrate surface. This will permit to use the large interface of the core/shell active surface, and increase the emission efficiency per unit area of the substrate surface. One example would be self-assembled quantum dots in core-shell GaAs/AlGaAs nanowires which have shown blue-shifted emission spectrum [46].

(3) High aspect ratio

The high aspect ratio, e.g., the surface/volume ratio of nanowires, makes them very sensitive to their environment. With a high contact interface with surroundings, nanowire based devices are perfect candidates for sensor applications [47-48].

1.3.2 Growth of nanowires: VLS and self-catalyzed mechanism

(1) The main two growth routes: VLS and SAG

In the last decade, III-V nanowires have been mainly grown by MBE and MOVPE, either by vapor-liquid-solid (VLS) growth or selective area growth (SAG).

The first synthesis of semiconductor wires has been published by Wagner and Ellis of the Bell laboratories in 1964 [49-50]. They demonstrated the growth of one dimension (1D) silicon wire (Fig. 1.7) on silicon substrate, with a diameter of hundreds of nanometers, showing no dislocation along the axial direction. The experiment was carried out by vapor phase epitaxy (VPE), with pre-deposition of a metallic impurity on the silicon surface, where $SiCl_4$ was used as a precursor for silicon. Wagner and Ellis proposed a new mechanism of crystal growth, called VLS for vapor-liquid-solid [49]. This mechanism involves first the creation of metallic droplets on the surface. These droplets act as preferential sites to pyrolyze the $SiCl_4$ precursor. The solidification of Si at the droplet/substrate interface takes place after accumulation of Si atoms in the metallic droplets. Later, the VLS mechanism has been studied by Givargizov in 1975 [51], who expounded the catalytic function of the metallic droplet. This catalytic effect lowers the potential barrier of pyrolysis, and the potential barrier of nucleation at the vapor/droplet and droplet/substrate interfaces. Owing to these works, one could imagine devices based upon the use of these new high aspect ratio and good crystal quality wires. However, interest for (III-V)-nanowires really began at the end of the 1990s, when their unique electronic and optical properties were thoroughly addressed, with a view to optoelectronic and sensor applications. The very early GaAs nanowires were grown in 1995 by T. J. Trentler *et al.* by implementing a low temperature Solution-Liquid-Solid method [52]. The first VLS growth of GaAs nanowire was presented by A. Morales and C. Lieber in 1998 [53].

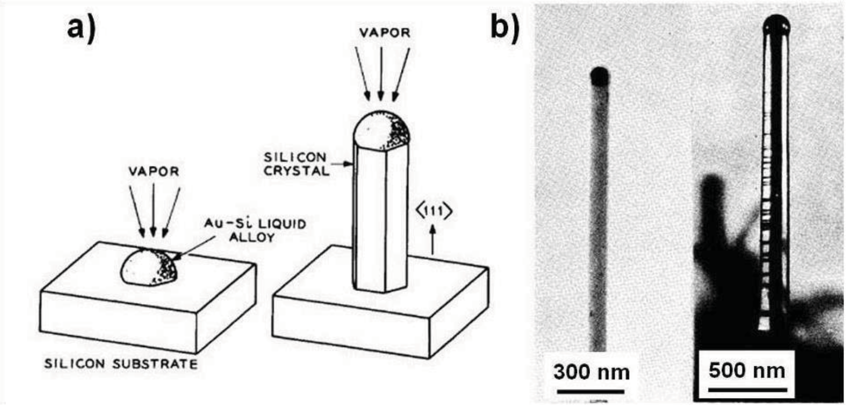

Fig.1.7: (a) VLS mechanism of silicon nanowire growth. (b) Scanning electron microscope (SEM) images of the first silicon nanowires [50].

In parallel, selective area growth (SAG) is another common process used for the growth of nanowires. Selective epitaxial deposition of silicon and gallium arsenide were achieved in the 1960s [54-56]. Lithography can be used to pattern the substrate before growth, providing predefined locations for nanowire formation. Substrate patterning is also efficient to control the nanowire density and arrangement [57]. For SAG implemented by

MOVPE, it was found that the growth selectivity was strongly depending on the substrate temperature, the chamber pressure, and the local geometry of the mask windows and the surface treatment [58-60]. Two mechanisms were proposed to explain the local growth enhancement observed at the edges of stripes or pyramidal objects of the earliest SAG-MOVPE studies: surface diffusion [61] and vapor-phase diffusion [62]. In the 2000s, SAG-MOVPE has been beneficiating from years of experimental data and theoretical models, until pioneering and remarkable work was done by K. Tomioka *et al.* [63-64]. The authors used a seven-step sequence growth approach for the epitaxial growth of GaAs nanowires on Si, as shown in Fig. 1.8.

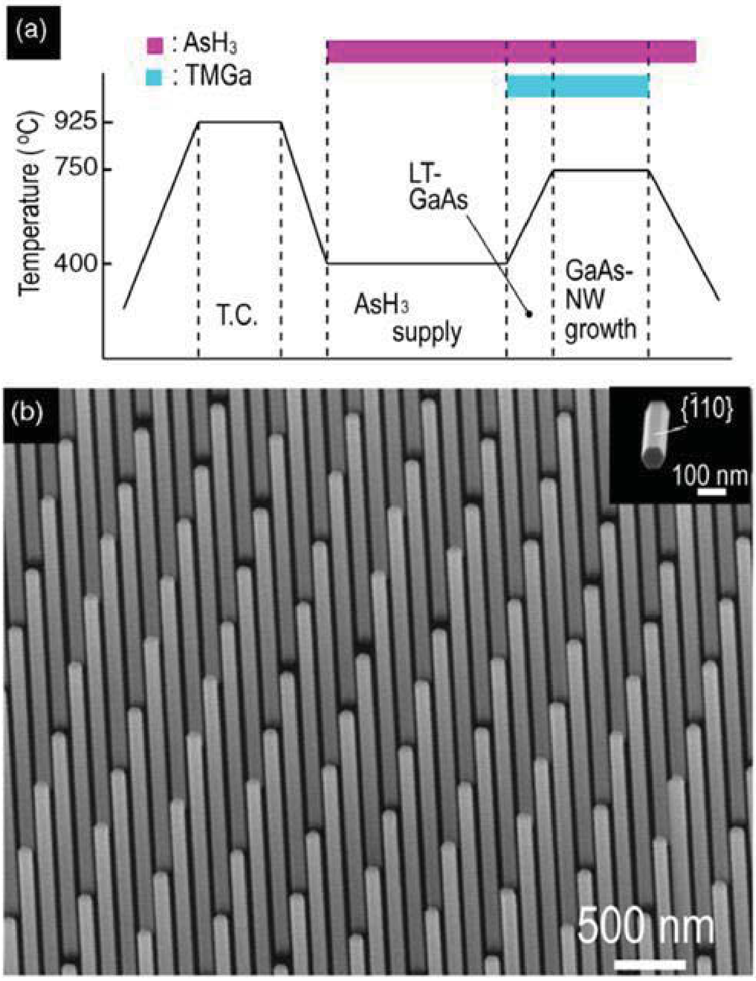

Fig. 1.8: (a) Growth sequence for GaAs nanowires grown on Si(111) substrate. T.C. stands for thermal cleaning and LT means low temperature. (b) 45°-tilted view of a SEM image of a GaAs nanowire array on a Si(111) surface [63].

This was the first demonstration of regular arrays of GaAs nanowires vertically aligned on Si(111) substrate.

(2) Integration of III-V nanowires on silicon

The demand for introducing non-Si channel materials such as III-V for nMOS and Ge for pMOS, expends in 22 nm technology [65]. Heteroepitaxial growth of GaAs on Si is then needed, opening the path to monolithic integration of GaAs-based optoelectronic devices on Si [66]. Silicon is the most widely used semiconductor material [67]. The advantages of silicon with respect to the III-V are well known: abundant reserves on earth; comparatively cheap process; large size substrate fabrication due to its mechanical stability; a native oxide as an insulator and high hole mobility to make high speed p-channel field-effect transistors (FETs). Of course, silicon has two obvious drawbacks as its indirect band gap, which limits the use for active optical device applications; another one is its low electron mobility, which influences the performance of the n-channels FETs. Most of the III-V materials do not have these shortcomings.

That is why today epitaxial researchers are trying to find a way to merge Si as substrate and electronic platform with III-V semiconductors, with a view to the monolithic integration of structure devices. As we have mentioned in 1.3.1, the main difficulties for the heteroepitaxy of GaAs on silicon are related to the lattice mismatch and the thermal coefficient difference. Because of the film-substrate lattice mismatch ($\varepsilon_0 = 4.0\%$ for the GaAs/Si system), GaAs films can have dislocation densities as high as 10^9-10^{10} cm^{-2}. The difference in the thermal expansion coefficients ($6.63\times10^{-6}\,K^{-1}$ for GaAs, and $2.3\times10^{-6}\,K^{-1}$ for Si) also promotes the generation of a great quantity of dislocations and cracks in the GaAs film on cooling down after the epitaxial growth [68].

As we mentioned in section 1.3.1, nanowires can be grown on high lattice mismatch-substrates. The critical diameter for coherent epitaxial growth of nanowire decreases with lattice mismatch ε_0 [43] and equals 24-26 nm for InAs/Si ($\varepsilon_0 = 11.6\%$), 36-38 nm for InP/Si ($\varepsilon_0 = 8.1\%$), and 100 nm for GaAs/Si. Therefore, the nanowire geometry is very promising for monolithic integration of III-V compounds on silicon, especially for GaAs on silicon [69]. VLS growth of semiconductor nanowires assisted by a metal is highly mature. The crucial issues have been the control of the crystalline quality and impurity concentration [70]. With regard to purity, one has tried to avoid the use of gold as catalyst for III-V nanowires growth. Gold is a fast diffusing metal that significantly harms the properties of semiconductors [71]. While it is ideal for general studies, gold and many other catalyst metals may be problematic for device applications because they form electrically active defects in the semiconductor nanowire [72]. Defects are due to the unintentional catalyst contamination, as the example shown in Fig. 1.9 for InAs nanowires [73]. Also, pre-deposition of foreign metal catalysts is considered as an extra-step for the growth of III-V nanowires on silicon substrate leading to a more expensive growth process. Indeed, a self Ga-catalyzed process for GaAs nanowires growth on silicon would be very interesting to get rid of metal-related issues and simplify the process route.

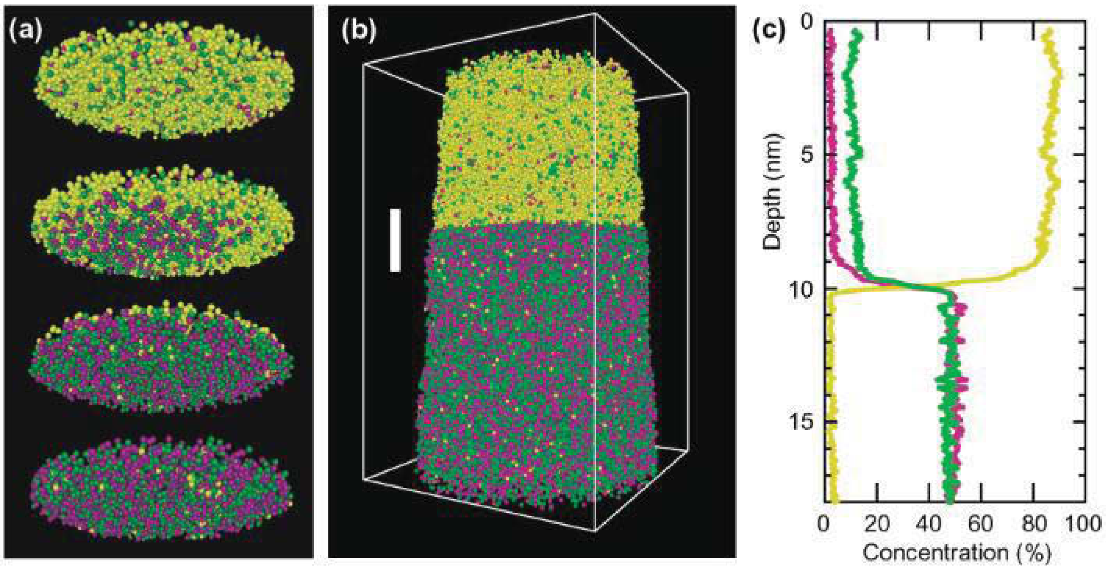

Fig. 1.9: Catalyst nanowire interface in three dimensions, which shows the diffusion of gold catalyst in InAs nanowires. (a) 1-nm-thick slices through the nanowire over the region defined by the white bar in b. The diameter of the slices is 10 nm. (b) A 14x14x23 nm^3 reconstruction of an InAs nanowire tip showing Au catalyst particle at the top. (c) One-dimensional composition profile plotted along the growth axis and through the catalyst/nanowire interface. The plotted composition is a radially averaged value within a 4-nm-diameter cylinder centered in the middle of the nanowire [73].

1.3.3 Growth of self-catalyzed GaAs nanowires by MBE

Gallium-catalyzed VLS growth of GaAs nanowires by molecular beam epitaxy (MBE) was introduced by A. Fontcuberta i Morral *et al.* [74-75]. As shown in Fig. 1.10, GaAs nanowires were obtained on (111)B and (001) GaAs wafers covered with 6 nm-layer of SiO_2, at 630 °C with an As_4 partial pressure of $8x10^{-7}$ mbar and a Ga rate of 0.25 Å/s. The key parameters governing the Ga-assisted growth of GaAs nanowires by MBE are: the oxide layer which provides the sites for nucleation, and offers the wetting characteristics which favor the formation of Ga droplets; the arsenic flux controlled by the As_4 pressure, which limits the axial growth rate; the Ga adatoms flux at the Ga droplets which increase the growth rate. This work also concluded that the radial growth was 2 orders of magnitude lower than the axial growth rate [75].

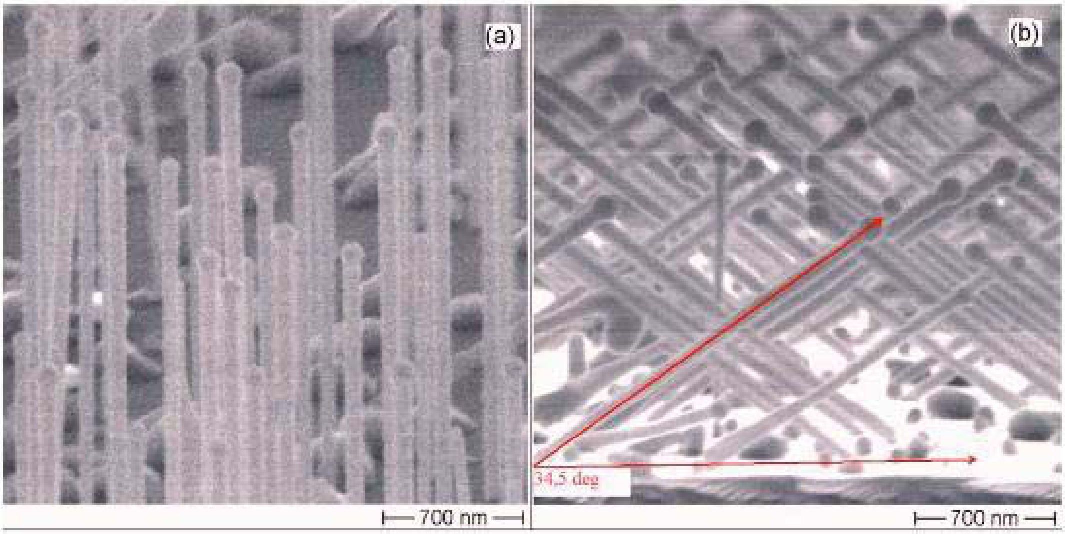

***Fig. 1.10:** Nanowires obtained on SiO_2-coated GaAs wafers with two different surface orientations: (a) (111)B and (b) (001) [74].*

This pioneering and outstanding study opened the way to self-catalyzed growth by MBE. Since then, remarkable progress has been achieved. The control of the thickness and the properties of the SiO_2 oxide remains an important parameter for the self-assisted growth of GaAs nanowires. Matteini *et al.* [76] described the relations between the nature and thickness of the oxide layer on Si substrate, and the self-catalyzed growth of GaAs nanowires (Fig. 1.11). One can conclude that the thickness of the oxide layer SiO_2 is a key factor for the growth of self-catalyzed nanowires, the optimized oxide thickness is between 0.8 to 1.2 nm. The influence of the oxide layer features will be discussed when self-catalyzed growth is implemented by HVPE in section 1.4.1 and 1.5.1.

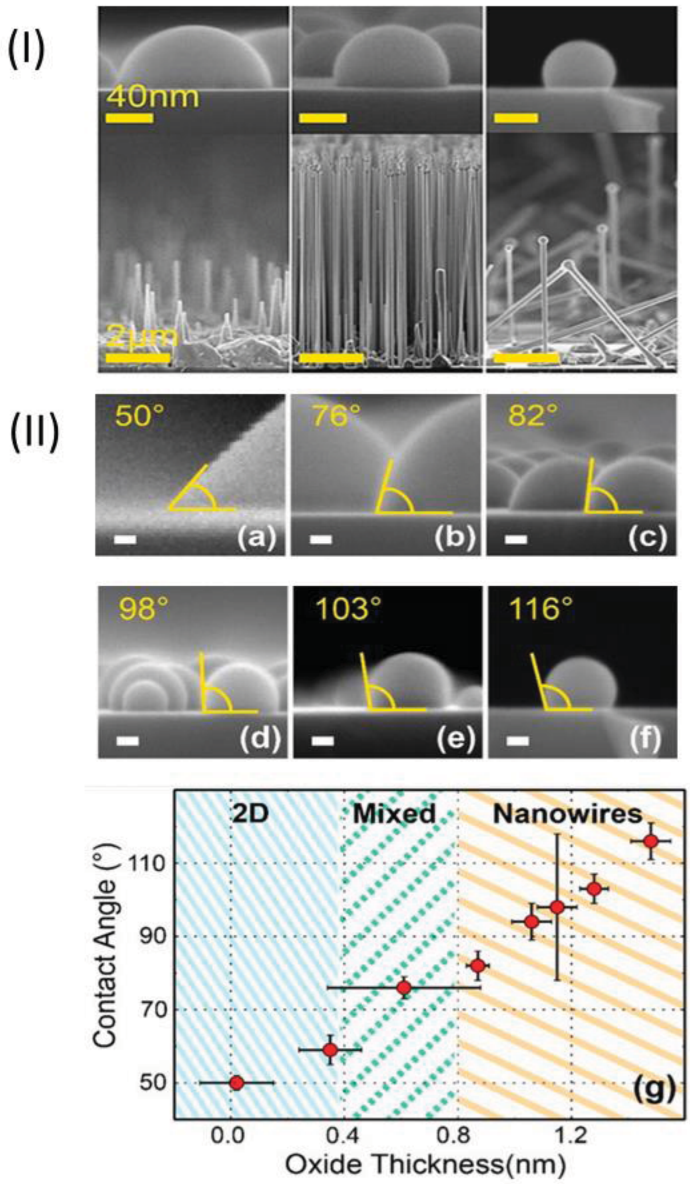

Fig. 1.11: (I) SEM micrographs of the wetting of the Ga droplets formed by Ga deposition at 640 °C for 5 min on different surface states of silicon, and morphology of the corresponding nanowires. (II) SEM micrographs of the wetting of the Ga droplets formed by Ga deposition at 640°C for 5 min on oxide thicknesses of 0.1 (a), 0.6 (b), 0.9 (c), 1.1 (d), 1.3 (e), and 1.5 nm (f). The scale bar is 20 nm. In (g) the increase of the contact angle at increased oxide thicknesses is represented. The progress of the contact angle is correlated to the evolution from 2D growth, to mixed 2D-elongated structures without droplets, to nanowire growth [76].

Another remarkable work on the growth of self-catalyzed GaAs nanowires was published by Priante *et al.* [77]. It has been shown the possibility of interrupting and resuming at will the self-catalyzed growth of GaAs nanowires by MBE (seen in Fig. 1.12).

Supplying only gallium allowed one to tune the starting diameter of the nanoparticle and to induce a nanowire regrowth starting with the same diameter of the underlying nanowire. This could be exploited to grow nanowires with controlled axial and radial heterostructures by simply stopping and resuming the axial growth.

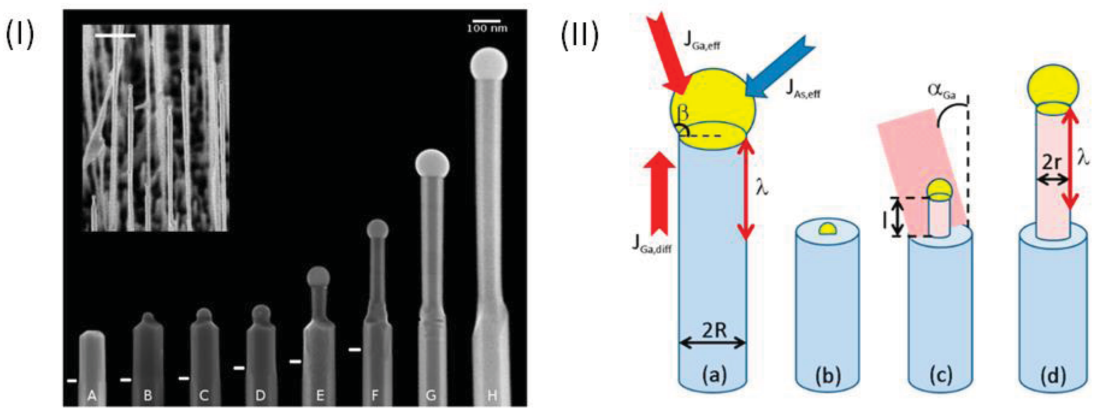

Fig. 1.12: (I) SEM images picturing the topmost region of GaAs nanowires observed just after the consumption of the Ga nanoparticle (A) and following subsequent exposures to Ga and As beams for 30 (B−D), 60 (E), 150 (F), 300 (G), and 420 s (H). The three different nanoparticles observed in nanowires coming from the same sample (B−D) give an indication of the local fluctuations in the process. A marker at the left of each wire indicates the position of the diameter discontinuity. The inset shows a tilted view (45°) of a sample after regrowth for 150 s. The marker in the inset corresponds to 1 µm. (II) Schematic of the nanowire growth process. (a) Regular self-assisted growth, (b) nucleation of a Ga nanoparticle, and (c and d) nanowire regrowth [77].

Theoretical investigations of self-catalyzed growth have been performed by several groups. One of the pioneer works was achieved by A. Fontcuberta's group [75]. The group discussed theoretically an As-limited growth of GaAs nanowires. Growth involves the creation of nucleation sites in the SiO_2 layer which depends on the desorption rate and diffusion length of Ga adatoms on SiO_2. Ga adatoms can diffuse towards the GaAs regions, the atoms impinging on the surface should diffuse through the oxide and then along the nanowire sidewalls and to the tip of the nanowire to contribute to the growth of Ga droplet [75]. Schematics of the growth steps are shown in Fig. 1.13.

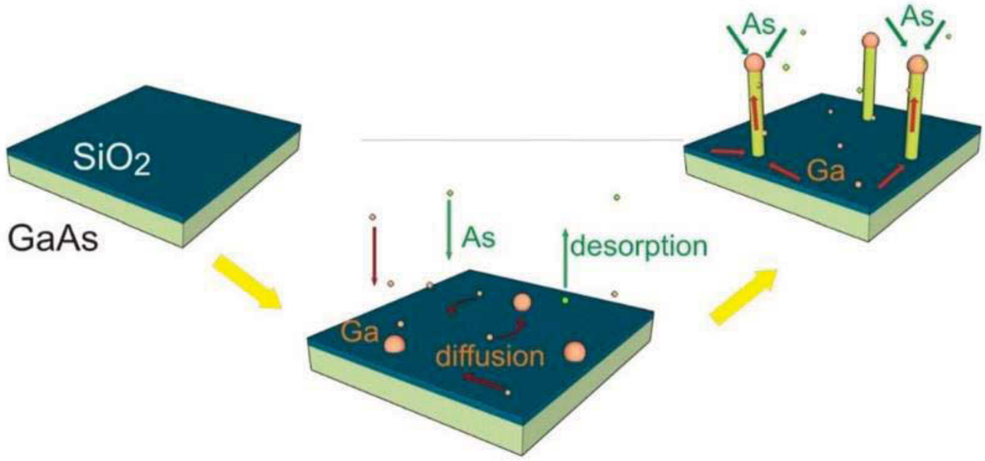

Fig. 1.13: Schematics of the growth steps of self-catalyzed nanowires. On the SiO_2, the seeds of GaAs nanowires nucleate and grow, being continuously fed by the Ga adatoms that diffuse from the neighboring SiO_2 surface, and form a droplet on top of the nanowires. The As_4 molecules impinging on the Ga top droplet contribute to the axial growth of the nanowires [75].

V.G. Dubrovskii *et al.* [78-79] and Sibirev *et al.* [80] provided theoretical models for the thermodynamics which govern the nanowires growth and surface energy. In Ref. [79], it is demonstrated that nanowire growth is metastable and controlled entirely by the growth kinetics. As for the crystal structure, one can model and predict the zinc-blende (ZB) and wurtzite (WZ) polytypism in III-V nanowires, and the critical radii for the transition between ZB and WZ. In 2010, V.G. Dubrovskii modeled in Ref. [81] the MBE growth of pure zincblende GaAs nanowires on Si (111). It is well known that the ZB structure is achieved only under sufficiently high As pressure by MBE and MOVPE [63] [82-86]. F. Glas and V.G. Dubrovskii demonstrated that the ZB phase takes place after the 2D nucleation of an island at the liquid-solid interface into the catalyst droplet, while nucleation at the triple phase (vapor-liquid-solid) line yields the WZ phase (Fig. 1.14).

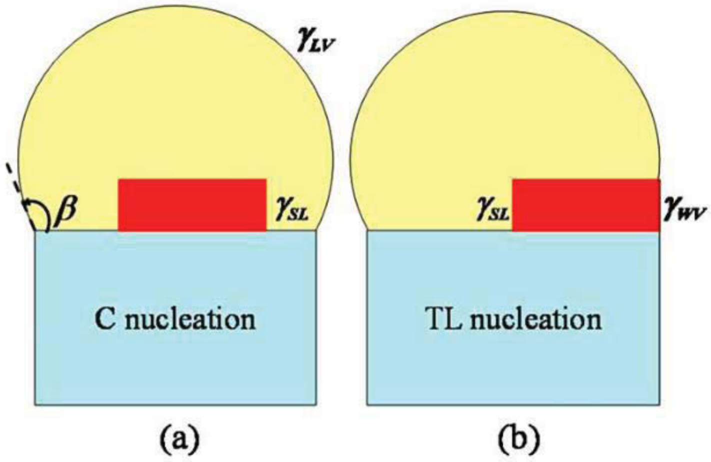

Fig. 1.14: Nucleation of a 2D island at the liquid-solid interface in the droplet (a) and at the triple phase line (TL) position (b). Nucleation at the TL position eliminates a part of preexisting liquid-vapor interface with effective energy $\gamma_{LV}\sin\beta$ and replaces it with the wire-vapor interface having energy γ_{WV} [81].

Today, with the knowledge brought by VLS growth quantitative models [87], one can take advantage of well-developed techniques for preparation of SiO_x/Si surface that influences the nanowire morphology [76] [83], obtain highly desired crystal phase purity (ZB phase) [78], and modulate the physical properties such as the nanowire diameters by tuning the As/Ga flux ratio [77] [88-89]. The elongation rate of Ga-catalyzed GaAs nanowires is determined by the arsenic vapor flux and is radius-independent for sufficiently large diameter of the droplets [75], which improves the length uniformity within the nanowire ensembles [90]. Furthermore, gallium droplets can self-equilibrate to a certain stationary size within a range of Ga/As flux ratios and this effect leads to narrowing the radius distribution of nanowires [72] [77] [91].

As a conclusion, the MBE process provides self-catalyzed GaAs nanowires on silicon with the highest crystal quality, the best spatial uniformity and a tunable morphology. What about VPE processes, that involve complex chemical precursors?

1.3.4 Self-catalyzed growth of GaAs nanowires by MOVPE

While indium-catalyzed VLS growth of InAs nanowires and InAs-based nanowire heterostructures have been successfully demonstrated by both MBE [92-93] and MOVPE [84] [94], Ga-catalyzed MOVPE growth of GaAs nanowires remains a very challenging task and does not produce structures with morphological and crystal phase perfections comparable to those obtained by MBE.

Breuer *et al.* [86] report the Ga-catalyzed growth of GaAs structures on Si(111) substrates using MOVPE (Fig. 1.15). GaAs nanowires were achieved with a V/III ratio of 1, using trimethylgallium (TMGa) and AsH_3. The oxide layer thickness was still proven an influent factor to control the nanowires density.

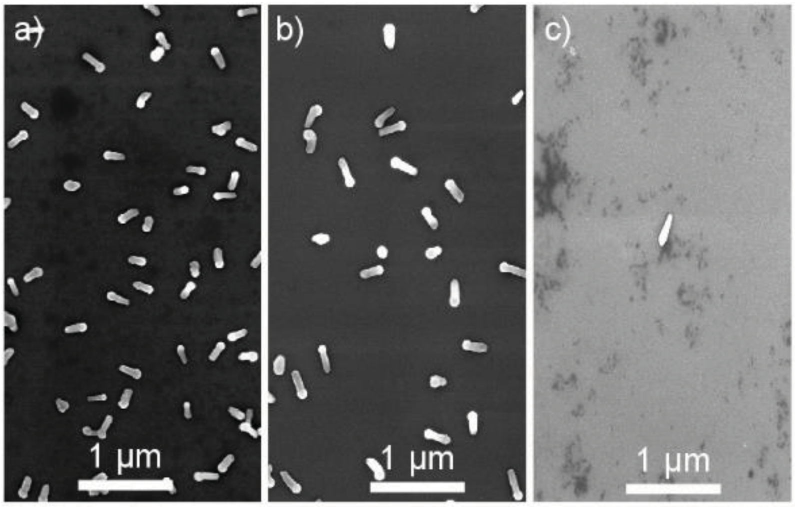

Fig. 1.15: SEM images (top view) of GaAs nanowires grown on Si/SiO_x using Ga droplets. Different SiO_x thicknesses, achieved by varying the SiH_4 flow of a) 3 sccm, b) 6 sccm, c) 9 sccm, resulted in various nanowires density [86].

Self-catalyzed growth of GaAs nanowires on GaAs substrate was reported by Ermez *et al.* [85] using TMGa and arsine as group-III and group V precursors. The growth took place at a relatively low temperature between 420 to 435 °C (Fig. 1.16).

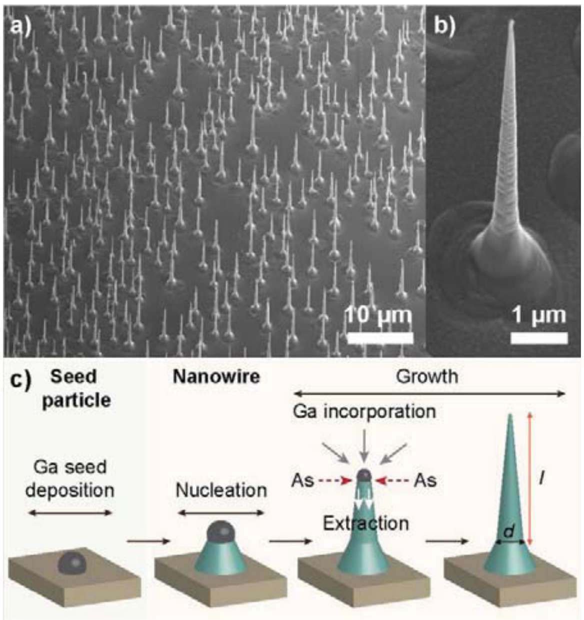

Fig. 1.16: (a) SEM image of a GaAs nanowires array showing the alignment of the nanowires on the GaAs (111)B substrate. (b) SEM image of a single nanowire taken at 45° tilt showing the nanowire morphology with two regions (base and nanowire) that have distinct tapering rates. (c) Nanowire growth schematic; in-situ Ga seed deposition is followed by nanowire nucleation and growth. The balance of Ga incorporation into the seed particle and Ga extraction from the droplet particle determines the tapering of the nanowire during growth. Nanowire length and diameter are denoted as l and d, respectively [85].

For VPE processes, the main challenge is related to the temperature required for cracking chemical precursors (such as organometallic precursors), combined with arsenic-rich atmosphere in the reactor. Such conditions do not favor both the initial nucleation and the further stability of the liquid gallium droplets [95-96]. Given these limitations, it is extremely difficult to find appropriate conditions for Ga-catalyzed VLS growth and GaAs nanowires obtained so far are limited in length (typically less than 1 µm) [86].

HVPE process has been proven as a cost-effective method for growing gold-catalyzed GaAs nanowires on GaAs substrates at a record elongation rate of more than 150 µm/h and with high crystal quality [2] [39] [97-99]. It is now the opportunity to test HVPE for self-catalyzed growth of GaAs nanowires on silicon substrate.

1.4 Self-catalyzed growth of GaAs nanowires by HVPE

Two types of Si substrates were used in the study, (1) Si (111) substrate with unpatterned native oxide; (2) patterned Si (111) substrate with SiN(100 nm)/SiO_2(20 nm) surface layers. The latter will be described in details in section 1.4.3.

The key steps for experimentally implementing GaAs growth on Si is: i) the preparation of the Si surface, ii) the wetting of the surface with Ga liquid droplets, iii) the nucleation of GaAs nanowires.

1.4.1 Chemical cleaning of Si substrates

As discussed previously in section 1.3.3, the Si surface and thus the thickness and the quality of the silicon dioxide are key parameters for the self-catalyzed growth of GaAs nanowires for either MBE or MOVPE. In this section, we discuss the chemical preparation of Si substrates. The surface was systematically analyzed by X-ray photoelectron spectroscopy (XPS) after HF chemical cleaning. XPS is a surface-sensitive quantitative spectroscopic technique that measures the chemical composition on the surface. XPS spectra are obtained by irradiating a material with a beam of X-rays while simultaneously measuring the kinetic energy and number of electrons that escape from the top 0 to 10 nm of the material being analyzed [100]. The thickness of the oxide layer was calculated with the spectra data.

6 inch Si (111) substrates with native oxide layer were cut into pieces of about 1 cm^2. They were cleaned with deionized water and 1% HF solution in an ultrasonic washing unit. Table 1.1 shows the XPS spectrum for various cleaning times. We chose Si_{2p} peak at 99.4 eV to analyze the variation of oxide layers, and the peak around 103.5 eV is the SiO_2 peak. The horizontal axis is the binding energy (eV), the vertical axis gives the intensity on counts per second (CPS) which varied in each measurement and is considered in arbitrary unity (a.u).

By calculating the surface ratio of $R = Si_{2p}\ oxide/Si_{2p}$ (first spectrum in Table 1.1, orange for $Si_{2p}\ oxide$ peak surface and blue for Si_{2p}), we can compare this ratio with the standard value and obtain a thickness range.

Cleaning method	XPS spectrum around Si_{2p} peak	Description
Si substrate cleaning with deionized water in ultrasonic cleaner	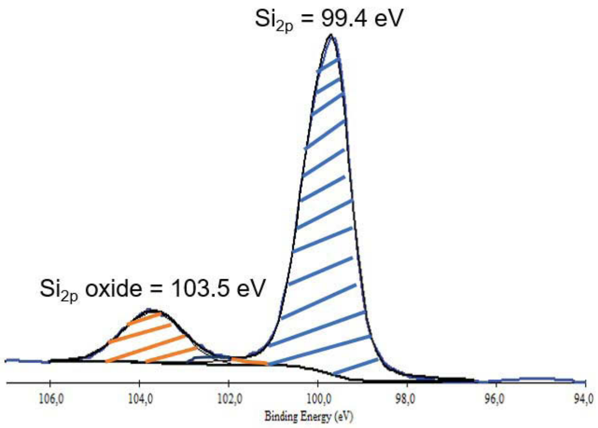	We can see clearly the SiO_2 peak at 103.5 eV. This peak represents a thickness of SiO_2 between 1.2 to 1.5 nm.
Si substrate cleaning with 1% HF during 10 s in ultrasonic cleaner	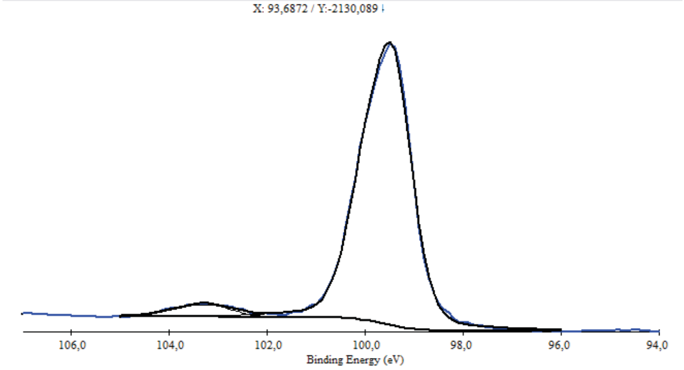	SiO_2 peak is dropped significantly; it represents a thickness of SiO_2 between 0.4 to 0.6 nm.
Si substrate cleaning with 1% HF during 30 s in ultrasonic cleaner	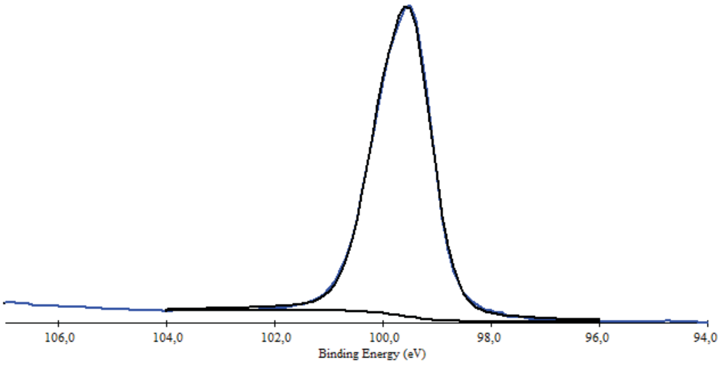	No SiO_2 peak observes in spectrum, oxide layer is eliminated.

Table 1.1: Different chemical cleanings of Si substrates with 1% HF solution (expect the first line) and their XPS spectrum.

From table 1.1, we can calculate that the etching rate of 1% HF on SiO_2 is about 0.1 nm per second. It takes about 12 to 15 s to eliminate the whole native oxide layer on the Si substrate. A slight re-creation of the 0.2 to 0.3 nm-oxide layer is observed during the transportation to the HVPE reactor. However, the chemical etching times must be much longer for self-catalyst growth on silicon. This is mainly to create more nucleation sites on the surface.

1.4.2 The formation of gallium droplets from $GaCl_g$ precursors

One must emphasize that Ga-catalyzed growth should not be implemented at the usual growth temperature of 2D planar GaAs epilayers (from 710 to 750°C), a temperature range that is also used for the Au-assisted growth of nanowires in the HVPE environment. For MBE and MOVPE, the temperature range used for self-catalyzed growth is between 550°C to 620°C or even lower [76] [82-83] [85] [89] [101]. Such a low temperature is necessary to limit the desorption of Ga adatoms from the oxide mask, and form liquid Ga droplets and optimize their diameter. There is a critical difference between HVPE and MBE/MOVPE. HVPE involves GaCl gaseous molecules, of which decomposition, i.e., dechlorination, is much more difficult from 600°C to 700°C. A thermodynamic calculation is necessary to predict the appropriate temperature range for the formation of liquid gallium droplets on the Si surface in the HVPE environment.

The possible chemical reactions of $GaCl_n$ decomposition are the following:

$$GaCl_g + \frac{1}{2} H_2 = Ga_l + \mathrm{HCl} \tag{1.28}$$

$$GaCl_{2g} + H_2 = Ga_l + 2\ \mathrm{HCl} \tag{1.29}$$

$$GaCl_{3g} + \frac{3}{2} H_2 = Ga_l + 3\ \mathrm{HCl} \tag{1.30}$$

$$2\ GaCl_g = GaCl_{2g} + Ga_l \tag{1.31}$$

$$3\ GaCl_g = GaCl_{3g} + 2\ Ga_l \tag{1.32}$$

$$3\ GaCl_{2g} = 2\ GaCl_{3g} + Ga_l \tag{1.33}$$

Thermodynamic calculations were conducted with equations 1.3 and 1.4 from Section 1.2.2. The theoretical decomposition efficiency of GaCl in reaction (1.28) is very low according to the numerical value of the equilibrium constant Keq, which is much smaller than 1 at 600 °C, and Keq rapidly decreases with increasing temperature (Fig. 1.17). This indicates that the equilibrium material balance is not in favor of liquid gallium when trying to deposit from GaCl gaseous molecules. The reactions (1.31-33) are slightly better than GaCl (1.28), but the value of Keq is still less than 1. The decomposition of $GaCl_2$ and $GaCl_3$ are extremely low as shown in Fig. 1.17, these species can be neglected.

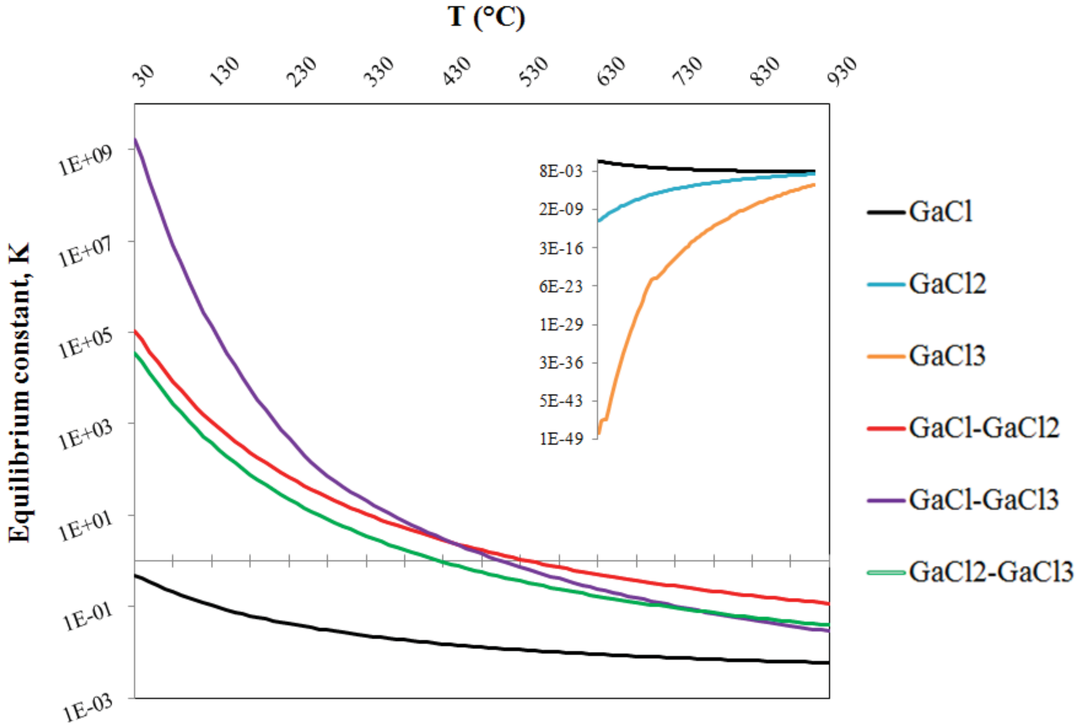

Fig. 1.17: Temperature dependence of the equilibrium reaction constants for dechlorination of various $GaCl_n$ gaseous precursors. Thermodynamic calculations show the preferred material balance for gaseous GaCl rather than liquid Ga, whatever the precursors.

It turns out that a high partial pressure input of GaCl is necessary to achieve the deposition of a few liquid gallium droplets on the substrate surface. A high partial pressure increases the supersaturation of reaction 1.28 and pushes the reaction to the production of liquid Ga. The growth temperature should not be the one used for the Au-assisted growth of GaAs nanowires by HVPE, that is T>700°C, which would yield evaporation of liquid gallium.

1.4.3 Preliminary test for GaAs growth on Si

The very first experiment of self-catalyzed growth of GaAs nanowires on Si, that we will call T(1), was performed at 670°C with the III and V fluxes usually used for Au-catalyzed growth of GaAs nanowires, that is 324 Pa for GaCl, 73 Pa for As_4 and 67 Pa for additional HCl. Si (100) and Si (111) substrates were etched chemically with 40% HF for 1 min. This intense etching guaranteed no oxide layer left and a rough surface with possible nucleation spots. These two substrates were transferred into the reactor. Heating up of the substrates from room temperature to 670°C under H_2 atmosphere took 20 minutes. Growth started when GaCl and As_4 (together with additional HCl) fluxes were supplied to the substrate zone. The III/V atomic ratio was 1 for the partial pressures of precursors of T(1).

SEM images of the post-growth surfaces of the (100) and (111) Si substrates are reported in Fig. 1.18.

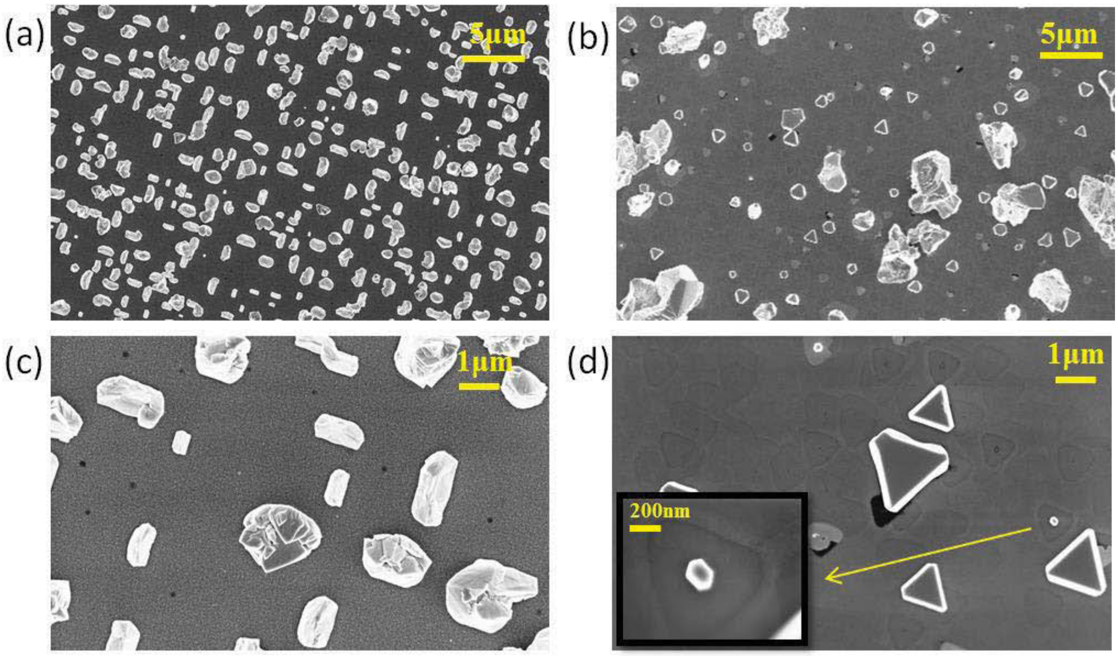

Fig. 1.18: SEM images of the post-growth surface of T(1) grown at 670 °C. (a) and (c) for Si (100); (b) and (d) for Si (111). Partial pressures were 324 Pa for GaCl, 73 Pa for As_4 and 67 Pa for additional HCl. The III/V atomic ratio was 1.

We can see that GaAs nano-objects grew successfully on both (100) and (111) Si substrates. The subselect part in Fig 1.18 (d) shows starting nuclei seed of a GaAs crystallite with a hexagon base and a half-sphere-like top. This could be the initial stage of the growth of a self-catalyzed nanowire. However, this type of structure is not present at high density on the surface. Most of the area of the surface is occupied by triangle micro-objects on Si (111), and rectangular crystals on Si (100). Epitaxial lateral overgrowth (ELO) should govern the growth of such 3D structures. The intense HF etching of the silicon substrates created holes in the nanometer-thick SiO_2 layer, from which ELO took place (see Fig. 1.18). T(1) showed 3D nucleation of solid GaAs micro-crystals, but no nanowires. This means that those specific preliminary experimental conditions and in particular the growth temperature of 670 °C, were not suitable for nanowire growth. Nevertheless, the feasibility of the growth of 3D GaAs objects through a condensation mechanism on Si (111) and (100) was demonstrated. We could then expect that self-catalyzed VLS growth should be possible by tuning both the atomic III/V ratio and the growth temperature in order to favor the formation of Ga droplets at the initial step. Before testing Ga-catalyzed growth from Ga direct wetting of Si substrate from GaCl precursors in the HVPE reactor, appropriate growth parameters for Ga-catalyzed GaAs nanowires were first determined on Si substrates with pre-deposited gallium droplets by MBE.

1.4.4 Pre-deposition of gallium droplets

In order to grow nanowires from a regular array of diameter-controlled gallium droplets on silicon, we used Si (111) substrates with pre-deposited gallium droplets prepared by MBE at the Center for Nanoscience and Nanotechnology C2N (ex LPN) of Marcoussis (France). Fig. 1.19 shows the SEM images of the surface after gallium deposition, and various annealings of the substrates in the HVPE reactor.

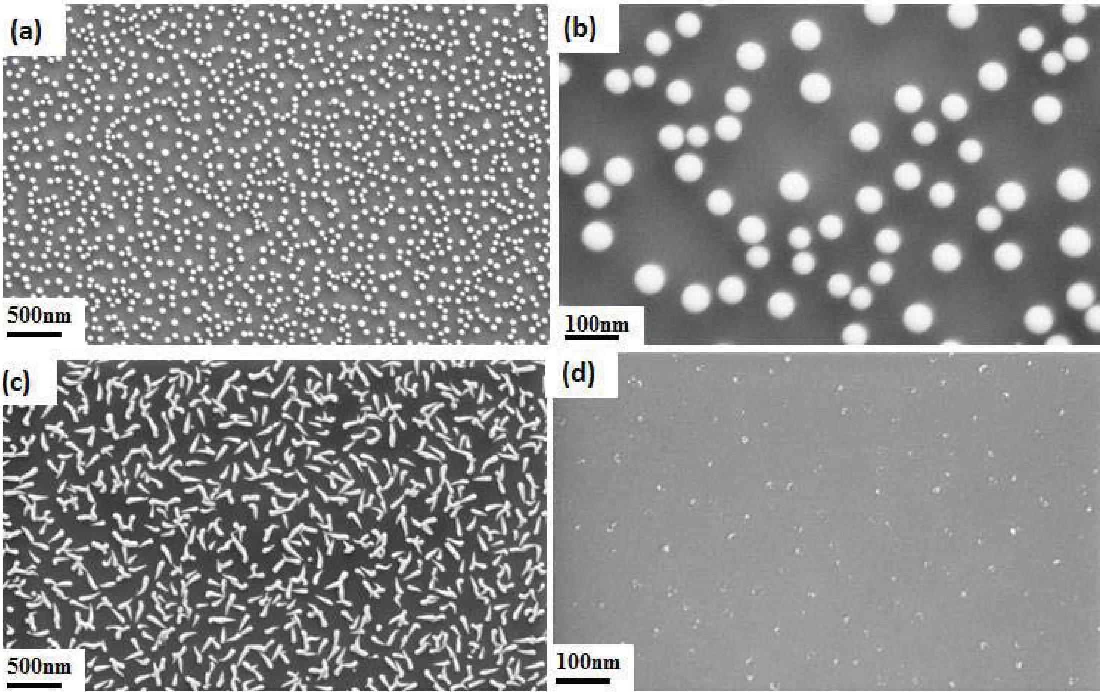

Fig. 1.19: SEM images of Ga droplets deposited by the C2N/LPN by MBE on Si (111) substrates ((a) and (b)). The average diameter of the Ga droplets is 50 nm. (c) Gallium droplets deformation after 10 min-annealing at 500°C in the HVPE reactor. (d) Left spot traces of gallium droplets after 10 min-annealing at 560°C in the HVPE reactor.

The first issue is related to the maximum annealing temperature that can be set while preserving the gallium droplets and preventing their evaporation in the HVPE reactor. Various annealing temperatures were tested, 400°C, 500°C, 530°C and 560°C. Ga droplets were found present on the Si surface until 530°C under hydrogen carrier gaz. The boiling point of liquid gallium is 2400°C. This contradicting phenomenon is mainly caused by the high saturating vapor pressures required with the H_2 ambiance in our reactor [95].

In order to stabilize Ga droplets pre-deposited in a foreign MBE reactor on the Si surface, we have designed a two steps process T(2) (Fig. 1.20). Step 1 at 500°C is a transient step which provides a protection for the gallium droplets before the temperature increases up to 600 °C for 4 mins. Step 2 corresponds to the normal growth as in T(1) previously described in Fig. 1.18 and 1.19 for 5 min.

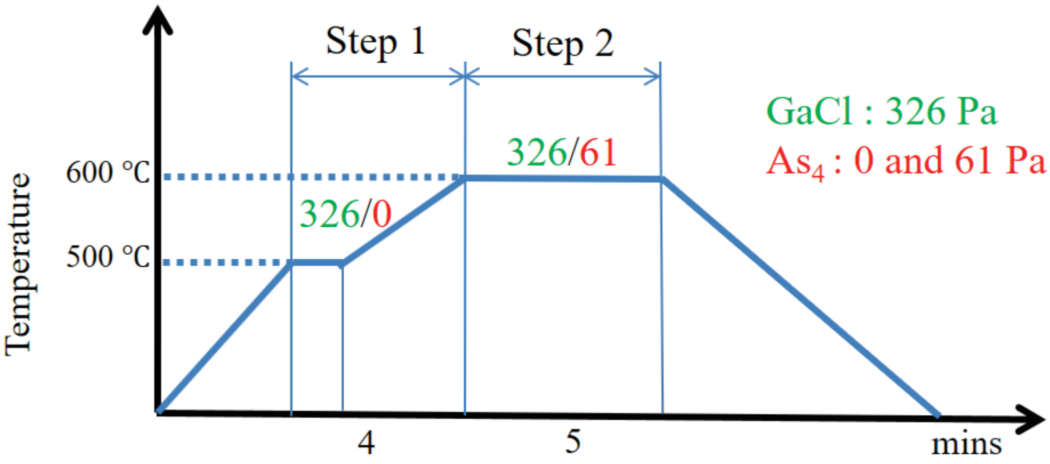

Fig. 1.20: Diagram of the two step-growth of experiment T(3) for Si (111) substrates with pre-deposited Ga droplets by MBE. HCl/Ga source flow is in green in Pascal, and As$_4$ flux is in red with the same unit.

The SEM images of post-grown substrates after T(2) experiments are shown in Fig. 1.21.

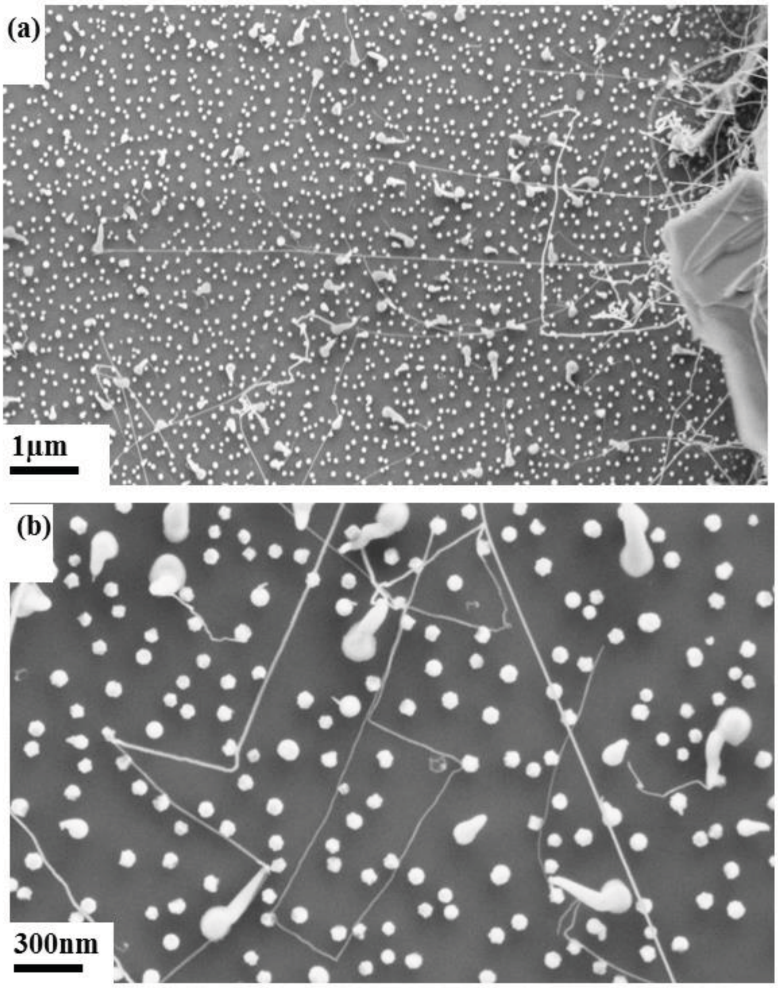

Fig. 1.21: SEM images of GaAs nanowires grown at 600 °C from pre-deposited Ga droplets after a two-step HVPE process (T(2) experiments - 5 min-growth). (a) Horizontal nanowire crawling on the surface; (b) few pear-like gallium droplets (by gathering effect of gallium at high temperature) with nanowires grown on the top.

The maximum elongation rate of the nanowires is 120 µm/h, and the extreme smallest diameter observed is 7 nm. Fig. 1.21 (a) shows horizontal nanowires clung to the surface with a maximum length of 8.5 µm. Fig. 1.21 (b) shows few pear-like gallium droplets which have nanowires grown from the top. We can see from Fig. 1.21(a) and (b) that most of the gallium droplets do not have nanowires grown; only the ones with pear-like shape have nanowires emerging from the droplet.

Most of the droplets were actually consumed under the As_4 flux after the first growth step of T(2). The As_4 flux should therefore be reduced to favor the growth of nanowires by VLS and prevent condensation of GaAs solid crystallites. In addition, gallium droplets are oxidized during the transfer from the C2N-LPN MBE chamber to the Institut Pascal HVPE reactor. Some papers mentioned that a mechanism of oxide-assisted growth of GaAs nanowires [102-103] may work. It is difficult to conclude whereas the growth mechanism described in Fig 1.21 is governed by self-catalyzed or oxide-assisted growth.

The pear-like base of the nanowires indicates that the III/V ratio must be increased to favor rich-gallium droplets. The fast growth rate of 120 µm/h, the extreme thin diameter of 7 nm, and a reasonable nanowire density proved the feasibility of Ga-catalyzed growth of GaAs nanowires by HVPE, with the specific features demonstrated previously for Au-catalyzed HVPE growth of GaAs nanowires under high mass input of precursors: high elongation rate, availability of thin diameter. That motivated us to develop a growth procedure base on *in-situ* deposition of Ga droplets in the HVPE reactor prior to growth.

1.4.5 Growth of nanowires on patterned Si substrate

From the previous study, one can estimate that: (1) patterned substrate could be used in order to facilitate the gathering of liquid gallium; (2) the growth temperature should be set to meet the two requirements: favor the decomposition of GaCl gaseous precursors and prevent the decomposition of gallium droplets; and (3) AsH_3 flux should be low to prevent the over-consumption of the elements III.

Within this framework, a 6 inch-pattern Si (111) substrate was used, cut into 1 cm^2 pieces for the growth experiments. The substrate was covered with a SiN (100 nm)/SiO_2 (20 nm) pattern on top of its surface. The structure is shown in Fig. 1.22:

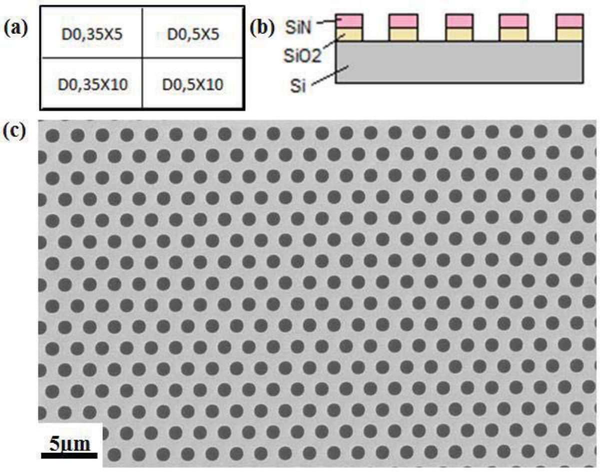

Fig. 1.22: Schematic of patterned Si (111) substrate. (a) Organization of ensembles of holes with their diameter and inter-center distance; 0.35×5 is for hole diameter of 0.35 µm and pattern period of 5. (b) Cross-section schematic of substrate, 20 nm of SiO_2 layers recovered by 100 nm of SiN. (c) SEM image of the (0.5×5) patterned zone.

Chemical etching was systematically applied during 7 minutes in 1% HF solution before each test in order to get rid of the first SiN layer, to preserve the SiO_2 mask and to clean the inside of the holes.

Several multi-steps HVPE growth procedures have been performed with patterned and non-patterned Si (111) substrates at different temperatures and vapor phase compositions. A summary of the most representative results obtained during the study are reported in Table 1.2, as a function of the relevant critical parameters: the growth temperature, the III/V ratio, the use of patterned or non-patterned substrates and the efficiency of the multi-steps growth process.

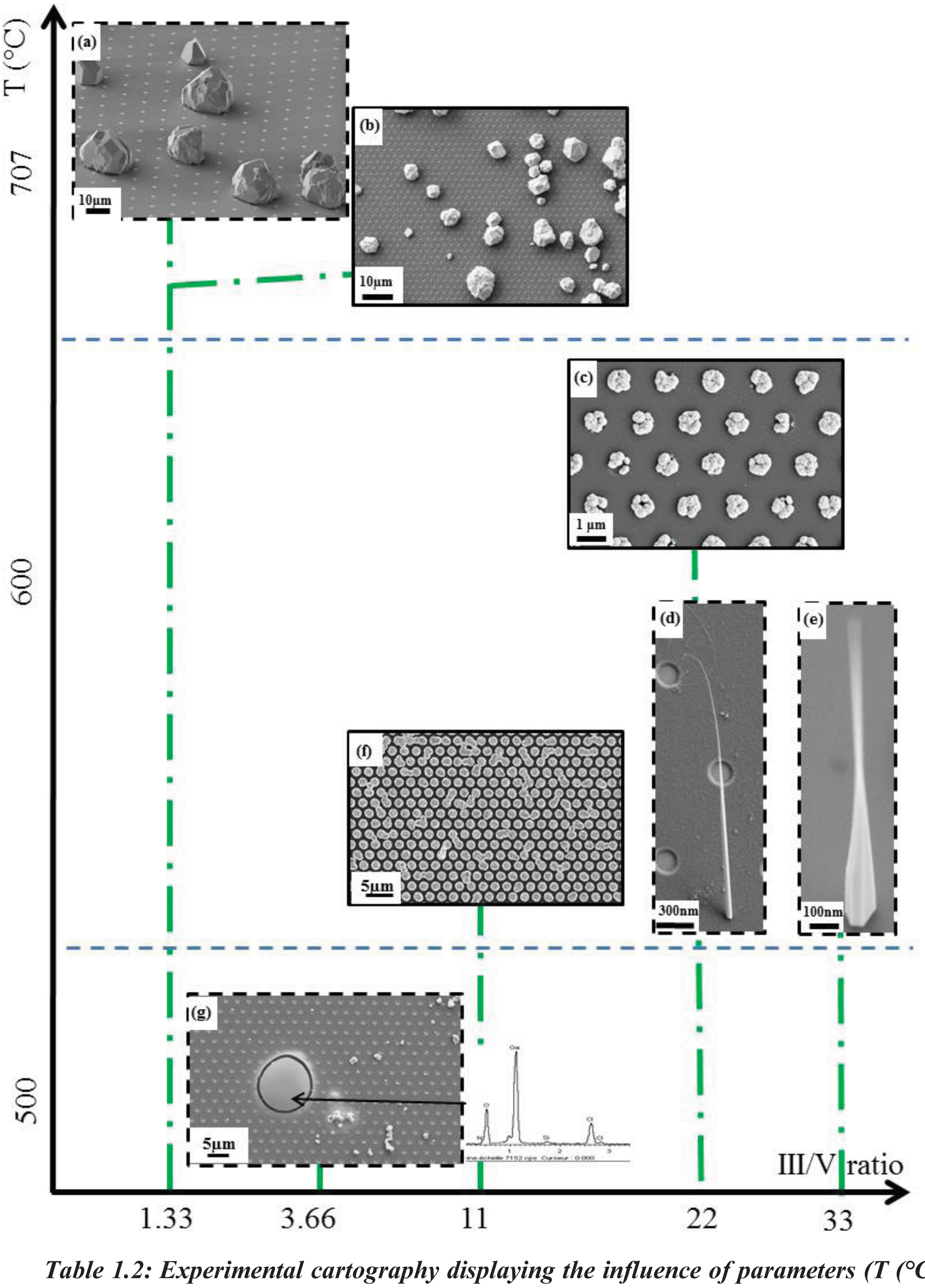

Table 1.2: Experimental cartography displaying the influence of parameters (T (°C), III/V ratio, patterned substrate, multi-steps growth process) on the growth of GaAs nanostructures. One-step processes results are encircled with a dotted line, two- and multi-steps processes images are encircled by a solid line. For temperature: (a)-(b) growth at 707 °C, (c)-(f) at 600 °C and (g) at 500 °C. For III/V atomic ratio: (a)-(b) at 1.33, (g) at 3.66, (f) at 11, (c)-(d) at 22 and (e) at 33. Image (e) was obtained with non-patterned Si (111) substrate.

Discussion:

Growth temperature. The main observation is: at low temperature (500 °C), neither nanowire growth nor GaAs crystallite growth is observed. Energy-dispersive X-ray spectroscopy (EDX) analyses showed a chlorine peak (Table 1.2 (g)). It mainly relates to the low decomposition efficiency of GaCl at this temperature, yielding traces of non-decomposed $GaCl_n$ on the substrate. At high temperature (707 °C), only 3D crystals are formed within the same III/V ratio range [1.33, 3.66] (Table 1.2 (a) and (b)).

III/V ratio, substrates and process-steps. For medium III/V ratios [11,22] at 600 °C, a good selectivity is observed on the patterned substrate with a multi-process growth (Table 1.2 (c) and (f)). However, these experimental conditions do not favor the growth of nanowires, especially when we compare the results between (c) and (d). Those two tests were performed with the same III/V ratio at 600 °C, the only difference being the choice of the process. The multi-steps process (c) did not provide nanowires but fills the holes with GaAs crystallites. One can conclude that the patterned openings are too large to favor the nucleation and growth of nanowires on silicon [64]. Furthermore, for the highest element V inputs which were tested (for III/V atomic ratio < 22), the growth of GaAs polycrystals are promoted rather than nanowires: liquid gallium deposited at the beginning is quickly consumed by As_4 atoms to form solid GaAs nuclei crystals, that enlarge by condensation directly. We can thus state that the optimized conditions to favor self-catalyzed growth of GaAs nanowires are 600 °C, with a high III/V atomic ratio such as for (d) and (e), with a one-step process and small nucleation sites created by long time HF etching up to 10 mins on the Si substrate surface.

1.4.6 Optimized self-catalyzed growth of GaAs nanowires by HVPE

Based upon the above considerations, we decided to simplify the growth procedure and to perform one-step HVPE growth at 600 °C (shown in Table 1.2 (d) and (e)). The growth recipe was the following. Instead of using a patterned Si substrate with holes of which too large diameter does not favor the creation of gallium droplets on the surface, we chose unpatterned Si (111) substrates to get spontaneous nucleation sites. The substrates were chemically etched in 1% hydrofluoric acid from 3 to 10 minutes in order to partially remove the native SiO_2 layer and create nucleation sites for gallium droplets. The growth was performed at 600°C, the equivalent partial pressure of As (further labelled P_5 ; it is deduced from the cracking of AsH_3 and equilibrium between As_2 and As_4 gaseous species) was deliberately set to very low values between 1.5 to 30 Pa, while the partial pressure of GaCl (P_3) was varied from 265 to 660 Pa, yielding unusual high III/V atomic ratios ranging from 11 to 222, compared to III/V ratios used in MBE and MOVPE processes.

Table 1.3 displays the partial pressures of GaCl and equivalent As that were tested and the resulting III/V atomic ratios.

	As pressure variation for a given GaCl partial pressure					
III/V atomic ratio	**11**	**17**	**22**	**33**	**44**	**220**
$P_{GaCl}=P_3$ (atm)	**3.26E-03**	**3.26E-03**	**3.26E-03**	**3.26E-03**	**3.26E-03**	**3.26E-03**
$P_{As}=P_5$ (atm)	**2.95E-04**	**1.96E-04**	**1.47E-04**	**9.82E-05**	**7.37E-05**	**1.47E-05**
$P_{GaCl}=P_3$ (Pa)	**330**	**330**	**330**	**330**	**330**	**330**
$P_{As}=P_5$ (Pa)	**30**	**20**	**15**	**10**	**7.45**	**1.5**
Sccm HCl on Ga_{liq}	**10**	**10**	**10**	**10**	**10**	**10**
Sccm AsH_3	**6**	**4**	**3**	**2**	**1.5**	**0.3**
	GaCl pressure variation for a given As partial pressure					
III/V atomic ratio	**88**	**66**	**53**	**44**	**35**	**-**
$P_{GaCl}=P_3$ (atm)	**6.49E-03**	**4.88E-03**	**3.91E-03**	**3.26E-03**	**3.26E-03**	**-**
$P_{As}=P_5$ (atm)	**7.37E-05**	**7.37E-05**	**7.37E-05**	**7.37E-05**	**7.37E-05**	**-**
$P_{GaCl}=P_3$ (Pa)	**658**	**494**	**396**	**330**	**264**	**-**
$P_{As}=P_5$ (Pa)	**7.45**	**7.45**	**7.45**	**7.45**	**7.45**	**-**
Sccm HCl on Ga_{liq}	**20**	**15**	**12**	**10**	**8**	**-**
Sccm AsH_3	**1.5**	**1.5**	**1.5**	**1.5**	**1.5**	**-**

Table 1.3: Partial pressures and related III/V atomic ratios that were tested, together with the input flows in sccm. P_{As} is the calculated equivalent pressure for a single As atom, deduced from the cracking of AsH_3 (which is actually introduced in the reactor) and equilibrium between As_2 and As_4 gaseous species.

Fig. 1.23 (a) and (b) show the SEM images of GaAs nanowires obtained with III/V atomic ratios of 220 and 33 after 10 minutes of growth. Post-growth studies reveal the presence of GaAs nanowires along with GaAs crystallites of different sizes (Fig. 1.23 (c)).

All nanowires are oriented along the <111>$_B$ direction. Nanowires have different lengths on a single sample. The average integrated growth rate (i.e., the mean nanowire length divided by the total growth time of 10 min) can be estimated at 30 µm/h for the most representative 5 µm-long nanowires (Fig. 1.23 (a)) and reaches more than 60 µm/h for the longest nanowires (Fig. 1.23 (c)) at P_5=7.45 Pa and P_3=396 Pa.

Fig. 1.23 (d) shows the variation of the mean nanowire length as a function of the equivalent As partial pressure at a fixed growth temperature of 600 °C and fixed GaCl partial pressure of 330 Pa. It gradually decreases with increasing P_5, from 5750 nm at P_5= 1.5 Pa to only 330 nm at P_5= 20 Pa. Further increase of P_5 to 30 Pa leads to suppression of any nanowire growth. This behavior is very unusual because, in the case of MBE, the axial nanowire growth rate is known to increase almost linearly with the arsenic flux [75] [77] [87] [104]. Varying the GaCl partial pressure from 264 to 658 Pa (Fig. 1.23 (e)) at fixed equivalent As (7.45 Pa)) produces the non-monotonic dependence of the mean nanowire length that reaches its maximum at 8800 nm for P_3 around 396 Pa. No nanowires grow at a high P_3 of 658 Pa. This is also unusual because, in the case of MBE, the axial nanowire growth rate is not influenced by the gallium flux which only changes the droplet size [72] [77] [91] [104]. The results were repeatable for different values of the fixed GaCl or As pressure in each case, i.e., a monotonic decrease of the nanowire length with increasing P_5 and a unimodal behavior under varying P_3.

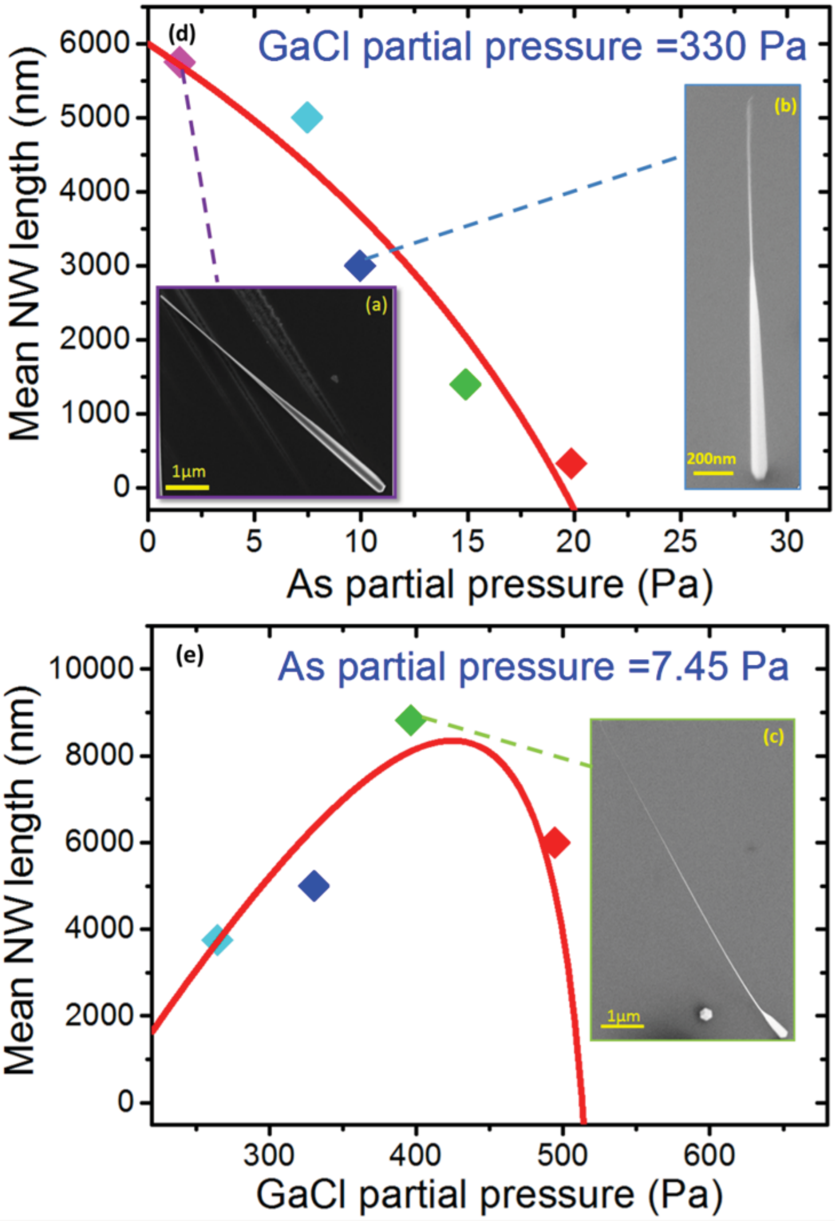

Fig. 1.23. SEM images of GaAs Nanowires grown at 600 °C at III/V = 222 (a), III/V = 33 (b), III/V = 55 (c). A GaAs crystallite can be seen (c). (d) Mean nanowire length versus the As equivalent partial pressure P_5 at P_3 = 330 Pa (symbols), lines are theoretical fits discussed later on. (e) Mean nanowire length versus the GaCl partial pressure P_3 at P_5 = 7.45 Pa (symbols), lines are theoretical fits discussed later on. Growth time was 10 min for each experiment.

HRTEM images of typical GaAs nanowires mechanically separated from the substrate and deposited on a holey carbon grid are shown in Fig. 1.24. They were obtained on a FEI-Tecnai microscope operated at 200 kV and equipped with an energy dispersive X-ray (EDX) system from Oxford Instrument.

The nanowire shown in Fig. 1.24 (a) to (f) presents a very thick (300 nm at the base) tapered trunk with a pure zinc-blende crystal structure (Fig. 1.24 (b)) and no evidence of twins or stacking disorder as often observed in MBE-grown self-catalyzed GaAs nanowires [78]. A similar nanowire observed perpendicular to the growth axis reveals a base of hexagonal shape (Fig. 1.24 (f)). Elemental maps of Ga and As obtained from EDX analysis show that the nanowire has a homogeneous composition of gallium and arsenic (Fig. 1.24 (d) and 3 (e)), and in particular no Ga droplets or Ga-rich regions are found at the nanowire tip. Of course, this does not evidence the absence of droplets during growth as all the excess gallium should be completely consumed in the cool-down stage. The second nanowire (Fig. 1.24 (g) to (i)) exhibits twinning, however, no wurtzite-zincblende polytypism is observed at the tip. This is in sharp contrast with most MBE-grown nanowires that have short wurtzite segments just beneath the droplet [77], associated with the droplet shrinking at the end of growth.

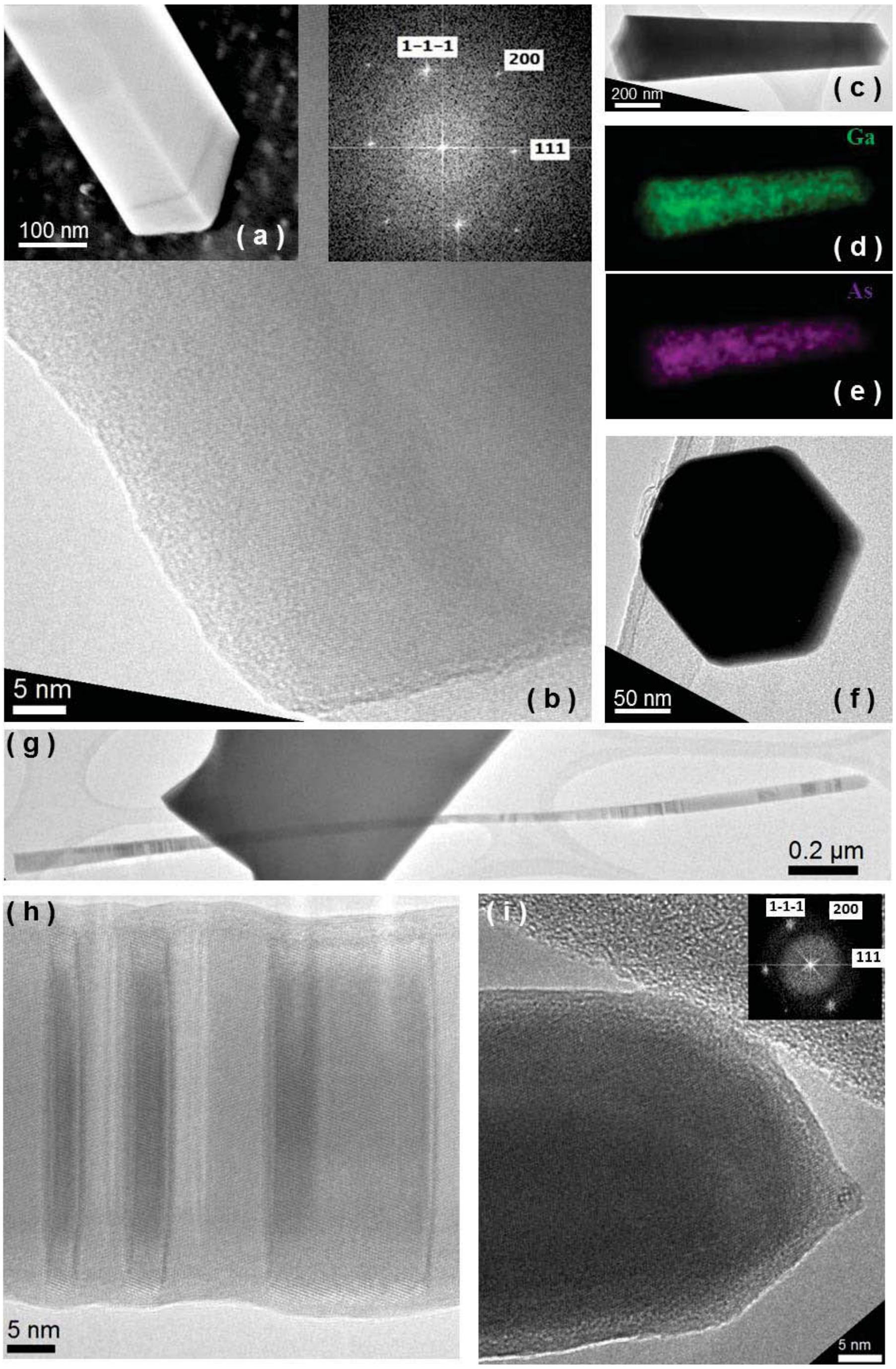

Fig. 1.24: (a) Contact part of GaAs nanowires and Si(111). (c) TEM image of a GaAs nanowire with a thick trunk (base dimension = 300 nm); (b) corresponding HRTEM image of the bottom part; the FFT in inset reveals the defect free cubic zincblende structure of the nanowire; (d-e) corresponding gallium and arsenic elemental maps from EDX; (f) TEM image of a nanowire view along the growth axis evidencing the hexagonal shape of the base; (g) TEM image of a 2.4 µm long GaAs nanowire; (h) twin defects in the middle part of the nanowire presented in (g); (i) pure zinc blende structure of the nanowire tip.

The interface between the GaAs nanowires and the Si(111) substrate is planar and the bottom part of nanowires has a hexahedral shape, as shown in Fig. 1.24 (a). Most nanowires have tapered bases of different thickness, followed by long straight tops with a minimum radius of 4-5 nm. Similar bottle-like nanowire geometry is observed in MOVPE [85].

1.5 Modeling of HVPE-self-catalyzed growth of GaAs nanowires

We now consider theoretically the different stages involved in the gold-free HVPE growth of GaAs nanowires. This study has been carried out together with Professor Vladimir G. Dubrovskii. There are four main issues that we should understand: (i) the initial nucleation stage of nanowires and the conditions under which they can start growing; (ii) the decomposition kinetics of complex gallium and arsenic growth species; (iii) the unusual bottle-like shape of nanowires and (iv) the unusual trends of the mean nanowire length versus P_5 and P_3 shown in Fig. 1.23 (d) and (e). Given the fact that our nanowires always coexist with GaAs crystallites and that the surface density of nanowires is less than that of crystallites, we speculate that the nanowires can only emerge from gallium droplets whose nucleation is constrained by a low decomposition efficiency of GaCl and by the formation of solid GaAs under arsenic influx. Therefore, there is a competition between nucleation of liquid metal droplets and parasitic III-V crystallites as shown by the SEM image of Fig. 1.23 (c). It is also the case for MBE growth of Ga-catalyzed GaAs nanowires on unpatterned SiO_x/Si(111) [88] or selective area MBE growth of InAs nanowires on patterned SiO_x/Si(111) [105].

The proposed picture of nucleation and growth of Ga-catalyzed GaAs nanowires is schematized in Fig. 1.25. The initial nucleation of gallium droplets (step 1 in figure 4) requires that the surface filling with the gallium adatoms θ_3 reaches a certain critical value θ_3^0. [106] The θ_3 evolves with time according to

$$\frac{d\theta_3}{dt} = \chi_3 v_3 - \frac{\theta_3}{\tau_3} - \frac{\theta_3 \theta_5}{\tau_{35}} \tag{R1}$$

Here, the first term in the right hand side stands for adsorption of gallium from the vapor flux v_3 [measured in monolayers (MLs) per second] at the dechlorination efficiency χ_3 at the solid surface, the second term gives the desorption rate with the characteristic desorption time τ_3 and the third term describes the GaAs crystallization which requires meeting two gallium and arsenic atoms and occurs with the crystallization rate τ_{35}^{-1}. Assuming that the arsenic filling factor θ_5 is proportional to its vapor flux v_5, $\theta_5 = v_5\tau_5$, with τ_5 as the desorption time of arsenic atoms, we find the time t_0 required to reach θ_3^0 in the form:

$$t_0 = -\frac{1}{1/\tau_3 + v_5\tau_5/\tau_{35}} \ln\left[1 - \frac{\theta_3^0}{\chi_3 v_3}\left(\frac{1}{\tau_3} + \frac{v_5\tau_5}{\tau_{35}}\right)\right]. \quad \text{(R2)}$$

Hence, the incubation time t_0 to reach θ_3^0 for nucleation of gallium droplets will increase either because of low dechlorination efficiency χ_3, or high desorption via the formation of $GaCl_g$ (small τ_3) or fast formation of GaAs crystallites (small τ_{35}).

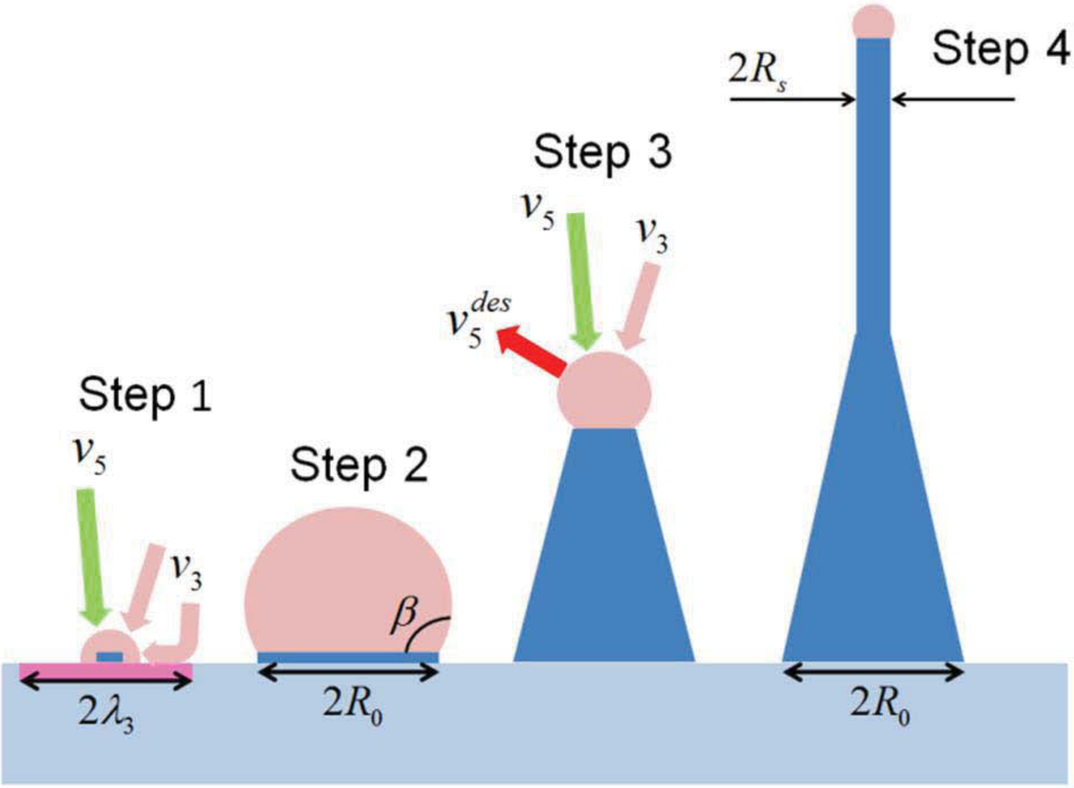

Fig. 1.25: Schematics of the GaAs nanowire growth: Step 1 – initial nucleation of the gallium droplet; Step 2 – rapid surface growth of this droplet assisted by the gallium diffusion from the substrate surface, the droplet reaches the size R_0 at which the very first nanowire ML is completed; Step 3 – growth of a tapered nanowire base with diminishing the droplet size under excessive arsenic flux, shrinking the droplet increases the arsenic desorption rate due to the Gibbs-Thomson effect; Step IV – the droplet reaches its stationary size and the nanowire top becomes straight.

The initial gallium droplets nucleate with a small size which is of the order of the critical size of classical nucleation theory, i.e., 1 nm [106]. We will now consider why and how these droplets can grow to a much larger size before producing a nanowire whose base radius in our case is of the order of 100 nm (step 2 in Fig. 1.25). Assume that the gallium adatoms diffuse toward the droplet of the base radius R_3 from the area of the radius $\lambda_3 >> R_3$ which is given by the effective diffusion length of gallium. Assume also that the arriving arsenic species immediately produce two-dimensional (2D) layer at the solid-liquid interface under the droplet. This is the worst case for the duration of the droplet growth on the surface and pertains for regular atomistic VLS growth, while there will be an additional time delay required to reach a supersaturation in the macroscopic nucleation picture [107].

We can write the two kinetic equations describing the growth rates of the 2D island radius R_{35} and the droplet base radius R_3 in the form

$$2\pi h R_{35}\frac{dR_{35}}{dt}=\frac{2\pi(v_5-v_5^{des})hR_3^2}{(1+\cos\beta_0)},$$

$$\frac{\pi R_3^2 f(\beta_0)}{\Omega_3}\frac{dR_3}{dt}=\frac{\pi v_3 h\lambda_3^2}{\Omega_{35}}-\frac{2\pi(v_5-v_5^{des})hR_3^2}{(1+\cos\beta_0)\Omega_{35}}. \qquad \text{(R3)}$$

The first equation gives the change of volume of the laterally extending 2D island of the ML height h = 0.326 nm, determined by the difference of the arsenic influx and desorption flux arriving to and leaving from the droplet surface, with β_0 as the contact angle of the gallium droplets resting on the surface. We consider a radius-independent desorption flux of arsenic atoms from the droplet given by $v_5^{des}=v_5^0\exp(n\mu_5^\infty)$, with a certain pre-exponential factor v_5^0, n as the number of arsenic atoms in the gaseous precursor and μ_5^∞ as the arsenic chemical potential in thermal units at $R_3\to\infty$ [87] [104] [107-108]. If the desorption flux is increased for small R_3 by the radius-dependent Gibbs-Thomson effect [87] [109], the duration of the droplet growth on the surface and the resulting initial nanowire radius will only increase. According to the second Eq. (R3), the droplet volume increases due to the diffusion of gallium adatoms from the area $\pi\lambda_3^2$ and decreases due to the 2D growth of solid GaAs at the liquid-solid interface, with $\Omega_3=0.02$ nm^3 as the elementary volume in the gallium droplet, $\Omega_{35}=0.0452$ nm^3 as the elementary volume in solid GaAs [91] and $f(\beta)=(1-\cos\beta)(2+\cos\beta)/(1+\cos\beta)\sin\beta$ as the geometrical function relating the droplet volume to the cube of its base through the contact angle [110].

For large enough λ_3, we can neglect the second term in Eq. (R3) for R_3. In this case, the solution for the droplet base radius is given by $R_3^3=3\varepsilon_0 h v_3\lambda_3^2 t$, with $\varepsilon_0=\varepsilon(\beta_0)$ and $\varepsilon(\beta)=\Omega_3/[\Omega_{35}f(\beta)]$ as the scaling factor. The time evolution of the 2D island radius can be put in the form

$$\frac{R_{35}}{R_3}=\left(\frac{R_3}{R_0}\right)^{3/2},\quad R_0=\lambda_3^{2/3}h^{1/3}\left[\frac{5(1+\cos\beta_0)\varepsilon_0}{2}\frac{v_3}{v_5-v_5^{des}}\right]^{1/3}\equiv\Lambda_3\left(\frac{v_3}{v_5-v_5^{des}}\right)^{1/3} \qquad \text{(R4)}$$

and hence the R_{35} remains smaller than R_3 as long as $R_3 < R_0$. Physically it means that the radial extension of 2D GaAs island under the droplet proceeds at a lower rate than the growth of the droplet size itself and the very first nanowire ML cannot be completed until the droplet base reaches the radius R_0. This requires the time $\Delta t = (5/6)(1+\cos\beta_0)[h/(v_5 - v_5^{des})]$ after the droplet nucleation at t_0. For high enough arsenic fluxes, this Δt is negligibly small compared to t_0. Therefore, the droplets reach the radius R_0 almost instantaneously after nucleation and this radius corresponds to the completion of the very first nanowire ML under the droplet. After that, the droplet will be lifted up, will change its shape and the growth will start to proceed vertically in the standard VLS mode. In this way, R_0 determines the initial nanowire radius at the base, as shown in Fig. 1.24. Rough estimate of R_0 from Eq. (R4) shows that the values of the order of 100 nm correspond to a plausible λ_3 about 1000 nm.

Considering gallium-catalyzed VLS growth, we note that most of our nanowires have strongly tapered shape in the initial stage, seen in Fig. 1.23. This step corresponds to the droplet shrinking (step 3 in Fig. 1.25) due to excessive arsenic flux to the droplet. Compared to the substrate surface, positive arsenic to gallium imbalance should be due to the absence of the gallium diffusion flux from the nanowire sidewalls to the top. Negligible gallium diffusion is known for straight Au-catalyzed HVPE GaAs nanowires at 715 °C [2] where direct impingement of gaseous species takes place into the catalyst droplets on top of the wires. It is even better justified at a much lower temperature of 600 °C and for tapered nanowire sidewalls that contain many steps to trap the gallium adatoms. However, the droplets do not shrink to zero size but rather converge to a stationary one, which explains why the nanowires grow straight starting from a certain length (step 4 in Fig. 1.25). This picture is somewhat similar to the radius self-equilibration described in Refs. [91] and [72], but in the absence of the gallium diffusion, it occurs due to the Gibbs-Thomson increase of the arsenic desorption flux from very small droplets [87] [109].

Based on the above consideration, we write down the kinetic equations describing the nanowire axial growth rate dL/dt and the growth rate of the nanowire top radius dR/dt as

$$\frac{dL}{dt} = \frac{2v_5 h}{(1+\cos\beta)}\left(v_5 - v_5^{des} e^{R_{GT}/R}\right)$$

$$\frac{dR}{dt} = \frac{2\varepsilon h}{(1+\cos\beta)}\left(v_3 - v_5 + v_5^{des} e^{R_{GT}/R}\right). \qquad \text{(R5)}$$

These expressions include the Gibbs-Thomson effect through the exponential radius-dependent terms, with $R_{GT} = (2n\Omega_5\gamma_3 \sin\beta)/(k_B T)$ as the characteristic Gibbs-Thomson radius, Ω_5 as the volume per the arsenic atom in the droplet, γ_3 as the surface energy of liquid gallium, β as the contact angle of the droplet resting on the nanowire top facet, T as the absolute temperature and k_B as the Boltzmann constant [109]. With the Gibbs-Thomson effect included, Eq. (R5) show simply that the nanowire elongation rate is determined by the difference between the arsenic adsorption and desorption fluxes, while the radial growth rate is given by the difference between the gallium vapor influx v_3 (including the decomposition efficiency of GaCl at the droplet surface) and the nanowire axial growth rate [72] [77] [91] [104]. We neglect the gallium desorption which should be very low at 600 °C.

According to this model, the radial growth rate is negative for large R due to $v_5 - v_5^{des} > v_3$ but becomes zero when the nanowire top reaches the stationary radius

$$R_s = R_{GT} \ln^{-1}\left(\frac{v_5 - v_3}{v_5^{des}}\right) \cong R_{GT} \frac{v_5^{des}}{v_5 - v_5^{des} - v_3}. \qquad \text{(R6)}$$

The approximate expression is valid when $R_s >> R_{GT}$, which should be the case because the R_{GT} value at γ_3=0.123 J/m^2 (from Ref. [87]) is only about 1 nm. Quite naturally, the stationary nanowire radius increases for higher Ga/As atomic flux ratios. Very importantly, the axial growth rate becomes $dL/dt = 2v_3 h/(1+\cos\beta)$ after the nanowire top radius reaches R_s, i.e., is given by the gallium rather than arsenic influx. Integration of Eq. (R5) at $R >> R_{GT}$ yields

$$L = \frac{R_0 - R}{\varepsilon} + \frac{R_*}{\varepsilon}\left[\frac{R_0 - R}{R_s} + \ln\left(\frac{R_0 - R_s}{R - R_s}\right)\right] = \frac{R_0 - R}{\varepsilon} + \frac{2vh_3(t - t_0)}{1+\cos\beta},$$

$$\frac{t - t_0}{\tau} = \frac{R_0 - R}{R_s} + \ln\left(\frac{R_0 - R_s}{R - R_s}\right), \qquad \text{(R7)}$$

with $R_* = v_3 R_s^2 / (v_5^{des} R_{GT})$ and $\tau = (1+\cos\beta) R_s^2 / [2\varepsilon h v_5^{des} R_{GT}]$. The first formula for the nanowire length expresses the nanowire shape through the scaling factor ε and the characteristic radius R_* at the known dimensions of the base R_0 and top R_s that can be directly measured. Fig. 1.26 shows how the tapered base increases in length for larger R_* at $\varepsilon = 0.058$, corresponding to $\beta = 120^{\circ}$. Of course, the tapered section should be more rapidly converged to the straight top for lower Ga/As atomic flux ratios. The second Eq. (R7) allows one to find the nanowire top radius and hence its length as a function of the growth time, with τ as the characteristic relaxation time to the stationary radius.

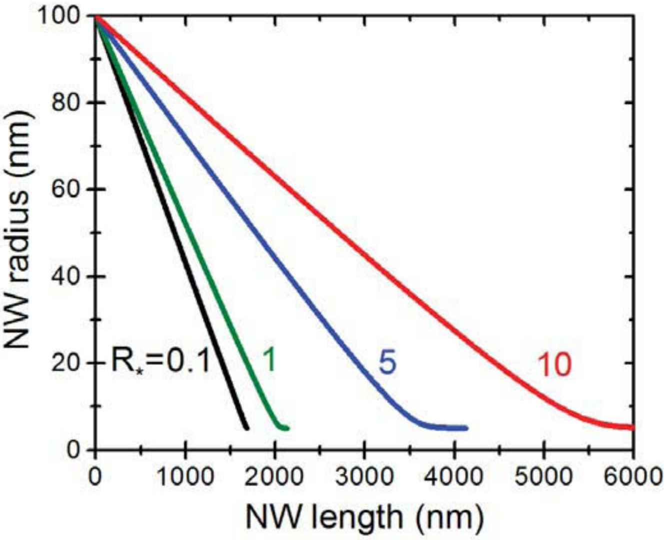

Fig. 1.26 Nanowire shapes obtained from Eq. (7) at ε =0.058, fixed R_0 = 100 nm, R_s = 5 nm and different R_* from 0.1 to 10 nm.

We now consider the dependences of the mean nanowire length on the partial pressures of AsH3 and GaCl, shown in Fig. 1.23. The fit in Fig. 1.23 (d) is obtained from Eq. (R7) for L with the incubation time t_0 given by Eq. (R2) in which τ_3 was fixed to 360 s, $a \equiv \theta_3^0/(\chi_3 v_3 \tau_3)$ to 0.7 (the values yielding best fits to the data points) and $(v_5 \tau_5 \tau_3)/\tau_{35} = bP_5$ was taken proportional to the AsH3 partial pressure, with $b = 0.0129$ Pa^{-1}. From this fit, the value of the instantaneous Ga-limited axial growth rate, $2hv_3/(1+\cos\beta)$ is estimated at 36 nm/s, or 130 µm/h, yielding $v_3 h$ = 9 nm/s at β=120°. These values are slightly larger than in Au-catalyzed HVPE growth of GaAs nanowires at 715 °C (with the instantaneous nanowire growth rate of 100-120 µm/h) due to desorption of gallium in the latter case. Taking $\theta_3^0 \sim 0.1$, we obtain the estimate for the dechlorination efficiency at the substrate surface $\chi_3 \sim 10^{-5}$ with respect to liquid gallium, meaning that only a tiny fraction of the arriving GaCl is actually decomposed. Thus, the observed decrease of the nanowire length with increasing the AsH_3 partial pressure is due to a longer incubation time required for the initial nucleation of gallium droplets for higher arsenic inputs. The fit shown in Fig. 1.23 (e) is obtained with v_3 proportional to P_3. However, this cannot describe the decrease of the nanowire length for P_3 higher than 400 Pa, and the complete suppression of the nanowire growth after ~ 550 Pa. To elaborate this effect, we assume that increasing P_3 decreases the desorption time of gallium from the substrate due to a higher concentration of HCl in vapor. The best fit to the data is obtained for the power law dependence $\tau_3 \propto P_3^{-1.77}$. Quantitative understanding of the obtained power exponent requires further studies and will be presented elsewhere.

Together with nanowires, GaAs by-product crystallites were observed on the various Si substrate surfaces. These nanoscale structures present very interesting features: some have well-defined crystal facets, that calls for discussion.

1.6 What about the nanoscale by-products?

1.6.1 GaAs nano-polyhedrons grown on Si (111) substrate by HVPE

As reported in Fig. 1.23 of section 1.5, the experimental conditions applied to grow self-catalyzed nanowires favored the growth of nanoscale by-products on the silicon substrate. These by-products consist of regular nanometer scale GaAs polyhedrons. In this section, we discuss the mechanisms which govern the growth of these GaAs nano-polyhedrons, achieved in one-step process in a record short time of 2 minutes. We observed the formation of GaAs polyhedrons with all the experiment conditions shown in Table 1.3 at 600 °C.

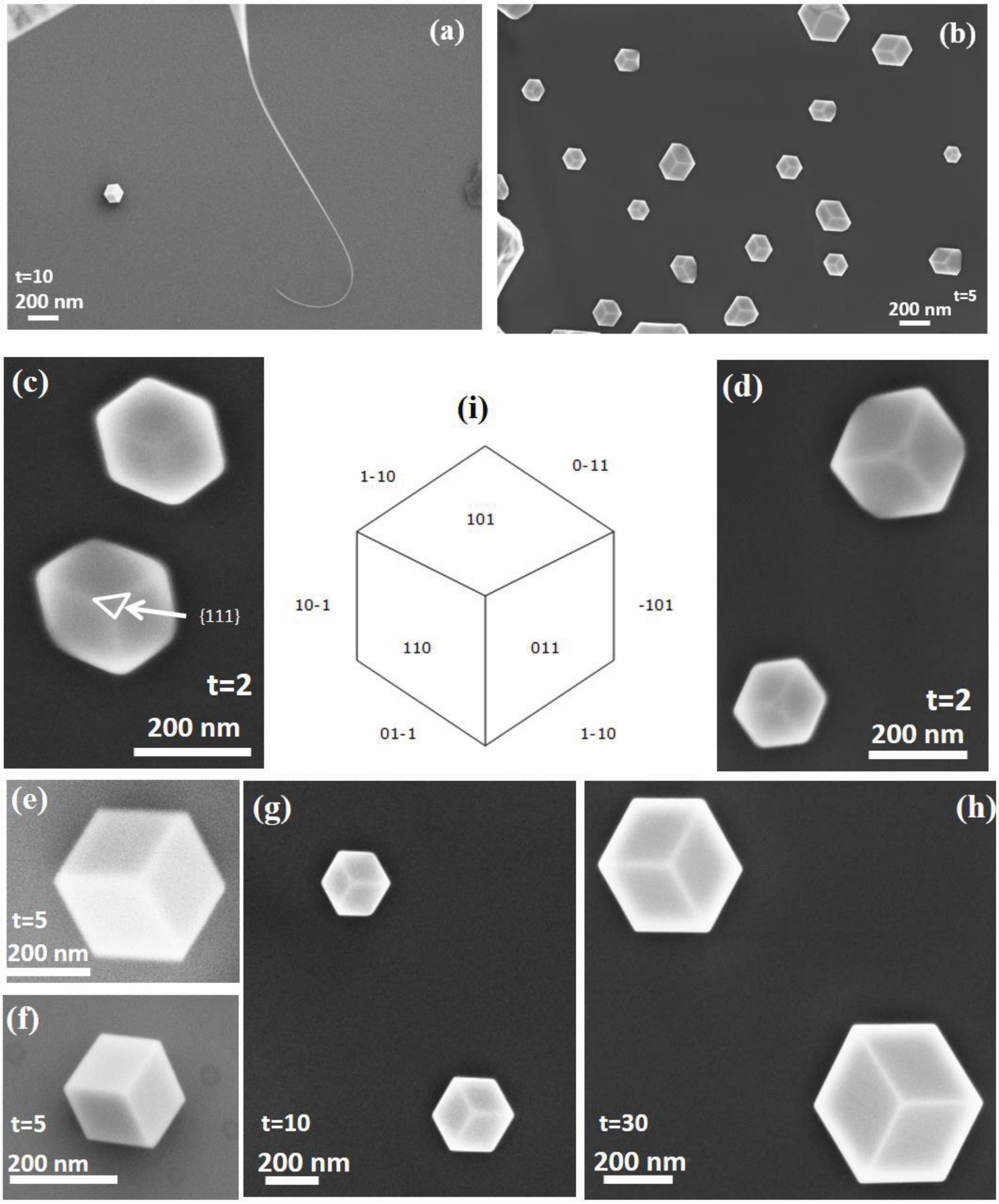

Fig. 1.27: SEM images of the top view of GaAs nano-polyhedrons grown by HVPE on Si (111), t is the growth time in min. The III/V ratio is the atomic ratio. (a) The GaAs nano-polyhedron is beside a nanowire grown with III/V = 4 and t = 10 min (b) Group of nano-polyhedrons grown with III/V = 44 and t = 5 min. Nano-polyhedrons grown under (c) III/V = 37 and t = 2 min. (d) III/V = 53 and t = 2 min. (e) and (f) III/V = 44 and t = 5 min. (g) III/V = 44 and t = 10 min. (h) III/V = 44 and t = 30 min. (i) Schematic of the top-view of a GaAs nano-polyhedron: the 9 facets belong to the {110} family.

Fig. 1.27 shows the SEM images of the top view of GaAs nano-polyhedrons grown on Si(111) as a function of the III/V ratio (from 4 to 53) and growth time (from 2 min to 30 min). It appears that the III/V ratio did not influence the size and the morphology of the nano-polyhedrons. The top of the nanostructures are bounded by {110} facets. Regarding the influence of the growth time, and for short growth time (2 min for Fig.1.27 (c)), some of the nanostructures are bounded by tiny {111}A facets. This indicates a growth competition between the {111}A and {110} GaAs facets and will be discussed later in this section. However, once the growth time is longer than 5 min, all the {111}A facets disappear. In addition, the length of the {110} side facets varies from 150 nm to 300 nm on the same substrate (see Fig. 1.27 (b)).

Nucleation inside the nano-holes in the SiO_2 layer

One reasonable assumption consists to consider that the size of opening in the native silicon dioxide governs the size of the final nano-polyhedron. This assumption is supported by results of other growth processes where similar nanostructures were observed and reported in figure 1.28 [111-113]. To initiate such nanostructures, nano-holes in the SiO_2 layer were intentionally generated through the patterning of the substrates.

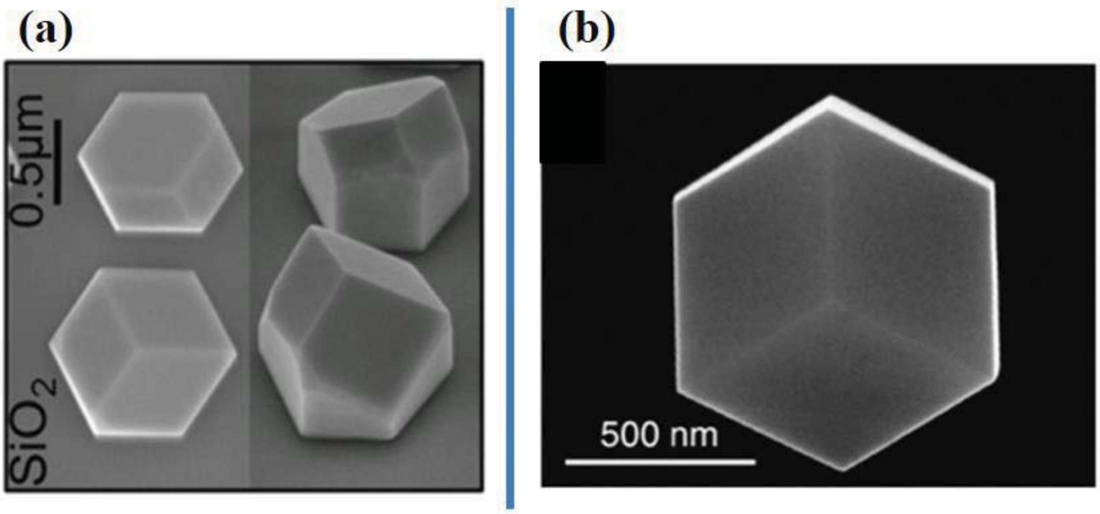

Fig. 1.28: (a) SEM images of self-assembled GaAs structures grown by MBE on patterned Si (111) in Ref. [111]. (b) GaAs structure grown by chemical beam epitaxy (CBE) via epitaxial lateral overgrowth (ELO) method on Si (111) in Ref. [113].

In Fig. 1.28 (a), GaAs crystals are grown directly by MBE on patterned Si (111) at 630 °C with a V/III ratio equal to 10 during 120 min of growth. The patterned holes of

1µm-diameter were formed by stepper lithography (Ref. [111]). In Fig. 1.28 (b), the GaAs structures were synthesized by chemical beam epitaxy (CBE) through ELO (epitaxial lateral overgrowth) method at 430 °C with a V/III ratio equal to 6 for 40 min of growth. The nanoscale seed openings were chemically produced before the growth step. According to these results and to confirm that the nucleation of the HVPE nano-polyhedrons took place in the SiO_2 holes of the Si (111) substrate, Si (111) substrates were chemically cleaned in different conditions. Three etching times in a chemical solution based of 1 % HF were applied: 1, 5 and 10 min. Then the growth was performed with a III/V equal to 44 at T = 600 °C during 10 minutes.

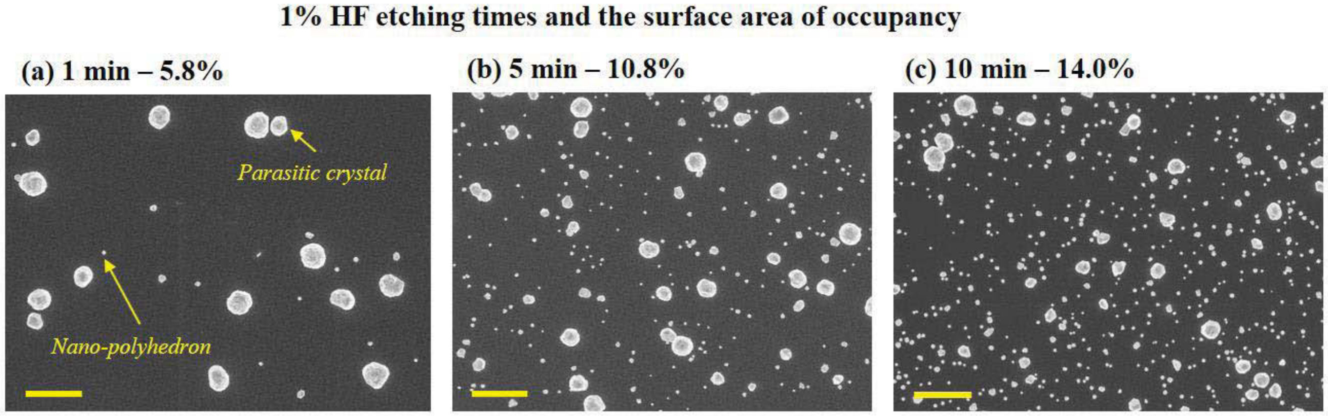

Fig. 1.28: SEM top view images of GaAs HVPE nano-polyhedrons grown on Si (111). The three Si substrates were chemically cleaned in 1% HF solution for 1min (a), 5min (b) and 10 min (c). The tiny white spots correspond to the GaAs nano-polyhedrons while the bigger ones are due to parasitic crystal structures. The surface area of occupancy by the GaAs crystals is 5.8% for (a), 10.8% for (b) and 14.0% for (c). The scale bar in each SEM image is 2 µm.

Fig. 1.28 shows the SEM images of post-growth substrates after three different chemical HF etchings. Note that there is a competition between two types of growth morphologies: the nano-polyhedrons and parasitic 3D crystal structures. The surface area of occupancy of the both structures increases by increasing the HF etching time. The density of nano-polyhedrons exhibit the same tendency: only few nano-polyhedrons were grown for the substrate etched by HF during 1 min, while the density of polyhedrons increased by increasing the etching time. Related to the state-of-the-art, this effect is due to the Si (111) surface roughness by the HF etching. During the HF chemical cleaning, after getting rid of the entire native oxide layer in 30 seconds, silicon continues to react (dissolves) with the HF aqueous solution [114-115]. This dissolution creates defects and roughness on the Si (111) surface. Then during the HVPE process temperature ramp, the SiO_2 is formed with surface defects like nano-holes as discussed in section 1.4.1. Ga adatoms nucleate preferentially in the small openings to form nano-polyhedrons. That is why the 10 min-etched surface exhibited a higher density of these nano-polyhedrons.

Crystallographic modeling of the nano-polyhedrons growth:

Cross-section SEM analysis, reported in Figures 1.29 (a) and (b), revealed that the nano-polyhedrons exhibit a hexagonal base delimited by (110) facets.

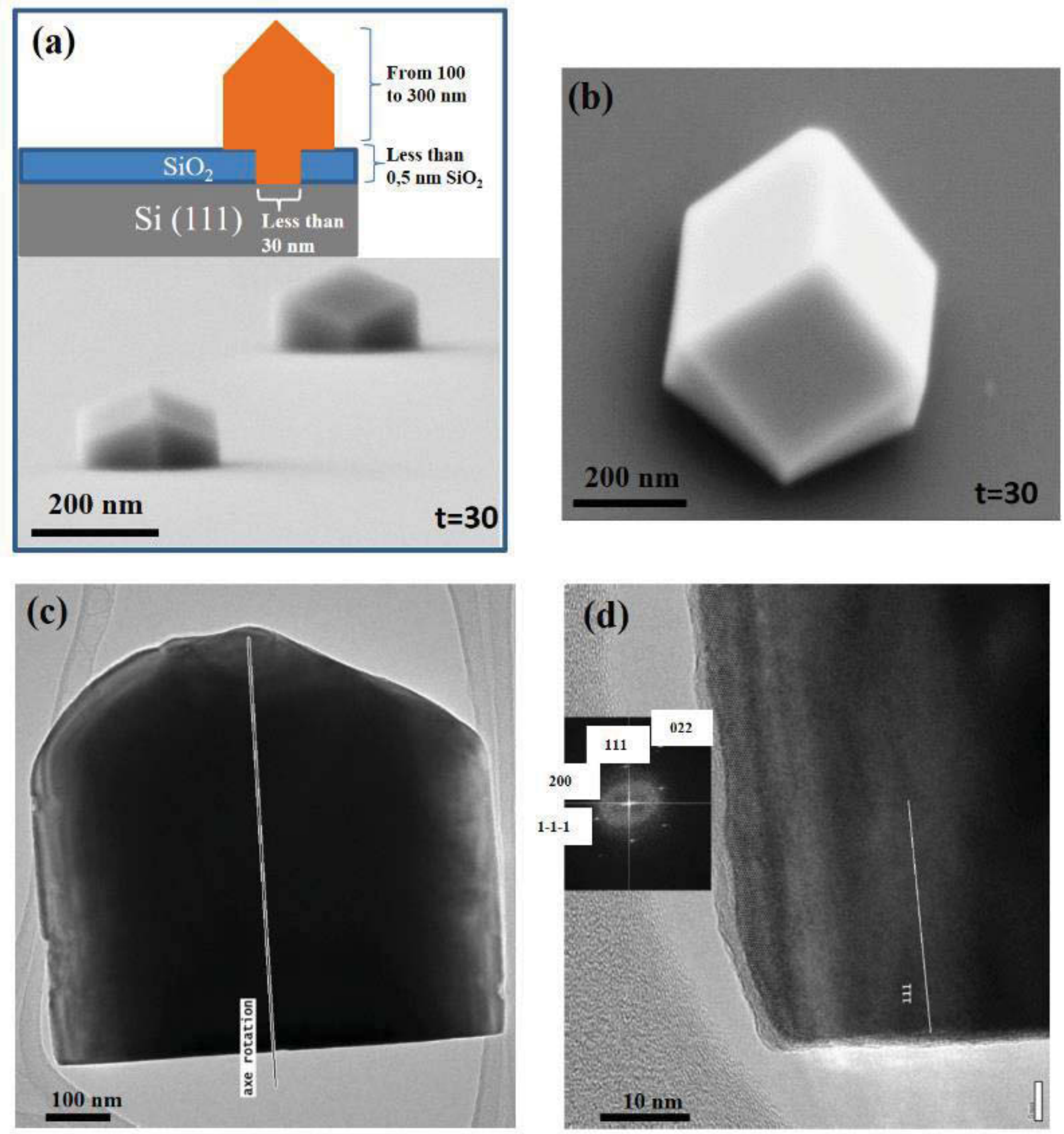

Fig. 1.29: SEM tilted views of the HVPE GaAs nano-polyhedrons grown on Si (111) with III/V = 44 and t = 30 min. (a) SEM tilted view (90°) and in insert the schematic cross section of a GaAs nano-polyhedron. (b) SEM tilted view (30°). (c) HRTEM image taken along the [0-11] zone axis of a single HVPE nano-polyhedron. (d) The FFT image shows the [111]A growth direction and the cubic ZB structure.

The SiO_2 thickness is less than 0.5 nm as measured by XPS analysis (see section 1.4.1 and in insert the schematic in Fig. 1.29 (a)).

HRTEM analysis confirms that the growth direction is [111]A and that nano-polyhedrons have a cubic ZB structure. The interface between the GaAs and the SiO_2 appears free of dislocations. These results are in agreement with the work of C. Renard who demonstrated that the use of small diameter openings lead to a dislocation-free relaxation and to the reduction of antiphase domain (APD) thanks to the ELO growth process [112-113]. An APD is a region of a crystal where the atoms present a crystallographic defect due to the polar/non-polar interfaces [116].

In order to understand the origin of the 9 crystallographic {110} facets of the HVPE nano-polyhedrons, a Wulff construction simulation is performed with the help of software WinXMorph [117]. The Wulff construction is a method used to determine the equilibrium shape of a crystal structure.

We have assumed that the shape of the nano-polyhedron was governed by the hierarchy of the growth rates of the low index faces, that is by the intrinsic growth anisotropy of the crystal. The morphology of the nano-polyhedron should then result from a simple construction referring to the growth rate vectors of the low index faces. This implies that the growth regime is strictly surface kinetics dependent [99].

The Wulff construction simulations were performed for three different conditions of R, the growth rates of the low index facets on planar GaAs substrates:

1- Isotropic growth conditions such as $R_{[110]}:R_{[111]A}:R_{[100]}=1:1:1$ (Fig. 1.30 (a)).

2- Because the planar growth rate is almost null in the growth conditions of the nano-polyhedrons (600 °C), a simulation considering the growth rates from standard growth conditions (growth temperature at 715 °C with a III/V ratio of 1) on planar GaAs (100), (111) and (110) substrates was done.

The measured growth rates were: 46.4 $\mu m.h^{-1}$ for the (100) direction, 24.5 $\mu m.h^{-1}$ for the (111) direction and 17.7 $\mu m.h^{-1}$ for the (110) direction. Therefore, the growth rate ratio of these three directions can be expressed as $R_{[110]}:R_{[111]A}:R_{[100]}=1:1.4:2.6$. The simulation results are represented in Fig. 1.30 (b). This result fits with Fig. 1.27 (e)-(h) where $t \geq 5\ min$.

3- To simulate with more accuracy the nano-polyhedrons growth, the growth rate ratio of $R_{[111]A}:R_{[110]}$ was decreased from 1.4 to 1.2. In this case, all the (100) facets disappear and only a tiny {111}A facet still appears on the top of the structure. This result is very similar to HVPE nano-polyhedron growth in short time (Fig. 1.27 (c) and (d)).

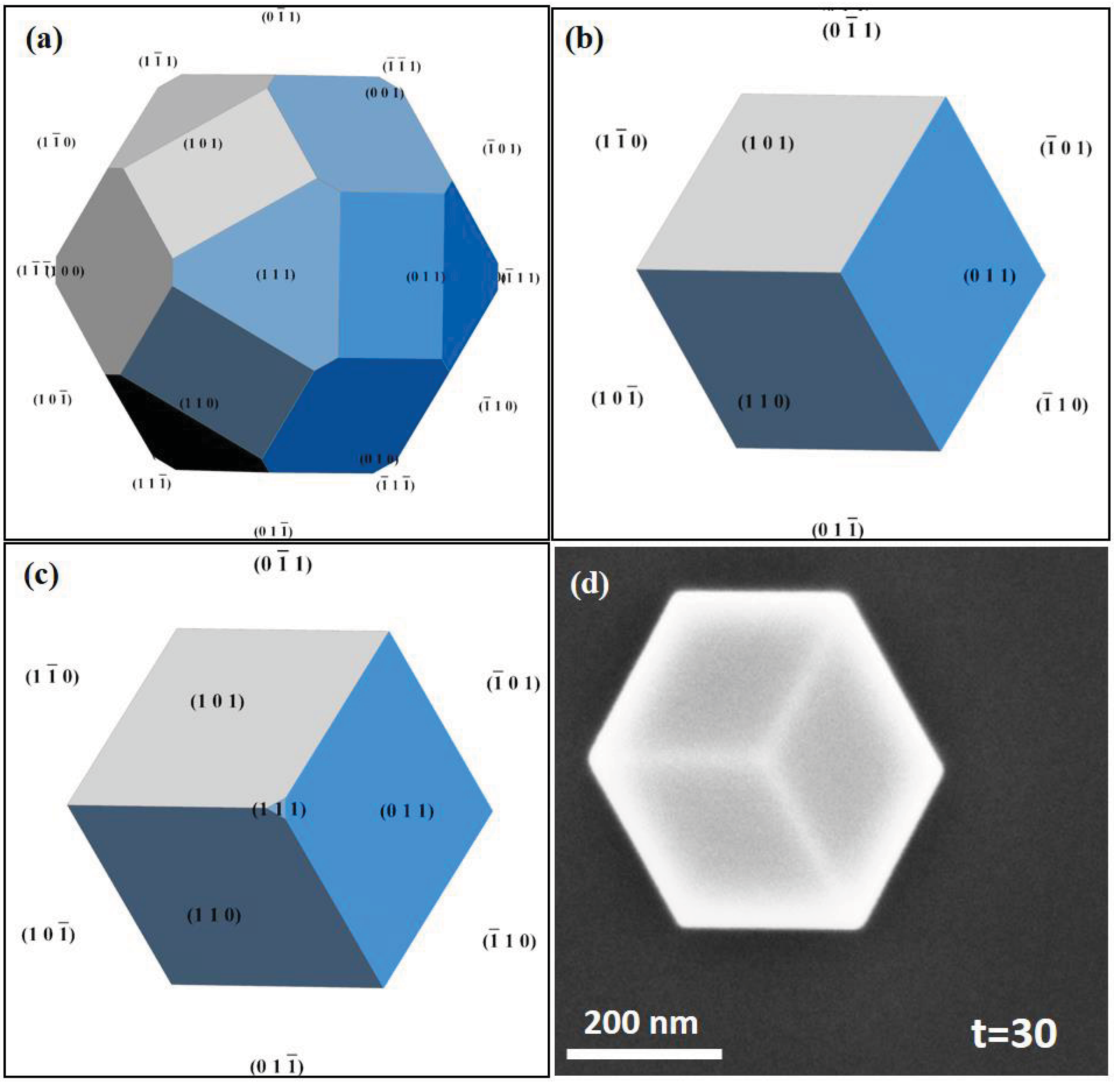

Fig. 1.30: Wulff simulations for the (111) projection direction (a)-(c). (a) $R_{[110]}:R_{[111]A}:R_{[100]} = 1:1:1$. (b) $R_{[110]}:R_{[111]A}:R_{[100]} = 1:1.4:2.6$. (c) $R_{[110]}:R_{[111]A}:R_{[100]} = 1:1.2:2.6$, anisotropic growth with lower $R_{[111]}$. (d) SEM image of GaAs polyhedron grown at III/V = 44, t = 30 min.

A good agreement was obtained between the morphology of the nano-polyhedrons and the kinetic Wulff constructions, built only from the knowledge of the growth rate anisotropy, demonstrating that a surface kinetics dependent growth regime was stabilized. Knowing the kinetics of the surface mechanisms (adsorption and desorption fluxes, decomposition frequencies and diffusion kinetics) for the low index faces [99], one can move from one morphology to another by controlling the hierarchy of the growth rates of the faces as a function of the experimental parameters.

To conclude, we can assume that the initial step for the growth of nano-polyhedrons is a self-catalyzed VLS growth mechanism as described in Fig.1.25. For step 3, a tapered nanowire is formed with reducing the droplet size under excessive arsenic flux. If the droplet composition becomes rich in As, the nanowire moves to nano-polyhedron structure by forming the {110} facets family on the top via a condensation growth process. As demonstrated by Wulff simulations, this {110}-type orientation is energetically stable and the facet morphology is due to the anisotropic growth rate of different directions. Thermodynamic modelling in collaboration with Professor V. Dubrovskii is in progress.

1.6.2 Perspective: feasibility of hybrid HVPE / CBE or MOVPE process

Today, intricate optoelectronic devices such as laser diodes, optical amplifiers, and solar cells require multiple growth and fabrication steps [118-120]. Combining different epitaxial methods with HVPE process that exhibits very high growth rate, could be a good alternative to reduce the cost of the growth steps [36]. During my PhD, a collaboration was carried out with C. Renard's team (C2N - Centre de Nanosciences et de Nanotechnologies) and KTH Royal Institute of Technology in Stockholm, to investigate the potential of combining HVPE with CBE and MOVPE processes.

Hybrid HVPE/CBE process

The first hybrid attempt was to regrow HVPE-GaAs on CBE-GaAs nanostructures grown on silicon (111) substrates.

Planar GaAs growth calibration on GaAs (100), (110) and (111) wafers was first performed. HVPE-GaAs growth was carried out in standard conditions: at 715 °C for 60 min of growth with a partial pressure of GaCl of 300 Pa, a partial pressure of As_4 of 71 Pa and with a H_2 vector flux of 3000 sccm including additional HCl flux (at 50 Pa) used to tune the supersaturation of the vapor phase [28] [31] [36]. The measured growth rates for these three different oriented GaAs substrates are: 46.4 $\mu m.h^{-1}$ for GaAs (100); 17.7 $\mu m.h^{-1}$ for GaAs (110) and 24.5 $\mu m.h^{-1}$ for GaAs (111) as presented previously.

HVPE epitaxial regrowth was carried out on the CBE-GaAs nanostructures in the standard planar growth conditions described above, after the chemical cleaning of the CBE samples in acetone/methanol solution. The growth results are reported in Fig. 1.31.

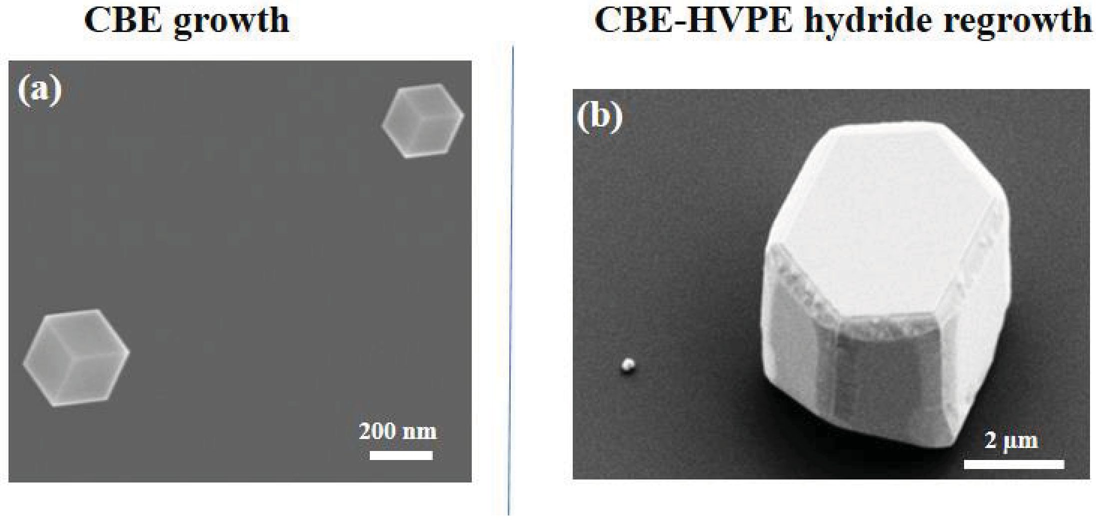

Fig 1.31: SEM images of (a) CBE-GaAs crystals on Si (111) substrate, and (b) after HVPE regrowth.

We can observe a hexagonal mesoscopic structure in 1.31 (b). More analysis is in progress but these preliminary results are very encouraging to continue the development of this hybrid process in order to enlarge the CBE structures.

Hybrid HVPE/MOVPE process

HVPE regrowth was performed on a MOVPE GaAs/Si layer obtained after corrugated epitaxial lateral overgrowth (CELOG) method [121]. A multiple circular openings-patterned MOVPE GaAs/Si substrate (Fig. 1.32 (a) and (b)) was prepared by the KTH group from Sweden [121]. This substrate was cleaned in buffered HF (BHF) diluted by iso-propanol 1:10 volume ratio for 15 seconds. The HVPE process was performed in order to have strainless thick GaAs integrated on silicon. In this specific case, the high growth rate (36 µm/h) of the HVPE process was applied to thicken the structures in the standard planar growth conditions (714 °C, 60 min of growth, GaCl of 300 Pa, As_4 of 71 Pa, H_2 vector flux of 3000 sccm including additional HCl flux (at 50 Pa)).

The pre-HVPE and post-HVPE growth SEM images are given in Fig. 1.32.

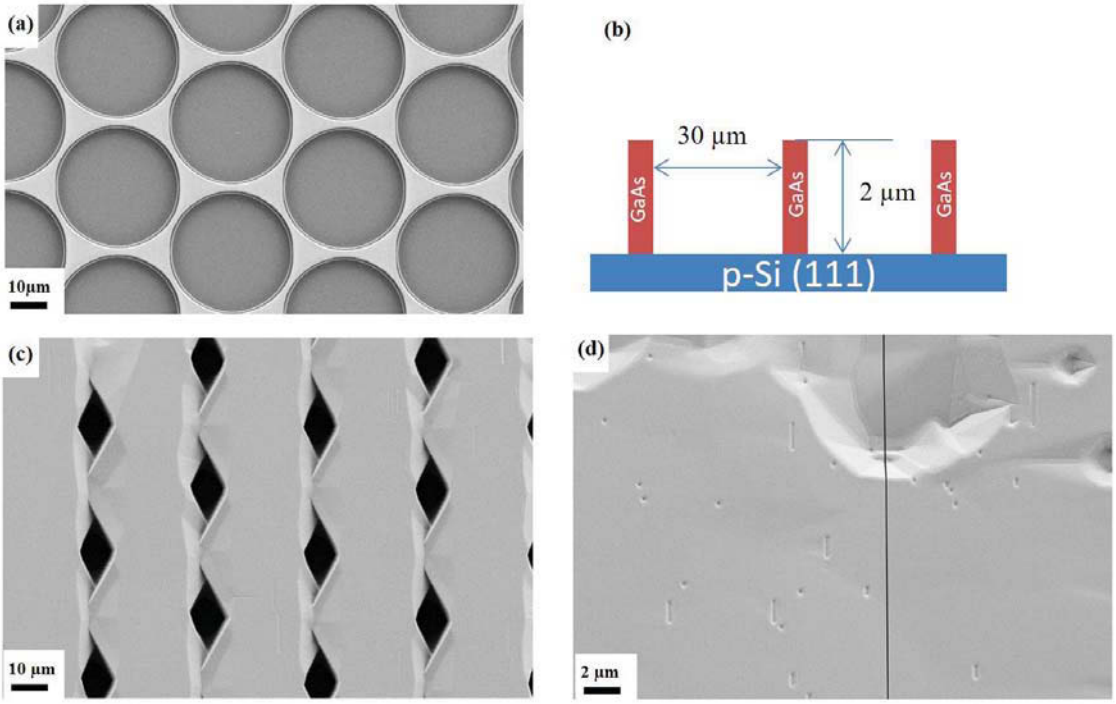

Fig. 1.32: SEM image of MOVPE pre-growth (a)-(b) and SEM images of HVPE post-growth (c)-(d). (a) GaAs circular openings on p-Si(111) substrate. (b) Scheme of the MOVPE GaAs/Si junction. The opening diameter is 30 µm, the height of the GaAs structure is 2 µm. (c) Non-coalesced overgrown structures on MOVPE GaAs circular. (d) Coalesced CELOG structure with a crack.

Hybrid HVPE-CELOG results in Fig. 1.32 exhibit two domains on the same substrate: non-coalesced and fully coalesced zones. The crack in Fig. 1.32(d) is due to the cooling step and the difference between the thermal expansion coefficients of GaAs and Si ($6.63\times10^{-6}\ K^{-1}$ for GaAs, and $2.3\times10^{-6}\ K^{-1}$ for Si).

High-resolution X-ray diffraction (HRXRD) reciprocal lattice mapping analysis was performed in KTH to analysis the strain and composition variations of the fully coalesced zones. The results are shown in Fig. 1.33.

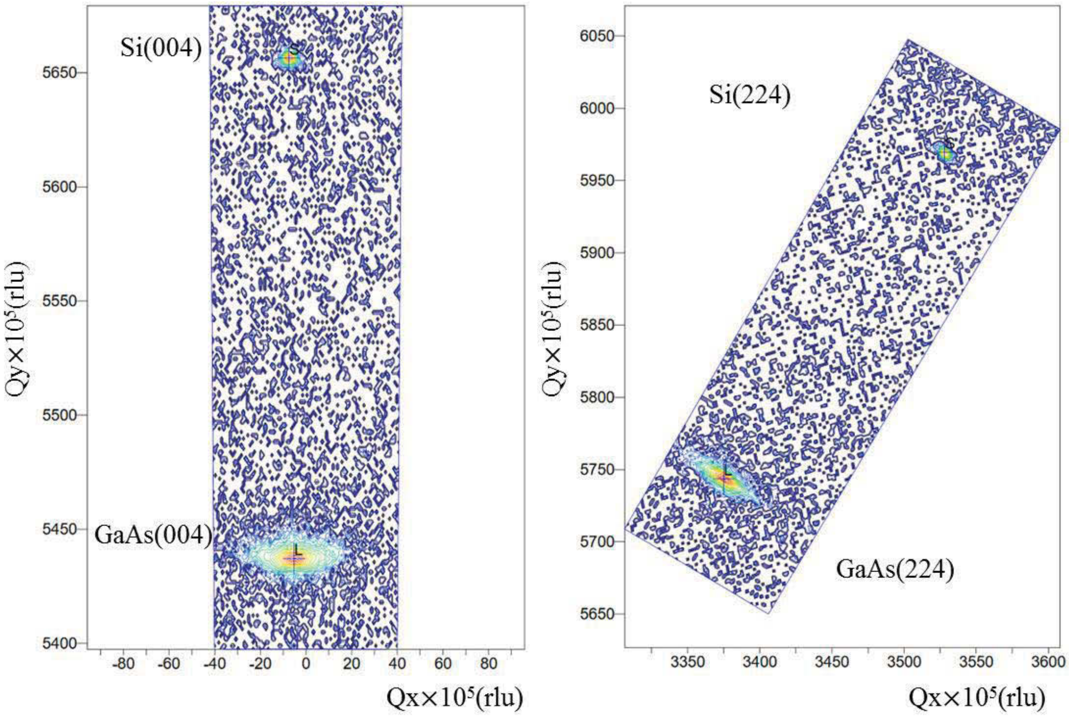

Fig. 1.33: HRXRD reciprocal lattice mapping around (004) and (224) silicon orders for the GaAs/Si CELOG growth. Peaks of Si and GaAs are marked in the images.

We can observe that the silicon diffraction peak is narrow and symmetrical whereas the GaAs CELOG layer peak is broadened (in Fig. 1.33 marked as GaAs (004) and (224)). Those peaks sign some mosaicity and complete or partial strain relaxation of the GaAs layer [122]. The peaks and maps confirm the presence of low defects in the GaAs layer. In summary, CELOG GaAs shows a good crystalline quality and further structural analysis will be performed with the collaboration of KTH.

1.7 Conclusion

Self-catalyzed growth of GaAs nanowires and nano-polyhedrons by HVPE were presented in Chapter 1. Table 1.4 displays the overall flow diagram of the HVPE experiments that were implemented.

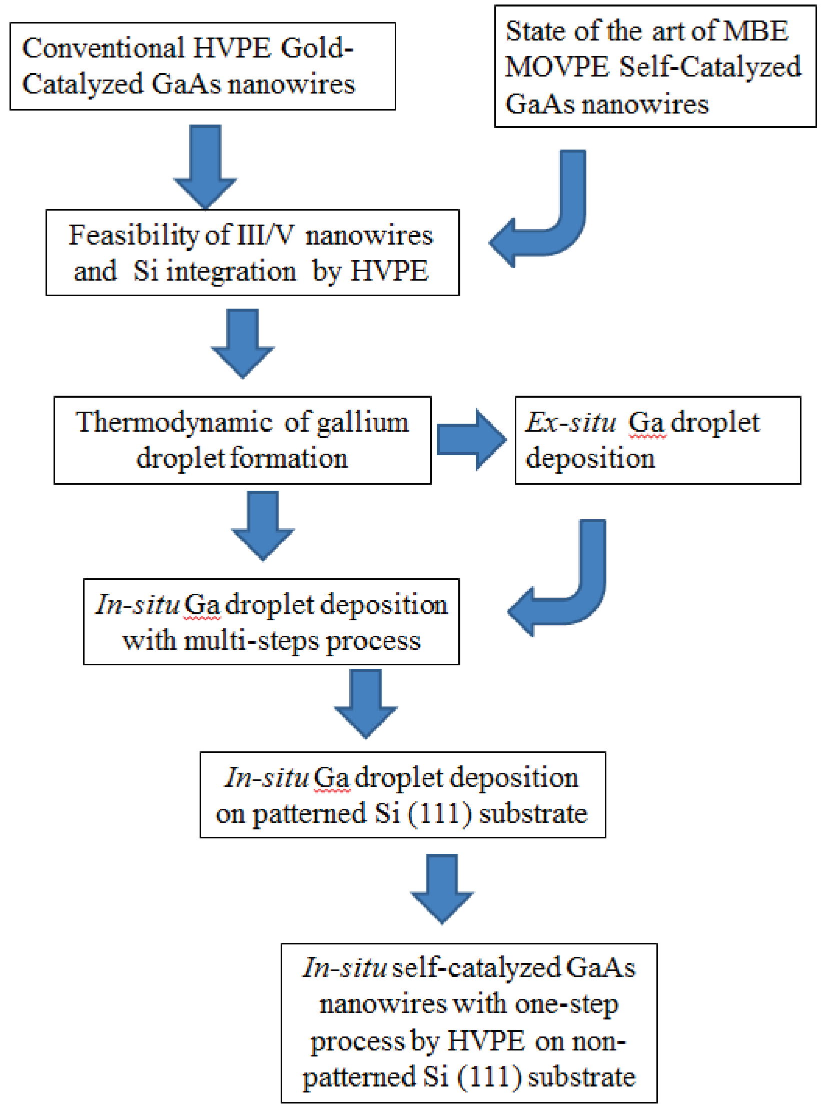

Table 1.4: Flow diagram of the HVPE experiments implemented during my PhD study.

In conclusion, we have succeeded to demonstrate gold-free GaAs nanowires grown by HVPE on unpatterned Si(111) substrates at a low temperature of 600 ºC and extremely high GaCl/AsH$_3$ flow ratios. Such growth conditions enable to successfully overcome the main difficulties of HVPE and MOVPE synthesis of gold-free GaAs nanowires, namely, the low decomposition efficiency of gallium precursors and effectively arsenic-rich atmosphere in the reactor. Nanowires can reach the 10 μm length after only 10 min of growth and are almost free of structural defects. The nanowires are strongly tapered at the beginning but then become straight with record small minimum radius of only 5 nm. A model that explains well the experimental findings was developed. In particular, we speculate that the nanowire growth is catalyzed by the gallium droplets that nucleate on the SiO_2/Si(111) surface under appropriate conditions and then rapidly swell to the size of the order of 100 nm before the very first nanowire monolayer can form. This process defines the initial nanowire radius. When the gallium droplets are brought away from the substrate, surface diffusion of gallium is disabled and the droplets shrink under excessive arsenic influx. However, the Gibbs-Thomson curvature effect largely enhances the arsenic desorption from very small droplets. Thus, the nanowires acquire a stationary radius and continue growing straight. Overall, our results give the first demonstration of cost-effective gold-free growth protocol for obtaining reasonable GaAs nanowires by vapor phase epitaxy. It may be useful for further development of HVPE, MOVPE and hybrid HVPE/MOVPE devoted to the fabrication of GaAs-based photonic nanostructures on silicon [123].

Secondly, regular nanometer scale GaAs polyhedrons as by-product grown on the same substrate besides the nanowires have attracted our attention because of their high density and well defined crystal facets. The feasibility of such structures opens the possibility to integrate GaAs on silicon. The initial nucleation of these structures is due to the presence of nano-holes in the SiO_2 generated by the chemical cleaning of the substrate. Wulff construction was built to model the crystallographic mechanism that governs the growth of this nano-polyhedrons. In the last part of the chapter, we have investigated the feasibility of hybrid HVPE/CBE or MOVPE processes. Preliminary results are very encouraging and further tasks will be continued in collaboration with C2N and KTH in Sweden.

References

[1] E. Gil, Y. André, M. R. Ramdani, C. Fontaine, A. Trassoudaine, and D. Castelluci, “Record high-aspect-ratio GaAs nano-grating lines grown by Hydride Vapor Phase Epitaxy (HVPE),” *J. Cryst. Growth*, vol. 380, pp. 93–98, Oct. 2013.

[2] E. Gil *et al.*, “Record Pure Zincblende Phase in GaAs Nanowires down to 5 nm in Radius,” *Nano Lett.*, vol. 14, no. 7, pp. 3938–3944, Jul. 2014.

[3] D. W. Shaw, “Influence of Substrate Temperature on GaAs Epitaxial Deposition Rates,” *J. Electrochem. Soc.*, vol. 115, no. 4, p. 405, 1968.

[4] D. W. Shaw, “Epitaxial GaAs Kinetic Studies: {001} Orientation,” *J. Electrochem. Soc.*, vol. 117, no. 5, p. 683, 1970.

[5] J. R. Knight, D. Effer, and P. R. Evans, “The preparation of high purity gallium arsenide by vapour phase epitaxial growth,” *Solid-State Electron.*, vol. 8, no. 2, pp. 178–180, Feb. 1965.

[6] L. Hollan and C. Schiller, “Étude de l’anisotropie de la croissance épitaxiale de GaAs en phase vapeur,” *J. Cryst. Growth*, vol. 13–14, pp. 319–324, May 1972.

[7] L. Hollan, “Influence of the Growth Parameters in GaAs Vapor Phase Epitaxy,” *J. Electrochem. Soc.*, vol. 124, no. 1, p. 135, 1977.

[8] M. Takikawa, “Two-dimensional electron gas in a selectively doped InP/In0.53 Ga0.47As heterostructure grown by chloride transport vapor phase epitaxy,” *Appl. Phys. Lett.*, vol. 43, no. 3, p. 280, 1983.

[9] C. Guedon, J. Le Bris, and J. L. Gentner, “Control of interface formation during growth of InGaAs/InP heterostructures by chloride vapour phase epitaxy,” *J. Cryst. Growth*, vol. 79, no. 1–3, pp. 909–913, Dec. 1986.

[10] V. S. Ban, K. Woodruff, M. Lange, G. H. Olsen, and K. A. Jones, “Comparison of InGaAs/InP p-i-n detectors grown by hydride and organometallic vapor phase epitaxy,” *IEEE Trans. Electron Devices*, vol. 37, no. 3, pp. 814–816, Mar. 1990.

[11] M. Cadoret, L. Chaput, H. Banvillet, A. Porte, C. Pariset, and R. Cadoret, “Kinetic processes in epitaxy of $Ga_xn_{1-x}As$ on InP(100) by hydride vapour phase epitaxy,” *Thin Solid Films*, vol. 192, no. 2, pp. 343–350, Nov. 1990.

[12] J. R. Flemish, “Altering the Composition of InGaAsP Grown by the Hydride Technique by Introducing HCl Downstream,” *J. Electrochem. Soc.*, vol. 138, no. 5, p. 1427, 1991.

[13] A. T. Macrander, “X-Ray, Photoluminescence, Stoichiometry, and Thickness Mapping of $In_{1-x}Ga_xAs_yP_{1-y}$,” *J. Electrochem. Soc.*, vol. 138, no. 4, p. 1147, 1991.

[14] C. Park, V. S. Ban, G. H. Olsen, T. J. Anderson, and K. P. Quinlan, “Process characterization and evaluation of hydride VPE grown Ga_xIn_{1-x} As using a Ga/In alloy source,” *J. Electron. Mater.*, vol. 21, no. 4, pp. 447–454, Apr. 1992.

[15] N. Gopalakrishnan, R. Dhanasekaran, and S. Lourdudoss, “Compositional analysis on quaternary $Ga_xIn_{1-x}As_yP_{1-y}$ vapour phase epitaxy: a comparison between theory and experiment,” *Mater. Chem. Phys.*, vol. 50, no. 1, pp. 70–75, Aug. 1997.

[16] C. Guedon, J. Le Bris, and J. L. Gentner, “Control of interface formation during growth of InGaAs/InP heterostructures by chloride vapour phase epitaxy,” *J. Cryst. Growth*, vol. 79, no. 1–3, pp. 909–913, Dec. 1986.

[17] R. Kobayashi, Y. Jin, F. Hasegawa, A. Koukitu, and H. Seki, “Low temperature growth of GaAs and AlAs by direct reaction between $GaCl_3$, $AlCl_3$ and AsH_3,” *J. Cryst. Growth*, vol. 113, no. 3–4, pp. 491–498, Sep. 1991.

[18] J. Leitner, J. Stejskal, V. Flemr, and P. Voňka, “Thermodynamic aspects of the preparation of AlAs and $Ga_{1-x}AlxAs$ epitaxial layers in hydride and chloride systems,” *J. Cryst. Growth*, vol. 144, no. 1–2, pp. 1–8, Nov. 1994.

[19] K. Grüter, M. Deschler, H. Jürgensen, R. Beccard, and P. Balk, “Deposition of high quality GaAs films at fast rates in the LP-CVD system,” *J. Cryst. Growth*, vol. 94, no. 3, pp. 607–612, Mar. 1989.

[20] K. L. Schulte *et al.*, “Metalorganic vapor phase growth of quantum well structures on thick metamorphic buffer layers grown by hydride vapor phase epitaxy,” *J. Cryst. Growth*, vol. 370, pp. 293–298, May 2013.

[21] T. Earles *et al.*, “Low-strain, quantum-cascade-laser active regions grown on metamorphic buffer layers for emission in the 3.0–4.0 µm wavelength region,” *IET Optoelectron.*, vol. 8, no. 2, pp. 25–32, Apr. 2014.

[22] J. Simon, D. Young, and A. Ptak, “Low-cost III-V solar cells grown by hydride vapor-phase epitaxy,” 2014, pp. 0538–0541.

[23] S. Lourdudoss, “Heteroepitaxy and selective area heteroepitaxy for silicon photonics,” *Curr. Opin. Solid State Mater. Sci.*, vol. 16, no. 2, pp. 91–99, Apr. 2012.

[24] K. L. Schulte, W. L. Rance, R. C. Reedy, A. J. Ptak, D. L. Young, and T. F. Kuech, “Controlled formation of GaAs pn junctions during hydride vapor phase epitaxy of GaAs,” *J. Cryst. Growth*, vol. 352, no. 1, pp. 253–257, Aug. 2012.

[25] M. Harrous, L. Chaput, A. Bendraoui, M. Cadoret, C. Pariset, and R. Cadoret, “Phosphine and arsine decomposition in CVD reactors for InP and InGaAs growth,” *J. Cryst. Growth*, vol. 92, no. 3–4, pp. 423–431, Oct. 1988.

[26] F. Lassalle, A. Porte, J. L. Laporte, C. Pariset, and M. Cadoret, “Growth of GaInAs/InP by the vapor phase epitaxy hydride method,” *Mater. Res. Bull.*, vol. 23, no. 9, pp. 1285–1297, Sep. 1988.

[27] E. Gil-Lafon, J. Napierala, A. Pimpinelli, R. Cadoret, A. Trassoudaine, and D. Castelluci, “Direct condensation modelling for a two-particle growth system: application to GaAs grown by hydride vapour phase epitaxy,” *J. Cryst. Growth*, vol. 258, no. 1–2, pp. 14–25, Oct. 2003.

[28] A. Pimpinelli, R. Cadoret, E. Gil-Lafon, J. Napierala, and A. Trassoudaine, “Two-particle surface diffusion-reaction models of vapour-phase epitaxial growth on vicinal surfaces,” *J. Cryst. Growth*, vol. 258, no. 1–2, pp. 1–13, Oct. 2003.

[29] G. B. Stringfellow, “Fundamental aspects of vapor growth and epitaxy,” *J. Cryst. Growth*, vol. 115, no. 1–4, pp. 1–11, Dec. 1991.

[30] G. B. Stringfellow, *Organometallic vapor-phase epitaxy: theory and practice*, 2. ed. San Diego, Calif.: Acad. Press, 1999.

[31] E. Gil-Lafon, J. Napierala, D. Castelluci, A. Pimpinelli, R. Cadoret, and B. Gérard, “Selective growth of GaAs by HVPE: keys for accurate control of the growth morphologies,” *J. Cryst. Growth*, vol. 222, no. 3, pp. 482–496, Jan. 2001.

[32] O. Mizuno and H. Watanabe, “Vapor growth kinetics of III–V compounds in a hydrogen-inert gas mixed carrier system,” *J. Cryst. Growth*, vol. 30, no. 2, pp. 240–248, Sep. 1975.

[33] L. Chaput, R. Cadoret, and M. Mihailovic, “Experimental and theoretical study of InP homoepitaxy by chemical vapour deposition from gaseous indium chloride and hydrogen diluted phosphine,” *J. Cryst. Growth*, vol. 112, no. 4, pp. 691–698, Jul. 1991.

[34] E. Kaldis, “Current Topics in Materials Science,” *J. Electrochem. Soc.*, vol. 127, no. 7, p. 283C, 1980.

[35] A. Pimpinelli, A. Videcoq, and M. Vladimirova, “Kinetic surface patterning in two-particle models of epitaxial growth,” *Appl. Surf. Sci.*, vol. 175–176, pp. 55–61, May 2001.

[36] E. Gil-Lafon, J. Napierala, A. Pimpinelli, R. Cadoret, A. Trassoudaine, and D. Castelluci, “Direct condensation modelling for a two-particle growth system: application to GaAs grown by hydride vapour phase epitaxy,” *J. Cryst. Growth*, vol. 258, no. 1–2, pp. 14–25, Oct. 2003.

[37] R. Cadoret and Evelyne Gil-Lafon, “Mécanismes de croissance des faces {001} exactes et désorientées de GaAs par la méthode aux chlorures sous H_2 : diffusion superficielle, croissance par spirale, mécanismes de désorption HCl et $GaCl_3$,” *J. Phys. I*, vol. 7, no. 7, pp. 889–907, Jul. 1997.

[38] R. Cadoret, “Growth mechanisms of (00.1)GaN substrates in the hydride vapour-phase method: surface diffusion, spiral growth, H_2 and $GaCl_3$ mechanisms,” *J. Cryst. Growth*, vol. 205, no. 1–2, pp. 123–135, Aug. 1999.

[39] M. R. Ramdani, “Croissance sélective HVPE et VLS-HVPE d’objets et de structures GaAs à morphologie contrôlée à l’échelle sub-micrométrique et nanométrique,” Université Blaise Pascal-Clermont-Ferrand II, 2010.

[40] M. Yao *et al.*, “Facile Five-Step Heteroepitaxial Growth of GaAs Nanowires on Silicon Substrates and the Twin Formation Mechanism,” *ACS Nano*, vol. 10, no. 2, pp. 2424–2435, Feb. 2016.

[41] D. W. Shaw, “Mechanisms in Vapour Epitaxy of Semiconductors,” in *Crystal Growth*, C. H. L. Goodman, Ed. Boston, MA: Springer US, 1974, pp. 1–48.

[42] M. Akiyama, Y. Kawarada, and K. Kaminishi, “Growth of GaAs on Si by MOVCD,” *J. Cryst. Growth*, vol. 68, no. 1, pp. 21–26, Sep. 1984.

[43] F. Glas, “Critical dimensions for the plastic relaxation of strained axial heterostructures in free-standing nanowires,” *Phys. Rev. B*, vol. 74, no. 12, Sep. 2006.

[44] E. Ertekin, P. A. Greaney, D. C. Chrzan, and T. D. Sands, “Equilibrium limits of coherency in strained nanowire heterostructures,” *J. Appl. Phys.*, vol. 97, no. 11, p. 114325, 2005.

[45] C.-W. Chuang, “III-V Nanowires and Nanoneedles on Lattice Mismatched Substrates for Optoelectronic Device Applications,” University of California, Berkeley, 2009.

[46] M. Heiss *et al.*, “Self-assembled quantum dots in a nanowire system for quantum photonics,” *Nat. Mater.*, vol. 12, no. 5, pp. 439–444, Feb. 2013.

[47] H. E. Jeong, I. Kim, P. Karam, H.-J. Choi, and P. Yang, “Bacterial Recognition of Silicon Nanowire Arrays,” *Nano Lett.*, vol. 13, no. 6, pp. 2864–2869, Jun. 2013.

[48] F. Qian, H. Wang, Y. Ling, G. Wang, M. P. Thelen, and Y. Li, “Photoenhanced Electrochemical Interaction between *Shewanella* and a Hematite Nanowire Photoanode,” *Nano Lett.*, vol. 14, no. 6, pp. 3688–3693, Jun. 2014.

[49] R. S. Wagner and W. C. Ellis, “Vapor-Liquid-Solid mechanism of single crystal growth,” *Appl. Phys. Lett.*, vol. 4, no. 5, pp. 89–90, Mar. 1964.

[50] R. S. Wagner and W. C. Ellis, “Vapor-liquid-solid mechanism of crystal growth and its application to silicon,” *Trans. Mettalurgic Soc. Aime*, no. 233, p. 1053, 1965.

[51] E. I. Givargizov, "Oriented growth of whiskers of $A^{III}B^{V}$ compounds by VLS-mechanism," *Krist. Tech.*, vol. 10, no. 5, pp. 473–484, 1975.

[52] T. J. Trentler, K. M. Hickman, S. C. Goel, A. M. Viano, P. C. Gibbons, and W. E. Buhro, "Solution-Liquid-Solid Growth of Crystalline III-V Semiconductors: An Analogy to Vapor-Liquid-Solid Growth," *Science*, vol. 270, no. 5243, pp. 1791–1794, Dec. 1995.

[53] A. M. Morales, "A Laser Ablation Method for the Synthesis of Crystalline Semiconductor Nanowires," *Science*, vol. 279, no. 5348, pp. 208–211, Jan. 1998.

[54] B. D. Joyce and J. A. Baldrey, "Selective Epitaxial Deposition of Silicon," *Nature*, vol. 195, no. 4840, pp. 485–486, Aug. 1962.

[55] F. W. Tausch and A. G. Lapierre, "A Novel Crystal Growth Phenomenon: Single Crystal GaAs Overgrowth onto Silicon Dioxide," *J. Electrochem. Soc.*, vol. 112, no. 7, p. 706, 1965.

[56] D. W. Shaw, "Selective Epitaxial Deposition of Gallium Arsenide in Holes," *J. Electrochem. Soc.*, vol. 113, no. 9, p. 904, 1966.

[57] J. Takeda, M. Akabori, J. Motohisa, and T. Fukui, "Formation of $Al_xGa_{1-x}As$ periodic array of micro-hexagonal pillars and air holes by selective area MOVPE," *Appl. Surf. Sci.*, vol. 190, no. 1, pp. 236–241, 2002.

[58] R. Azoulay, N. Bouadma, J. C. Bouley, and L. Dugrand, "Selective MOCVD epitaxy for optoelectronic devices," *J. Cryst. Growth*, vol. 55, no. 1, pp. 229–234, Oct. 1981.

[59] Y. Takahashi, S. Sakai, and M. Umeno, "Selective MOCVD growth of GaAlAs on partly masked substrates and its application to optoelectronic devices," *J. Cryst. Growth*, vol. 68, no. 1, pp. 206–213, Sep. 1984.

[60] K. Kamon, M. Shimazu, K. Kimura, M. Mihara, and M. Ishii, "Selective growth of $Al_xGa_{1-x}As$ embedded in etched grooves on GaAs by low-pressure OMVPE," *J. Cryst. Growth*, vol. 77, no. 1–3, pp. 297–302, Sep. 1986.

[61] K. Yamaguchi, M. Ogasawara, and K. Okamoto, "Surface-diffusion model in selective metalorganic chemical vapor deposition," *J. Appl. Phys.*, vol. 72, no. 12, p. 5919, 1992.

[62] J. J. Coleman, R. M. Lammert, M. L. Osowski, and A. M. Jones, "Progress in InGaAs-GaAs selective-area MOCVD toward photonic integrated circuits," *Sel. Top. Quantum Electron. IEEE J. Of*, vol. 3, no. 3, pp. 874–884, 1997.

[63] K. Tomioka, Y. Kobayashi, J. Motohisa, S. Hara, and T. Fukui, "Selective-area growth of vertically aligned GaAs and GaAs/AlGaAs core–shell nanowires on Si(111) substrate," *Nanotechnology*, vol. 20, no. 14, p. 145302, Apr. 2009.

[64] K. Tomioka, T. Tanaka, S. Hara, K. Hiruma, and T. Fukui, "III-V Nanowires on Si Substrate: Selective-Area Growth and Device Applications," *IEEE J. Sel. Top. Quantum Electron.*, vol. 17, no. 4, pp. 1112–1129, Jul. 2011.

[65] J. A. Hutchby, G. I. Bourianoff, V. V. Zhirnov, and J. E. Brewer, "Extending the road beyond CMOS," *IEEE Circuits Devices Mag.*, vol. 18, no. 2, pp. 28–41, 2002.

[66] R. Chau *et al.*, "Benchmarking Nanotechnology for High-Performance and Low-Power Logic Transistor Applications," *IEEE Trans. Nanotechnol.*, vol. 4, no. 2, pp. 153–158, Mar. 2005.

[67] K. Volz, W. Stolz, A. Dadgar, and A. Krost, "Growth of III/Vs on Silicon," in *Handbook of Crystal Growth*, Elsevier, 2015, pp. 1249–1300.

[68] Y. B. Bolkhovityanov and O. P. Pchelyakov, “GaAs epitaxy on Si substrates: modern status of research and engineering,” *Phys.-Uspekhi*, vol. 51, no. 5, pp. 437–456, May 2008.

[69] A. Larrue, C. Wilhelm, G. Vest, S. Combrié, A. de Rossi, and C. Soci, “Monolithic integration of III-V nanowire with photonic crystal microcavity for vertical light emission,” *Opt. Express*, vol. 20, no. 7, p. 7758, Mar. 2012

[70] D. Spirkoska, C. Colombo, M. Heiß, M. Heigoldt, G. Abstreiter, and A. F. i Morral, “Growth Methods and Properties of High Purity III-V Nanowires by Molecular Beam Epitaxy,” in *Advances in Solid State Physics*, vol. 48, R. Haug, Ed. Berlin, Heidelberg: Springer Berlin Heidelberg, 2009, pp. 13–26.

[71] S. D. Brotherton and J. E. Lowther, “Electron and Hole Capture at Au and Pt Centers in Silicon,” *Phys. Rev. Lett.*, vol. 44, no. 9, pp. 606–609, Mar. 1980.

[72] J. Tersoff, “Stable Self-Catalyzed Growth of III–V Nanowires,” *Nano Lett.*, vol. 15, no. 10, pp. 6609–6613, Oct. 2015.

[73] D. E. Perea, J. E. Allen, S. J. May, B. W. Wessels, D. N. Seidman, and L. J. Lauhon, “Three-Dimensional Nanoscale Composition Mapping of Semiconductor Nanowires,” *Nano Lett.*, vol. 6, no. 2, pp. 181–185, Feb. 2006.

[74] A. Fontcuberta i Morral, C. Colombo, G. Abstreiter, J. Arbiol, and J. R. Morante, “Nucleation mechanism of gallium-assisted molecular beam epitaxy growth of gallium arsenide nanowires,” *Appl. Phys. Lett.*, vol. 92, no. 6, p. 063112, 2008.

[75] C. Colombo, D. Spirkoska, M. Frimmer, G. Abstreiter, and A. Fontcuberta i Morral, “Ga-assisted catalyst-free growth mechanism of GaAs nanowires by molecular beam epitaxy,” *Phys. Rev. B*, vol. 77, no. 15, Apr. 2008.

[76] F. Matteini, G. Tütüncüoglu, H. Potts, F. Jabeen, and A. Fontcuberta i Morral, “Wetting of Ga on SiO_x and Its Impact on GaAs Nanowire Growth,” *Cryst. Growth Des.*, p. 150529153811003, May 2015.

[77] G. Priante, S. Ambrosini, V. G. Dubrovskii, A. Franciosi, and S. Rubini, “Stopping and Resuming at Will the Growth of GaAs Nanowires,” *Cryst. Growth Des.*, vol. 13, no. 9, pp. 3976–3984, Sep. 2013.

[78] V. G. Dubrovskii, G. E. Cirlin, N. V. Sibirev, F. Jabeen, J. C. Harmand, and P. Werner, “New Mode of Vapor−Liquid−Solid Nanowire Growth,” *Nano Lett.*, vol. 11, no. 3, pp. 1247–1253, Mar. 2011.

[79] V. G. Dubrovskii and N. V. Sibirev, “Growth thermodynamics of nanowires and its application to polytypism of zinc blende III-V nanowires,” *Phys. Rev. B*, vol. 77, no. 3, Jan. 2008.

[80] N. V. Sibirev, M. A. Timofeeva, A. D. Bol’shakov, M. V. Nazarenko, and V. G. Dubrovskiĭ, “Surface energy and crystal structure of nanowhiskers of III–V semiconductor compounds,” *Phys. Solid State*, vol. 52, no. 7, pp. 1531–1538, Jul. 2010.

[81] G. E. Cirlin *et al.*, “Self-catalyzed, pure zincblende GaAs nanowires grown on Si(111) by molecular beam epitaxy,” *Phys. Rev. B*, vol. 82, no. 3, Jul. 2010.

[82] P. Krogstrup, R. Popovitz-Biro, E. Johnson, M. H. Madsen, J. Nygård, and H. Shtrikman, “Structural Phase Control in Self-Catalyzed Growth of GaAs Nanowires on Silicon (111),” *Nano Lett.*, vol. 10, no. 11, pp. 4475–4482, Nov. 2010.

[83] F. Matteini, G. Tütüncüoğlu, D. Rüffer, E. Alarcón-Lladó, and A. Fontcuberta i Morral, "Ga-assisted growth of GaAs nanowires on silicon, comparison of surface SiOx of different nature," *J. Cryst. Growth*, vol. 404, pp. 246–255, Oct. 2014.

[84] B. Mandl *et al.*, "Au-Free Epitaxial Growth of InAs Nanowires," *Nano Lett.*, vol. 6, no. 8, pp. 1817–1821, Aug. 2006.

[85] S. Ermez, E. J. Jones, S. C. Crawford, and S. Gradečak, "Self-Seeded Growth of GaAs Nanowires by Metal–Organic Chemical Vapor Deposition," *Cryst. Growth Des.*, vol. 15, no. 6, pp. 2768–2774, Jun. 2015.

[86] Breuer, S, Karouta, F., Tan, H.H., and Jagadish, C., "MOCVD growth of GaAs nanowires using Ga droplets," in *IEEE*, Melbourne, VIC, 2012, pp. 39–40.

[87] F. Glas, M. R. Ramdani, G. Patriarche, and J.-C. Harmand, "Predictive modeling of self-catalyzed III-V nanowire growth," *Phys. Rev. B*, vol. 88, no. 19, Nov. 2013.

[88] F. Matteini, V. G. Dubrovskii, D. Rüffer, G. Tütüncüoğlu, Y. Fontana, and A. F. I. Morral, "Tailoring the diameter and density of self-catalyzed GaAs nanowires on silicon," *Nanotechnology*, vol. 26, no. 10, p. 105603, Mar. 2015.

[89] A. M. Munshi *et al.*, "Position-Controlled Uniform GaAs Nanowires on Silicon using Nanoimprint Lithography," *Nano Lett.*, vol. 14, no. 2, pp. 960–966, Feb. 2014.

[90] V. G. Dubrovskii *et al.*, "Length Distributions of Nanowires Growing by Surface Diffusion," *Cryst. Growth Des.*, vol. 16, no. 4, pp. 2167–2172, Apr. 2016.

[91] V. G. Dubrovskii *et al.*, "Self-Equilibration of the Diameter of Ga-Catalyzed GaAs Nanowires," *Nano Lett.*, vol. 15, no. 8, pp. 5580–5584, Aug. 2015.

[92] G. Koblmüller *et al.*, "Self-induced growth of vertical free-standing InAs nanowires on Si(111) by molecular beam epitaxy," *Nanotechnology*, vol. 21, no. 36, p. 365602, Sep. 2010.

[93] T. Grap, T. Rieger, C. Blömers, T. Schäpers, D. Grützmacher, and M. I. Lepsa, "Self-catalyzed VLS grown InAs nanowires with twinning superlattices," *Nanotechnology*, vol. 24, no. 33, p. 335601, Aug. 2013.

[94] X. Wang, W. Du, X. Yang, X. Zhang, and T. Yang, "Self-catalyzed growth mechanism of InAs nanowires and growth of InAs/GaSb heterostructured nanowires on Si substrates," *J. Cryst. Growth*, vol. 426, pp. 287–292, Sep. 2015.

[95] W. M. Haynes, *CRC Handbook of Chemistry and Physics, 95th Edition*. CRC Press, 2014.

[96] C. Chatillon and D. Chatain, "Congruent vaporization of GaAs(s) and stability of Ga(l) droplets at the GaAs(s) surface," *J. Cryst. Growth*, vol. 151, no. 1–2, pp. 91–101, May 1995.

[97] V. G. Dubrovskii *et al.*, "Role of nonlinear effects in nanowire growth and crystal phase," *Phys. Rev. B*, vol. 80, no. 20, p. 205305, Nov. 2009.

[98] M. R. Ramdani *et al.*, "Fast Growth Synthesis of GaAs Nanowires with Exceptional Length," *Nano Lett.*, vol. 10, no. 5, pp. 1836–1841, Apr. 2010.

[99] E. Gil, Y. André, R. Cadoret, and A. Trassoudaine, "Hydride Vapor Phase Epitaxy for Current III–V and Nitride Semiconductor Compound Issues," in *Handbook of Crystal Growth*, Elsevier, 2015, pp. 51–93.

[100] J. F. Watts and J. Wolstenholme, *An introduction to surface analysis by XPS and AES*. Chichester: Wiley, 2003.

[101] S. Bietti *et al.*, "Self-assisted GaAs nanowires with selectable number density on Silicon without oxide layer," *J. Phys. Appl. Phys.*, vol. 47, no. 39, p. 394002, Oct. 2014.

[102] W. S. Shi, Y. F. Zheng, N. Wang, C. S. Lee, and S. T. Lee, "Oxide-assisted growth and optical characterization of gallium-arsenide nanowires," *Appl. Phys. Lett.*, vol. 78, no. 21, p. 3304, 2001.

[103] R.-Q. Zhang, Y. Lifshitz, and S.-T. Lee, "Oxide-Assisted Growth of Semiconducting Nanowires," *Adv. Mater.*, vol. 15, no. 78, pp. 635–640, Apr. 2003.

[104] V. G. Dubrovskii, "Group V sensitive vapor–liquid–solid growth of Au-catalyzed and self-catalyzed III–V nanowires," *J. Cryst. Growth*, vol. 440, pp. 62–68, Apr. 2016.

[105] M. T. Robson, V. G. Dubrovskii, and R. R. LaPierre, "Conditions for high yield of selective-area epitaxy InAs nanowires on SiO_x/Si(111) substrates," *Nanotechnology*, vol. 26, no. 46, p. 465301, Nov. 2015.

[106] V. G. Dubrovskii, "Theory of VLS Growth of Compound Semiconductors," in *Semiconductors and Semimetals*, vol. 93, Elsevier, 2015, pp. 1–78.

[107] V. G. Dubrovskii, "Mono- and polynucleation, atomistic growth, and crystal phase of III-V nanowires under varying group V flow," *J. Chem. Phys.*, vol. 142, no. 20, p. 204702, May 2015.

[108] V. G. Dubrovskii, "Influence of the group V element on the chemical potential and crystal structure of Au-catalyzed III-V nanowires," *Appl. Phys. Lett.*, vol. 104, no. 5, p. 053110, 2014.

[109] V. G. Dubrovskii *et al.*, "Gibbs-Thomson and diffusion-induced contributions to the growth rate of Si, InP, and GaAs nanowires," *Phys. Rev. B*, vol. 79, no. 20, May 2009.

[110] V. G. Dubrovskii, *Nucleation Theory and Growth of Nanostructures*. Berlin, Heidelberg: Springer Berlin Heidelberg, 2014.

[111] C.-P. Chu *et al.*, "Nanoscale Growth of GaAs on Patterned Si(111) Substrates by Molecular Beam Epitaxy," *Cryst. Growth Des.*, vol. 14, no. 2, pp. 593–598, Feb. 2014.

[112] C. Renard *et al.*, "Growth of high quality micrometer scale GaAs/Si crystals from (001) Si nano-areas in SiO_2," *J. Cryst. Growth*, vol. 401, pp. 554–558, Sep. 2014.

[113] C. Renard *et al.*, "Dislocation and antiphase domain free microscale GaAs crystals grown on SiO_2 from (001) Si nano-areas," *Appl. Phys. Lett.*, vol. 102, no. 19, p. 191915, 2013.

[114] R. Memming and G. Schwandt, "Anodic dissolution of silicon in hydrofluoric acid solutions," *Surf. Sci.*, vol. 4, no. 2, pp. 109–124, Mar. 1966.

[115] V. Lehmann and U. Gösele, "Porous silicon formation: A quantum wire effect," *Appl. Phys. Lett.*, vol. 58, no. 8, p. 856, 1991.

[116] M. Kawabe and T. Ueda, "Self-Annihilation of Antiphase Boundary in GaAs on Si(100) Grown by Molecular Beam Epitaxy," *Jpn. J. Appl. Phys.*, vol. 26, no. Part 2, No. 6, pp. L944–L946, Jun. 1987.

[117] W. Kaminsky, "From CIF to virtual morphology using the *WinXMorph* program," *J. Appl. Crystallogr.*, vol. 40, no. 2, pp. 382–385, Apr. 2007.

[118] Y. Arakawa, "Multidimensional quantum well laser and temperature dependence of its threshold current," *Appl. Phys. Lett.*, vol. 40, no. 11, p. 939, 1982.

[119] M. Sugawara *et al.*, "Theory of optical signal amplification and processing by quantum-dot semiconductor optical amplifiers," *Phys. Rev. B*, vol. 69, no. 23, Jun. 2004.

[120] A. . Nozik, "Quantum dot solar cells," *Phys. E Low-Dimens. Syst. Nanostructures*, vol. 14, no. 1–2, pp. 115–120, Apr. 2002.

[121] Y. T. Sun, G. Omanakuttan, and S. Lourdudoss, "An InP/Si heterojunction photodiode fabricated by self-aligned corrugated epitaxial lateral overgrowth," *Appl. Phys. Lett.*, vol. 106, no. 21, p. 213504, May 2015.

[122] H. Yoshida, K. Inaba, and N. Sato, "X-ray diffraction reciprocal space mapping study of the thin film phase of pentacene," *Appl. Phys. Lett.*, vol. 90, no. 18, p. 181930, 2007.

[123] G. Avit *et al.*, "GaN Rods Grown on Si by SAG-HVPE toward GaN HVPE/InGaN MOVPE Core/Shell Structures," *Cryst. Growth Des.*, vol. 16, no. 5, pp. 2509–2513, May 2016.

Chapter 2: Biocompatibility of GaAs nanowires and fabrication of a Microbial Fuel Cell (MFC) Prototype

2.1 Introduction

This work was performed within the project LabEx IMobS^3 (Innovative Mobility: Smart and Sustainable Solutions) under challenge 3, dedicated to the development of processes for the production of energy for mobility. Before my PhD, a collaboration had been initiated within Institut Pascal in order to combine the knowledge in physics, electronics, electrochemistry and biology. The work presented in this chapter is the outcome of a close collaboration between several researchers of Institut Pascal: Dr. P. Fontanille and Dr. F. Audonnet from GePEB (Process, chemical and thermodynamic engineering, and Biosystems) department, and Dr. C. Varenne from PHOTON (Photonics, Waves, Nanomaterials) department. This chapter proposes the design of a Microbial Fuel Cell (MFC) prototype based on GaAs nanowire samples.

In recent decades, the energy consumption of the world has continuously increased. Energy sources can be classified into three categories: fossil fuels, renewable sources and nuclear sources. Non-renewable sources are more commonly used today [1]. Solar energy is one of the potential candidates for the future, as well as wind and water powers. Fuel cells are proposed as alternative energy sources. They use metal catalysts, they do not exhaust environmental polluting gases, they do not need mobile particles like aerogenerator and they show high energy transformation efficiency [2]. Nevertheless, high cost and mass production are the main issues of these new energy sources.

In this chapter, we will describe the functionality of a microbial fuel cell which uses an active microorganism as a biocatalyst in an anaerobic anode compartment for the production of bioelectricity [3]. A brief history of MFC will be presented, followed by the first biocompatibility tests of GaAs electrode.

The second part is devoted to the assembling of the first MFC prototype and its electrochemical characterizations based on Nernst potential measurement. The working electrode chosen here is a commercial doped-GaAs substrate in contact with a biological medium. The measurements allowed to validate the presence of an electron exchange between the bacterium biofilm (*Algoriphagus yeomjeoni*) and the GaAs doped-anode electrode at 2.0×10^{18}cm^{-3}. A standard electrochemical solution containing ions (Fe^{3+}/Fe^{2+}) at a controlled pH was used to identify the oxidation-reduction reactions that take place on the surface of the GaAs semiconductor. Finally, a last part is dedicated to measurements by impedance spectroscopy, to model the electron exchange at the interface either on the surface of a GaAs planar layer or on GaAs nanowires, in aqueous medium. The feasibility of *n*- and *p*-doping of these nanowires is also addressed.

2.2 Developments in microbial fuel cell

Electrical current produced by bacteria was observed in 1911 by M.C. Potter [4]. However, there was no salient improvement until the early 1990s when the fuel cells became common devices. MFC research has enlarged extensively after the discovery of which mediator (a chemical that transfers electrons from the bacteria in the cell to the anode) was efficient in 1999 [5-7].

MFC are devices which use bacteria as catalysts to oxidize organic and inorganic matter and generate current. Most of them can be schematically presented as in Fig. 2.1.

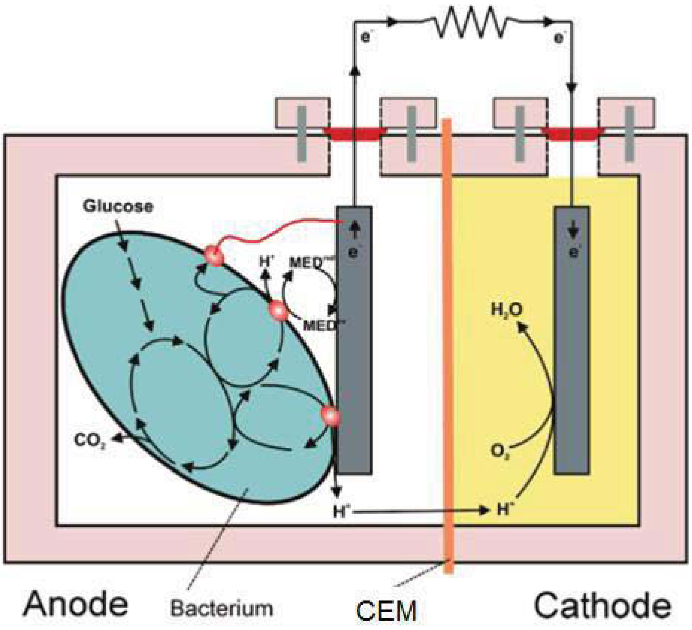

Fig. 2.1: Operating principles of a MFC. A bacterium in the anode compartment transfers electrons obtained from an electron donor (glucose) to the anode electrode. This occurs either through a direct contact, nanowires, or mobile electron shuttles (small spheres represent the final membrane associated shuttle). During electrons production, protons are also produced in excess. These protons migrate through the cation exchange membrane (CEM) into the cathode chamber. The electrons flow from the anode through an external resistance (or load) to the cathode where they react with the final electron acceptor (oxygen) and protons [8].

As shown above in Fig. 2.1, a bacterium acts as an active biocatalyst in the anode compartment. It transfers electrons given by an electron donor (glucose or acetate for example) to the anode electrode. This transfer can occur either through direct contact, nanowires, or mobile electron shuttles. Active biocatalyst in the anode compartment oxidizes the carbon sources or substrates, and generates electrons and protons. CO_2 will be created continuously by bacteria then dissolved in solvent and turn to HCO_3^-.

A MFC with an acetate oxidizing anode ($HCO_3^- = 5\times10^{-3}M, CH_3COO^- = 5\times10^{-3}M, pH = 7$) [9] can be presented by the following chemical reaction (unit M is the Molar concentration):

$2HCO_3^- + 9H^+ + 8e^- \rightarrow CH_3COO^- + 4H_2O$ Anode reaction (2.1)

Basing on IUPAC convention, all reactions in this chapter are written in the direction of chemical reduction, products are always the reduced species, and the reactants are the oxidized species (oxidized species $+ e^- \rightarrow$ *reduced species)* [10].

Microbes at anode oxidize organic fuel and generate electrons and protons. Electrons transferred to the cathode compartment through external circuit to generate current. Then, electrons and protons are consumed in cathode chamber, combining with O_2 to form water.

Both compartments can be divided by a cation exchange membrane (CEM) as shown in Fig. 2.1. The membrane placed between two separate chambers allows the transfer of charges between two electrodes, the anode chamber, where the bacteria grow, and the cathode chamber, where the electrons react with oxygen [11]. The cathode is in contact with air to provide dissolved oxygen for the redox reaction. During electron production in anode chamber, protons coming from the bacteria mechanism of glucose reduction are also produced in excess. These protons migrate through the CEM into the cathode chamber. The electrons flow from the anode through an external resistance (or load) to the cathode where they react with the final electron acceptor (oxygen) and protons [12]. Protons and electrons react with oxygen in the cathode chamber through the following chemical reduction reaction [13]:

$\frac{1}{2}O_2 + 2H^+ + 2e^- \rightarrow H_2O$ Cathode reaction (2.2)

Equations (2.1) and (2.2) are the two general equations of the MFC basic functions in two chambers. A standard oxygen reducing cathode works with ${}_pO_2 = 0.2\, bar$, and

$pH = 7$ [9]. If now we look at the mechanisms of electricity generation, MFCs can be divided in two different categories, with mediator and mediator-less MFCs [14].

The main experimental parameters which control an MFC are: the power density, the cell voltage, biological parameters and the substrate loading rate in continuous systems [3]. The substrate loading rate here is defined as the volume, concentration, and frequency of injection of organic substrates for *in-situ* anaerobic bioremediation [15]. The performance of MFCs are chiefly influenced by: (i) the oxygen supply and consumption in the cathode chamber, (ii) the substrate oxidation in the anode chamber, (iii) the electron shuttle from the anode substrate to the anode surface, and (iv) the permeability of the proton exchange membrane.

Intense research and developments on MFCs have been performed in the recent decade. B.E. Logan and his team from Penn State University are one of the pioneers in MFCs development and modeling [16-19].

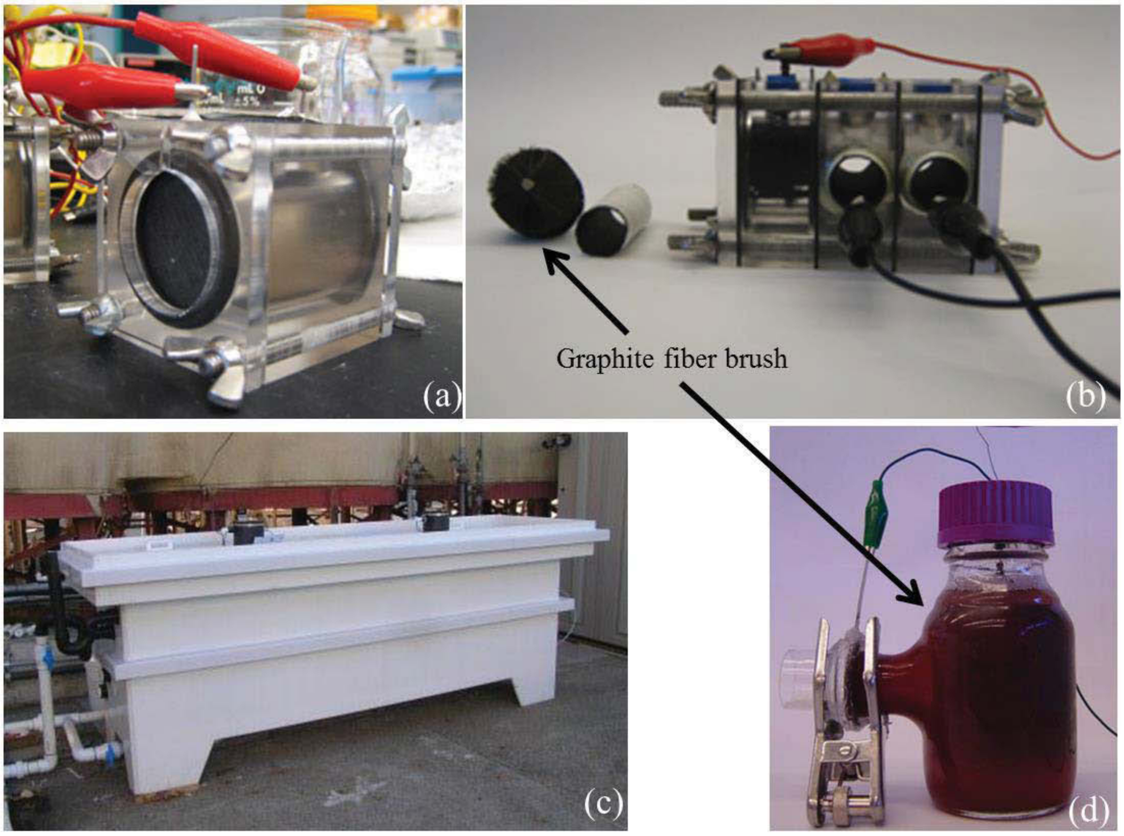

Fig. 2.2: a) Typical single chamber MFC with carbon paper as anode [19]; b) tubular membrane cathode MFC with large cathode contact surface [18]; c) a pilot-scale (1,000 L) for continuous flow MFC with a maximum of 7.4 A/m^3 [16]; d) simple single chamber MFC with graphite fiber brush as anode [17].

Fig. 2.2 shows some MFC prototypes realized by B.E. Logan's group. In order to make this technology feasible for widespread applications, this group focused on the increase of the power density, by the increase of the surface area of the material that constitutes the anode [17]. Fig. 2.2 (a) shows a typical single chamber MFC where oxygen, hydrogen protons and the electrons connected by a circuit from the anode to the cathode [19]. As shown in Fig. 2.2 (b) and (d), graphite fiber brush was chosen as the anode in order to increase the specific surface area (surface area per volume). The two tube cathodes in Fig. 2.2 (b) are based on ultrafiltration hydrophilic tubular membrane coated with graphite [18].

These two surface-area-increasing methods augment electrons production intensively. And this effect leads us to envision the use of III-V semiconductor nanowires, which have a very high surface area per volume, to fabricate a bio-battery prototype. Also, to our knowledge, no work has been published on MFC built with GaAs nanowires.

2.3.1 Biocompatibility test with the GaAs electrode

Arsenic and many of its compounds are potent poisons [20]. GaAs electrodes are therefore not implantable into a human body or animals. The prototype presented in this chapter does not address *in-vivo* applications. The biocompatibility tests are performed between few bacteria categories and GaAs nanowires in order to understand the bioenergetics property of such samples. A preliminary and previous study of biocompatibility, had been conducted by Mouna MIMOUNI during her Master internship in our laboratory.

In order to introduce the experimental results, we first give a typical five-stage biofilm development diagram in Fig. 2.3.

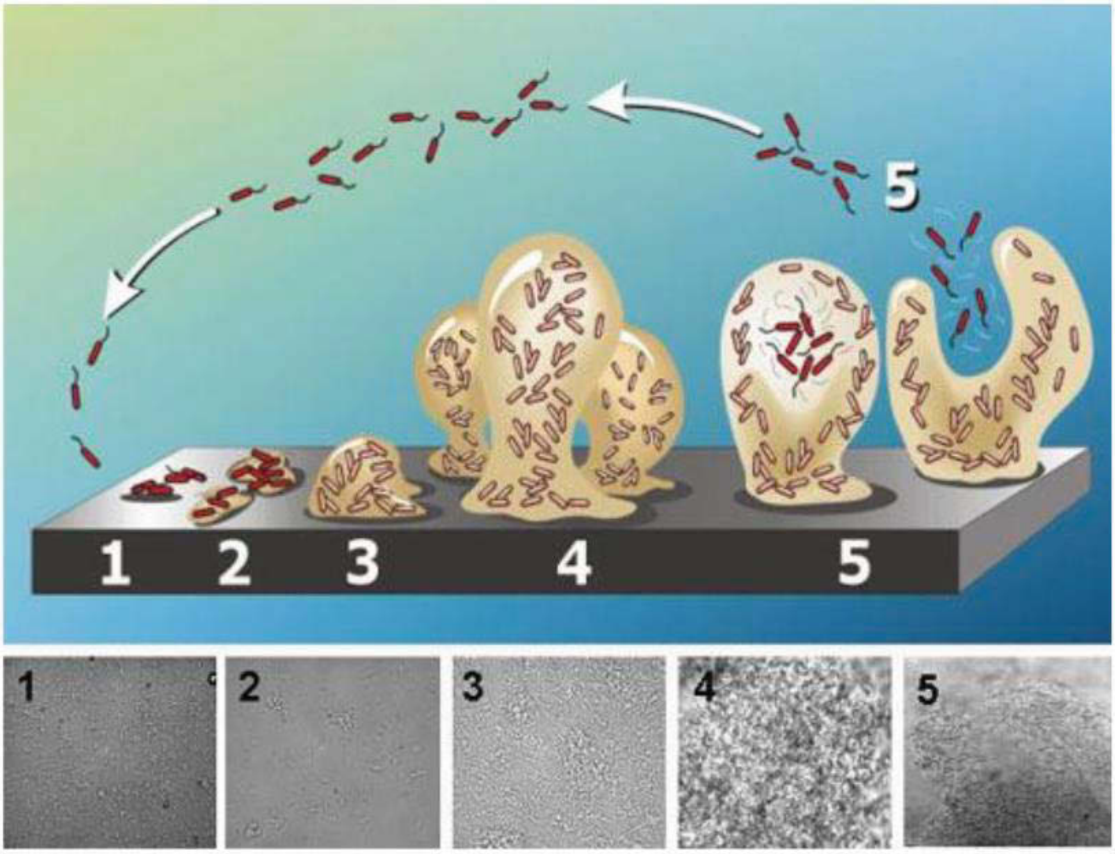

Fig. 2.3: Biofilm development diagram as a five-stage process. Stage 1: initial attachment of cells to the surface. Stage 2: production of extracellular polymeric substance (EPS) resulting in more firmly adhered "irreversible" attachment. Stage 3: early development of biofilm architecture. Stage 4: maturation of biofilm architecture. Stage 5: dispersion of single cells from the biofilm. The bottom images (1-5) show each of the five stages of the development represented by a photomicrograph of P. aeruginosa when grown under continuous-flow conditions on a glass substrate [21].

The five stages of biofilm development can be resumed as: (1) initial attachment of cells to the surface; (2) the production of extracellular polymeric substance (EPS) results in more firmly adhered "irreversible" attachment; (3) the early development of biofilm architecture and (4) maturation of biofilm architecture; and finally, (5) dispersion of single cells from the biofilm. With this basic knowledge, we can then discuss the bacteria incubation results obtained by Mouna MIMOUNI.

For this work, two types of bacteria have been tested to study the formation of strain: (a) *Algoriphagus yeomjeoni* bacteria were chosen by the biologist Dr. P. Fontanille, and supplied by Institut National Polytechnique de Toulouse (INP Toulouse) [22]. This electroactive bacterium is isolated from the natural seawater of Genoa and cultured in laboratory environment. (b) *Leuconostoc mesenteroïdes* bacteria was cultured to form strain in order to see the fluorescence. All the experiments were performed in sterilized flasks containing a mineral medium. The results are shown in Fig. 2.4:

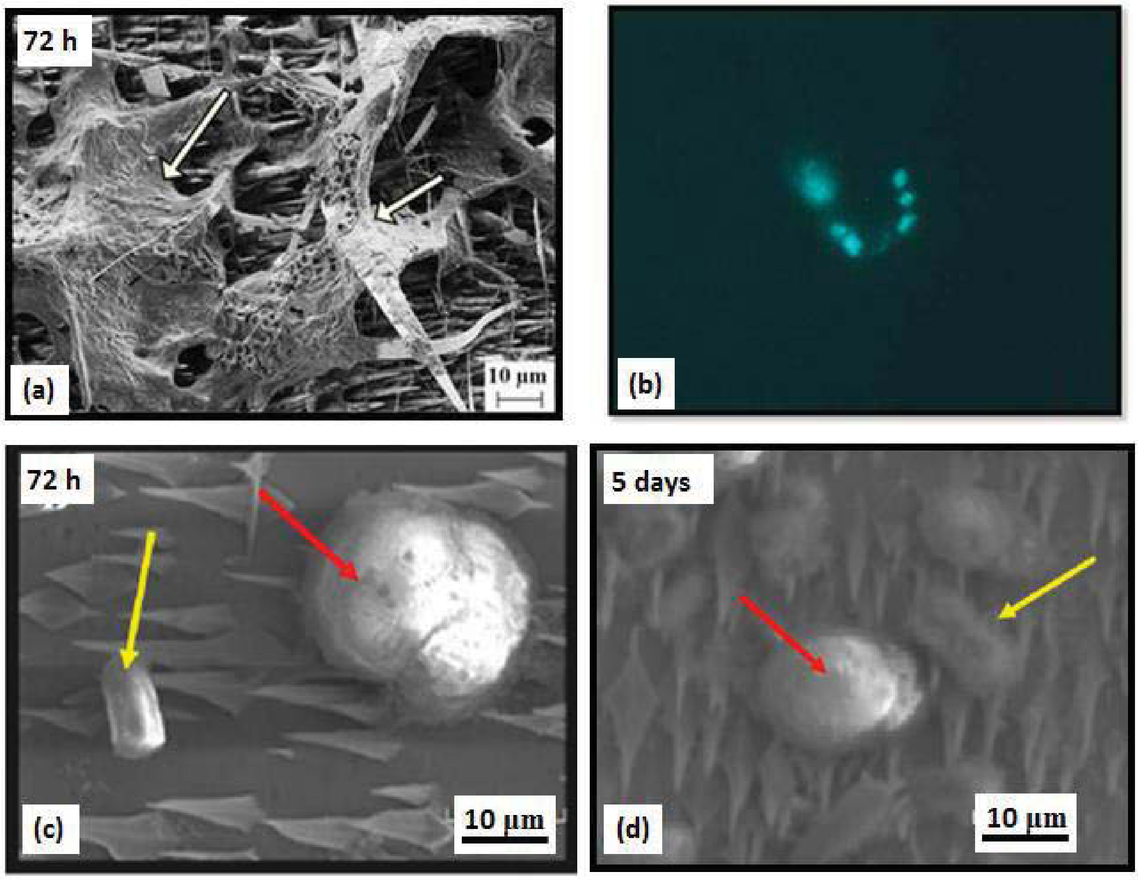

Fig. 2.4: SEM and fluorescence microscope images of bacteria strain formation. (a) **Leuconostoc mesenteroïdes** ***biofilm formation on gold-catalyzed GaAs nanowires grown by HVPE. (b) Fluorescence microscope image after DAPI coloration (4',6-diamidino-2-phenylindole, fluorescent stain), blue fluorescence represents bacteria presented in (a). (c) and (d) show the incubation of the*** **Algoriphagus** ***bacteria after 72 h (c) and 5 days (d). Yellow flash shows single bacteria, and red flash shows a group of bacteria covered by an exopolymer.***

The formation of a biofilm on GaAs nanowires was observed from SEM and fluorescence microscope images (Fig. 2.4 (a)). [15]. In Fig. 2.4, SEM and fluorescence microscope images of bacteria strain formation are presented. In (a) we can observe the formation of a biofilm of *Leuconostoc mesenteroïdes* bacteria on gold-catalyzed GaAs nanowires. Fig. 2.4 (b) shows the Fluorescence microscope image after DAPI coloration, blue fluorescence represents bacteria observed in figure (a). (c) and (d) show the incubation of the *Algoriphagus* bacteria after 72 h (c) and 5 days (d). Yellow flash shows single bacteria, and red flash shows a group of bacteria covered by an exopolymer.

From above experiments, we can conclude that the kinetic formation of bacteria is not blocked with the contact of GaAs materials. This previous work proved the biocompatibility between GaAs crystalline and the two selected bacterial strains. These results encouraged us to fabricate our MFC prototype, and get further to test its electrical properties.

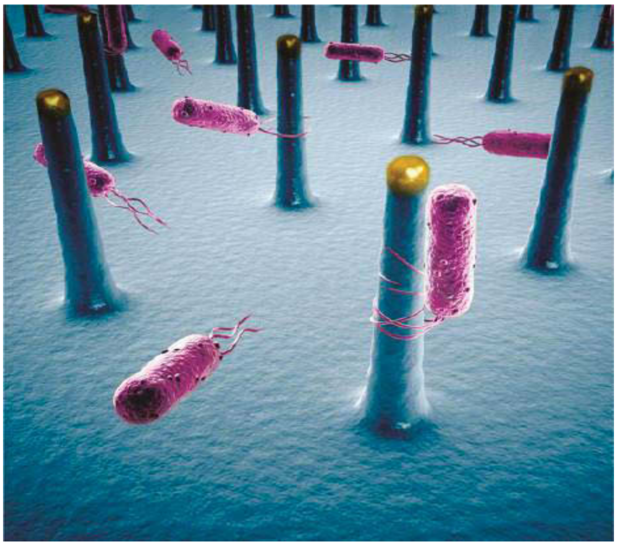

Fig. 2.5: Illustration of Shewanella oneidensis MR-1 bacteria's recognition with silicon nanowire arrays [23].

Furthermore, many papers [17-18][23-24] propose that nano- or microwires could be used as a direct contact support to bacteria. One expected situation should be that the bacteria would recognize the nanowire arrays and attach with them (Fig. 2.5). This effect may play an important role during the early stages of the biofilm formation, and finally increases the contact interface in order to increase the electrons transportation inside the biofilm with bacteria contact and increases the MCF prototype yield [23].

2.4 MFC prototype design

The MFC is placed in a sterile compartment to limit the risk of contamination of the system. The MFC installation presented in Fig. 2.6. contains: a) GaAs (100) substrate as an anode electrode; b) saturated calomel electrode as the reference electrode; c) bacteria solution as the supply of the reaction; d) bain-marie to keep the whole system at 30 °C. There is no direct cathode in this system (only the calomel electrode as cathode to perform measurement), we can consider that this prototype has an aqueous-air mix cathode, yet the efficiency was very limited by the material and the contact surface. The air-liquid interface (bacteria solution) provides the dissolved oxygen to the electrode, and the GaAs (100) substrate has a part in air which plays a role like air-cathode. With a digital potentiometer, the tension of this open circuit is measured.

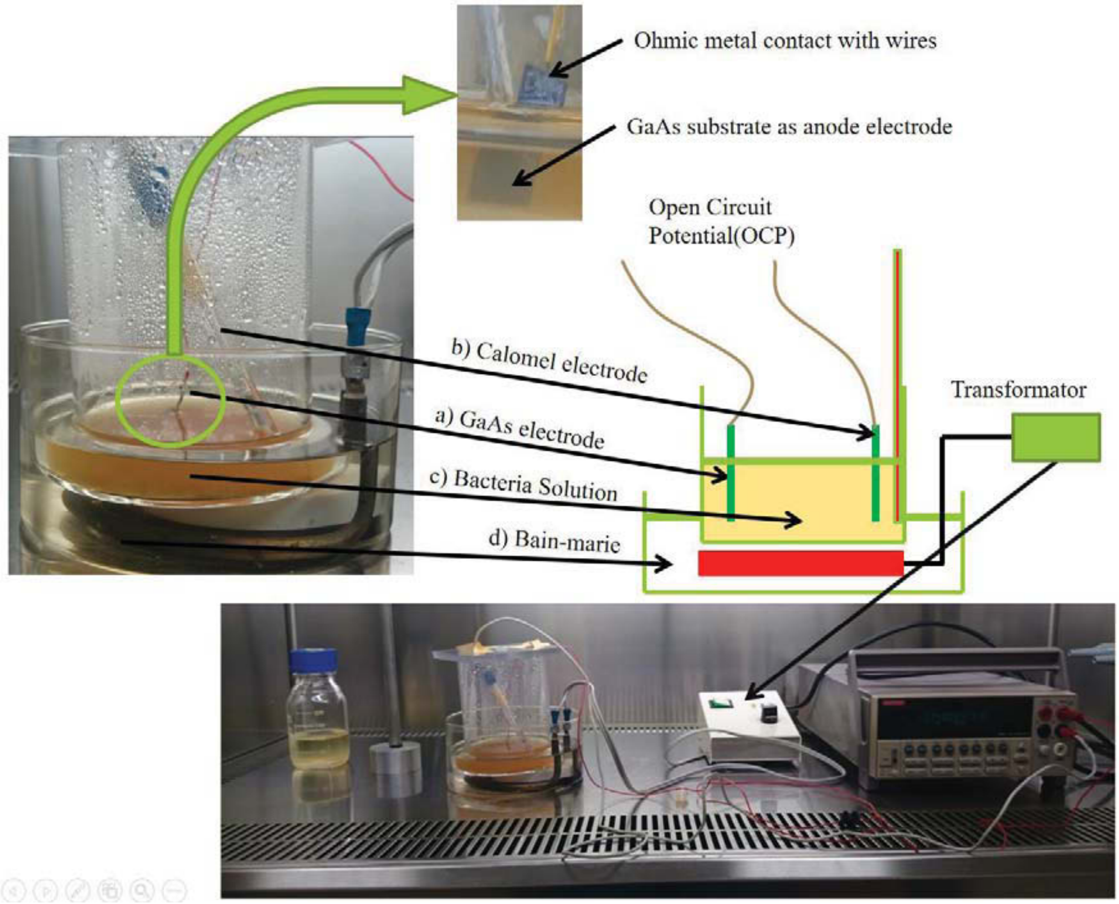

Fig. 2.6: MFC prototype and schematic with all components. Image below shows the MFC prototype connected with potentiometer. An illustrated prototype structure is shown on the right side of the zoom photo. Half-immersed GaAs electrode in bacteria solution is the view zoomed above.

The most important component in our system is the GaAs (100) substrate used as the anode. In the following three sections, the preparation of this GaAs anode will be described including the growth of GaAs nanowires by gold-catalyst HVPE process.

The bacteria selected here was the *Algoriphagus* strain supplied by INP Toulouse for its electrochemical activity. The measurements obtained on this preliminary prototype will be presented and discussed in section 2.3.2.

2.4.1 MFC anode preparation

In order to understand the operating mechanism of the bacteria solution with different anodes, we prepared two GaAs substrates, shown in Fig. 2.7, without nanowires, for preliminary testing of the electric potential of our prototype:

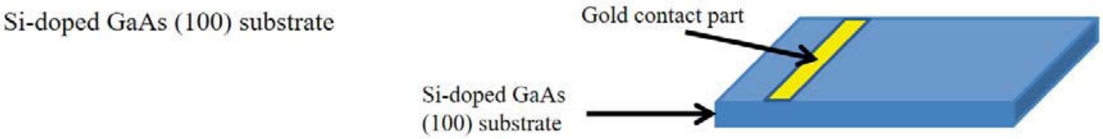

Fig. 2.7: GaAs substrate tested in the prototype. Commercial Si-doped GaAs (100) substrate, carrier concentration is about 2.0×10^{18} cm^{-3}.

The surface of the GaAs (100) substrates was fixed to 4 cm × 2 cm. This surface was set as a balance between the sensitivity of the system, the easier handling during the manipulation of the electrodes and the fragility of the metal contacts. Commercial Si-doped GaAs (100) is supplied by Wafer Technology LTD with a carrier concentration of 2.0×10^{18} cm^{-3}.

Ohmic contact part (mentioned as “Gold contact” in Fig. 2.7 and following figures) is realized by thermal evaporation of noble metal gold (Au) and germanium (Ge) by Dr. C. Varenne. Before thermal evaporation, all GaAs substrates are cleaned in methanol then ethanol. After cleaning, the sample is mounted in the evaporator chamber. Once the sample is mounted, it is heated from ambient temperature to 100 °C. Finally, evaporation of contact metals is done through a stainless-steel mask at a rate of (0.5±1) Å sec^{-1} and background pressure around 10^{-6} Torr. Evaporated metals and their thickness are: Au 100 Å/Ge 350 Å/Au 1000 Å. After the evaporation process, the sample is annealed under a hydrogen atmosphere with sequence of 200°C (for 3 min), 250°C (for 1 min) and 300°C (for 1 min).

2.4.2 MFC prototype potential measurement with bacteria

A digital potentiometer was used to test the MFC prototype. We can measure the open circuit potential (OPC) between two electrodes (Si-doped GaAs as anode and calomel electrode) immerged in the bacteria solution. Si-doped GaAs substrate anode as shown in

Fig. 2.7 was tested. Electrode in Fig. 2.7 was chosen as a standard electrode because of its high doping level (2.0×10^{18} cm^{-3}).

As shown in Fig. 2.6, MFC prototype was implemented in a biological safety cabinet with fresh *Algoriphagus* bacteria solution. With Si-doped anode (electrode in Fig. 2.7), the measurement lasted 10 days nonstop. Data were collected manually every day.

We first identified which were the key parameters measured during the MFC test. There are some concepts to be clarified. In a MFC, electricity is generated only if the overall reaction is thermodynamically favorable, *i.e.* if the Gibbs free energy $\Delta G_r^0 < 0$ is negative (spontaneous reaction) [12]. For this MFC prototype, this relation can be written as:

$$E_m = E_{emf}^{0'} - E_{Cal} + E_{GaAs(°C)} \qquad (2.3)$$

where

E_m : Potential measured by potentiometer

$E_{emf}^{0'}$: Maximum electromotive force of the *Algoriphagus* bacteria

E_{Cal} : Reference potential of Calomel (240 mV)

$E_{GaAs(°C)}$: Potential of N-type GaAs semiconductor at 303 K

E_m is the only data we measured directly in this test, which is read from the screen of the potentiometer. All other data have to be calculated to obtain $E_{emf}^{0'}$.

According to B.E. Logan [12], $E_{emf}^{0'}$ can be expressed for any type of battery or fuel with the Nernst equation as:

$$E_{emf} = E^0 - \frac{RT}{nF}\ln(\mathrm{Q}) \qquad (2.4)$$

where

R: Universal gas constant (8.31447 J mol^{-1} K^{-1})

F: Faraday's constant (9.64853×10^4 C/mol)

n: Number of electrons per reaction mol.

The reaction quotient Q is the ratio of the activities of the products divided by activities of the reactants raised to their respective stoichiometric coefficients, *i.e.*, $Q = \frac{a_{Red}^y}{a_{Ox}^x}$ for any electrochemical half-cell reaction of the form $xOx + ne^- = yRed$. a_{Ox} and a_{Red} are the chemical activities of oxidants and reductants of the redox half-cell equation.

E^0 is the standard cell electromotive force or standard electrode potential. This value depends only on the reaction in the bacteria solution. E^0 can be analyzed in terms of the half-cell reactions, which is the separate reaction occurring at the anode and the cathode. If we look at IUPAC convention, E^0 (at T = 298 K, P = 1 bar, C as [chemical concentration] = 1M) is reported as a reduction potential where the reaction is expressed in the direction where electrons are consumed [25]. If acetate is oxidized at the anode by bacteria, the reaction 2.1 given in section 2.2 is the reaction that occurs at the anode:

$$2HCO_3^- + 9H^+ + 8e^- \rightarrow CH_3COO^- + 4H_2O \qquad \text{Anode reaction (2.1)}$$

And if we formulate that oxygen is used as the electron acceptor for the reaction, the reaction 2.2 given in section 2.2 is the reaction that occurs at the cathode:

$$\tfrac{1}{2}O_2 + 2H^+ + 2e^- \rightarrow H_2O \qquad \text{Cathode reaction (2.2)}$$

For a normal MFC (air-cathode MFC for example), we can give the calculations for two anode and cathode electrodes as in Fig. 2.8.

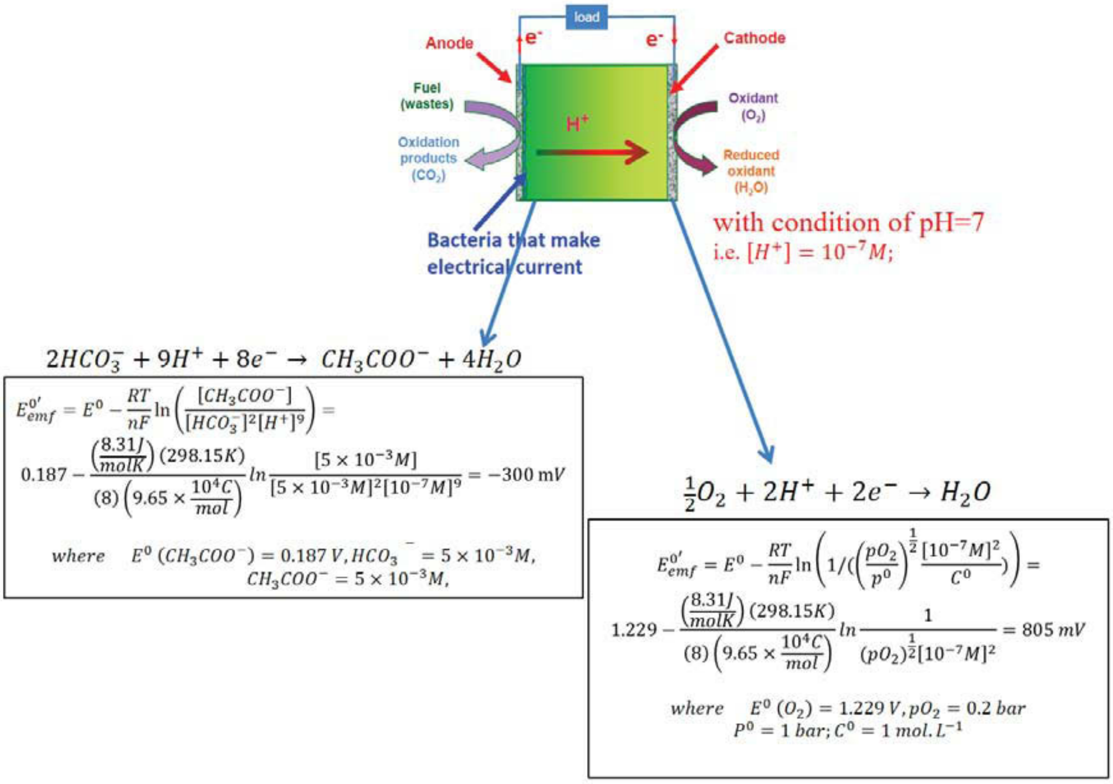

Fig. 2.8: Calculation of standard electrode potential for a normal air-cathode MFC.

$E^0(CH_3COO^-)$ and $E^0(O_2)$ were the standard potentials for typical conditions in MFCs [12]

where

$$\mathrm{E_A} = \mathrm{E_{emf}^{0'}}\,(\mathrm{Anode}) = -300\ \mathrm{mV} \quad (2.5)$$

$$\mathrm{E_C} = \mathrm{E_{emf}^{0'}}\,(\mathrm{Cathode}) = 805\ \mathrm{mV} \quad (2.6)$$

So we can have:

$$E_{emf}(theory) = E_c - E_A = 805 - (-300) = 1105\,mV \qquad (2.7)$$

This $E_{emf}(theory)$ shows that the maximum MFC voltage which is attainable in Ref. [12] is on the order of $1.1V$.

For our MFC prototype, two situations can occur. Whether we have an air-aqueous cathode effect, or this effect is negligible. For the latter situation, electron creation with time will rise the pH in solution.

A $E_{GaAs(°C)}$ was measured by potentiometer with *Algoriphagus* bacteria, resulting as -0.21 V for Si-doped GaAs (100) electrode (a). $E_{GaAs(°C)}$ could be expressed by equation (2.8) [26] where:

$$E_{GaAs(°C)} = V_{OC} = \frac{kT}{q} ln\left[\frac{(N_A + \Delta n)\Delta n}{n_i^2}\right] \qquad (2.8)$$

We can calculate the theoretical value of open circuit potential (OCP) from these two cases:

with air-aqueous cathode we have

$$E_m(theory) = E_+ - E_{-cal} + E_{GaAs(°C)}$$

$$= \ (805 + 300) - 240 - 210 = 655\, mV \qquad (2.9)$$

where $E_+ = E_{emf}(theory) = E_c - E_A$

$$= 805 - (-300) = 1105\, mV \qquad (2.7)$$

The values of E_c and E_A are given by ref E_{-cal} which was contacted to the negative plate of the potentiometer. If now we consider the situation with a feeble cathode, where the effect of $E_c \approx 0$, equation (2.7) will become:

$$E_{emf}(theory) = -E_A \qquad (2.10)$$

and we have

$$E_m(theory) = E_+ - E_{-cal} + E_{GaAs(°C)} = -E_A - E_{-cal} + E_{GaAs(T)}$$

$$= \ 300 - 240 - 21 = -190\, mV \qquad (2.11)$$

As a summary for the theoretical results, we can conclude that: (1) with air-cathode, theoretical open circuit potential should be around $655\, mV$ (equation 2.8); (2) with a feeble cathode, theoretical values should be around $-190\, mV$ (equation 2.11). These two theoretical results correspond to the E_m value which is measured directly by the potentiometer in the MFC prototype.

The actual measuring data are shown in Fig. 2.9.

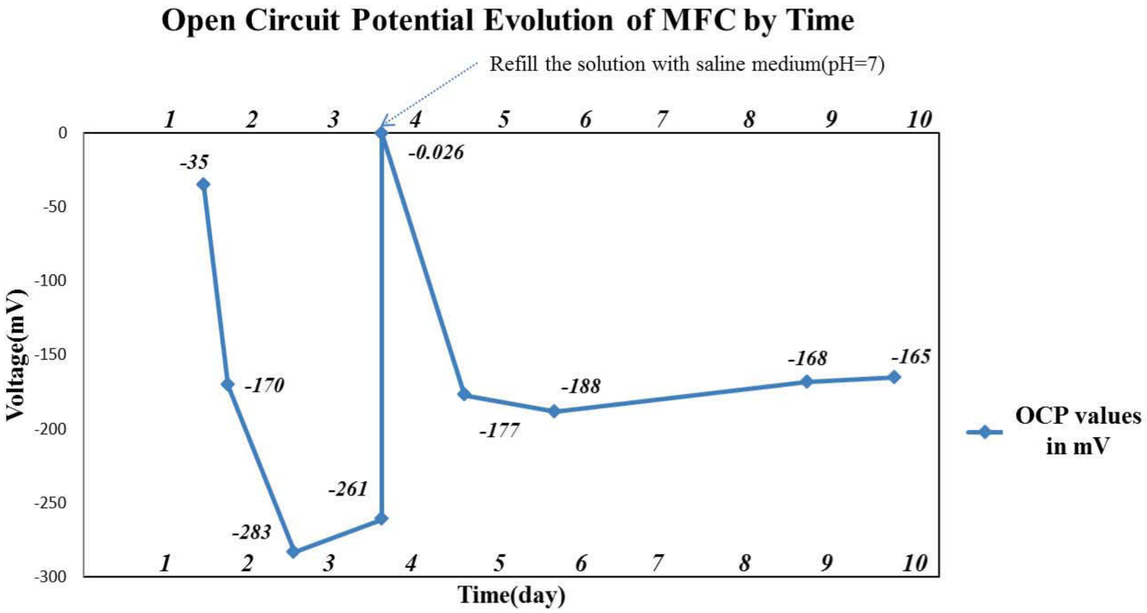

Fig. 2.9: Open circuit potential E_m measurement evolution with Si-doped GaAs anode in ten days.

We can see that the measured potential curve (Fig. 2.9) reached its maximum value at day 2 (minimum negative potential), then E_{emf} potential went smoothly down. The point at the lower value in Fig. 2.9 is the one corresponding to the highest electron charge carrier exchange. To apprehend these measurements, attention should be placed on the biofilm formation as represented in Fig. 2.4 in section 2.2.1. From day 1 to day 2, the development of bacteria should correspond to stage 1 to stage 5, where in stage 5 the production of electron reaches its minimum peak value (-283 mV) and thus we have measured a negative minimum for E_m.

A peak between day 3 and day 4 indicates the refill of saline medium (nutriment for bacteria), the production of electrons from bacteria was stopped suddenly, and returned to normal tendency the following day. However, the electron creation efficiency continuously decreased after the second day was still go down since the second day. This might mainly due to the pollution of the microbial solution, which induced the competition between the foreign bacterial colonies and the *Algoriphagus* bacterial biofilm on the GaAs substrate.

Our measured peak potential of MFC was $E_{m(max)} = -283\,mV$ and $E_{m(Average)} = -185\,mV$ which were very close to the result in equation 2.10 $(E_m(theory) = -190\,mV)$.

As a summary, the experimental measured results of the MFC prototype with Si-doped GaAs electrode (a) are coherent with the theoretical calculated results.

Table 2.1 gives a summary of all results with electrode (a).

Components	Equation	Potential(mV)
E_A: maximum electromotive force of the *Algoriphagus yeomjeoni* bacteria on anode	$2HCO_3^- + 9H^+ + 8e^- \rightarrow CH_3COO^- + 4H_2O$	$-300\,mV$
E_c: maximum electromotive force of the *Algoriphagus yeomjeoni* bacteria on cathode	$\frac{1}{2}O_2 + 2H^+ + 2e^- \rightarrow H_2O$	$805\,mV$
E_{emf}: total maximum electromotive force of the *Algoriphagus yeomjeoni* bacteria	$E_{emf} = E^0 - \frac{RT}{nF}\ln Q$	$1105\,mV$
E_{Cal}: Reference potential of Calomel		$240\,mV$
$E_{GaAs(°C)}$: Potential of N-type GaAs semiconductor at 303 K	$E_{GaAs(°C)} = V_{OC} = \frac{kT}{q} ln\left[\frac{(N_A + \Delta n)\Delta n}{n_i^2}\right]$	$210\,mV$
$E_m(theory)$ with air-aqueous cathode (OCP)	$E_m(theory) = E_c - E_A - E_{-cal} + E_{GaAs(°C)}$	$655\,mV$
$E_m(theory)$ with feeble cathode (OCP)	$E_m(theory) = -E_A - E_{-cal} + E_{GaAs(°C)}$	$-190\,mV$
$E_m(Average)$ measured with potentiometer (OCP)		$-185\,mV$

Table 2.1: Summary of electric potential measurements and calculation with Si-doped GaAs (100) electrode in MFC prototype.

Although the measurements are generally coherent with the theoretical calculations, the pollution of the microbial solution is still a serious influent factor for the electric potential measurement. And this is an intrinsic default related to the design of the MFC prototype. This task will be addressed later in this project (after my PhD). One solution should be to use a sealed container to prevent the contamination from air. In order to understand with more accuracy the functionality of the GaAs electrode in aqueous environment, we decided to conduct a series of electrochemistry analysis with various kinds of GaAs electrodes.

2.5 Electrochemistry ability analyses

2.5.1 GaAs electrodes for electrochemical analyses

In the previous section, we have validated that electron exchange occurs between a biological solution and the surface of the GaAs semiconductor material. The following section is dedicated to "electrochemistry ability analyses" to obtain an accurate control of the chemical oxydo-reduction reactions that take place on the surface of the GaAs material. It constitutes a preliminary work to study the behavior of the GaAs nanowire electrode in an aqueous biological environment. This environment is simulated by an electrolyte solution composed by iron ions in a controlled pH solution.

In order to address more specific properties of different anodes, five GaAs samples (including electrode presented in the previous section) were prepared for testing their electrochemistry ability (see figure 2.10). These five electrodes simulated electrochemical properties of different bacteria incubation electrodes. They were a) Si-doped GaAs (100) substrate (used in the previous section), b) Si-doped GaAs (100) substrate with biofilm, c) undoped GaAs (100) substrate, d) undoped GaAs (100) substrate with a low-doped GaAs planar layer grown by HVPE, e) Au-catalyzed GaAs nanowires grown by HVPE on undoped GaAs (100) substrate.

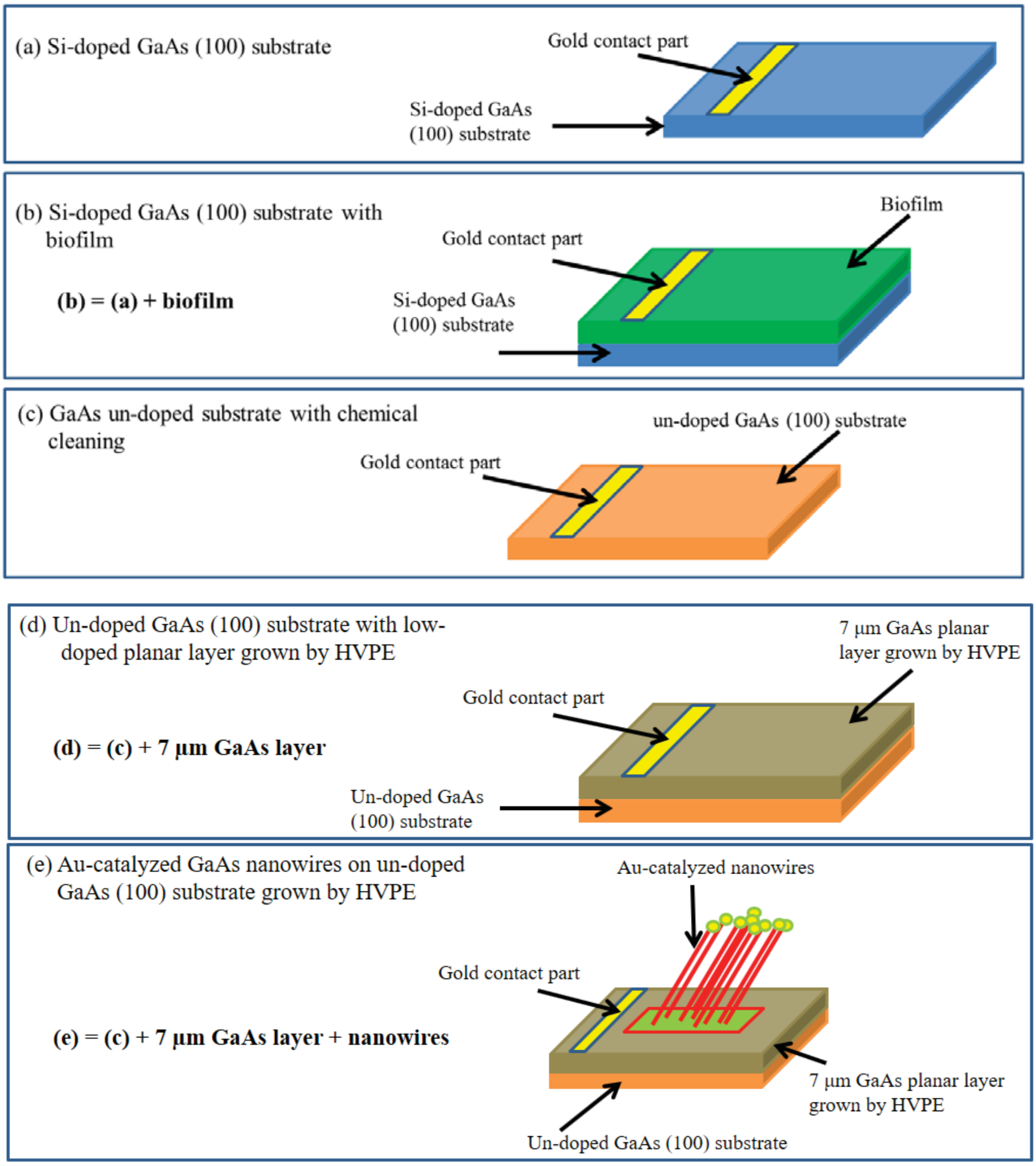

Fig. 2.10: Summary of the five GaAs electrodes tested for their electrochemistry abilities. (a) Si-doped GaAs (100) substrate, (b) Si-doped GaAs (100) substrate with biofilm, (c) undoped GaAs (100) substrate, (d) undoped GaAs (100) substrate with low-doped GaAs planar layer grown by HVPE, (e) Au-catalyzed GaAs nanowires grown by HVPE on undoped GaAs (100) substrate.

Electrode (a) is the substrate part of electrode (b); electrode (c) is the substrate part of electrode (d); and electrode (d) is the first two grown structures (GaAs substrate and planar layer) without nanowires in electrode (e). This experimental protocol gave us the possibility to analyze from part to part the electrochemical properties of different electrodes. We will first discuss the preparation of electrode (e) with gold-catalyzed GaAs nanowires.

2.5.2 Preparation of electrode (e) – Gold-catalyzed GaAs nanowires

In Chapter 1, self-catalyzed growth of GaAs nanowires on silicon has been detailed, and we showed that the main issue was the very low NW density. To address the biocompatibility of GaAs nanowires, we chose to grow GaAs nanowires by gold-assisted HVPE process. This process mastered by the HVPE group is capable to provide arrays of GaAs nanowires with high density and low resistivity. The feasibility of gold-catalyzed growth of GaAs nanowires by using HVPE has been demonstrated in 2010. Nanowires showed an exceptional length with respect to other epitaxial techniques. Length varying from 40 to 200 μm are obtained at an axial growth rate of some 180 μm/h. Pre-deposited gold layer is annealed to form nanoscale gold catalyst droplets, from which nanowires grow [27] with a defect-free cubic ZB phase whatever the NW radius is [28].

Nanowires growth was performed on GaAs (100) substrate -4° off toward (-110) direction. A quantity of gold equivalent to one-tenth of a monolayer was deposited on the substrate in an ultra-high vacuum chamber. The growth temperature was fixed at 715 °C. The partial pressure of GaCl and As_4 were fixed at 300 Pa and 71 Pa. With these experimental conditions, the growth rate of the planar layer is 36 $\mu m.h^{-1}$ for GaAs (100).

Once the GaAs substrate was introduced in HVPE, it was heated at the growth temperature with hydrogen. This annealing step was maintained for one hour at 715 °C in order to create Au-Ga droplets with diameters between 10 to 50 nm.

A post-growth SEM image is shown in Fig. 2.11. We can observe two types of objects grown by the VLS mechanism: 1) giant hexagonal structures 50 µm-long and spindled, named “scales” with a gold droplet on the top; 2) thin nanowires grown from the lateral faces of the scales, oriented along the (111)B direction with a length between 10 to 50 µm.

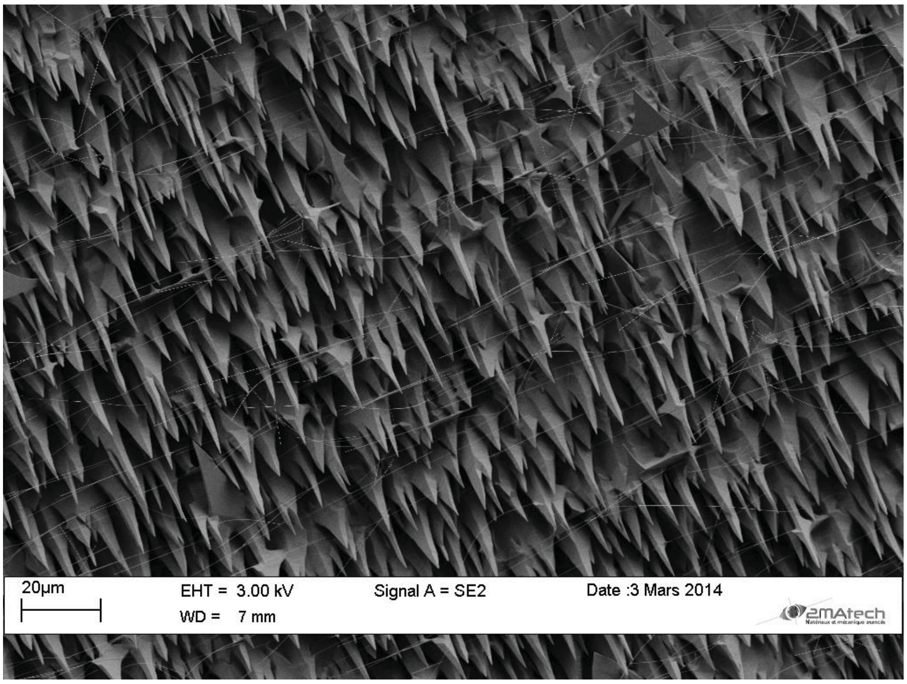

Fig. 2.11: SEM image of a GaAs (100) substrate after gold-catalyzed VLS-HVPE growth of GaAs nanowires.

Details related to gold-catalyzed growth of nanowires by HVPE were thoroughly described in several publications of the group [28-29]. We will focus here on the experimental procedure performed during my PhD to provide the nanowire electrode (e) of Fig. 2.10.

As a matter of fact, the implementation of (e) electrode was the main difficulty during this study. To preserve the gold contact zone, a three-steps growth process was carried out with the help of our team engineer, D. Castelluci. This process includes: (1) gold deposition thanks to the design of an adequate mask for the GaAs (100) substrate; (2) HVPE Au-catalyzed nanowire growth; (3) gold contact zone deposition inside the evaporator with second designed mask, to avoid the metal contamination of the nanowires during the deposit of metal contacts. A diagram of the protocol is presented in Fig. 2.12.

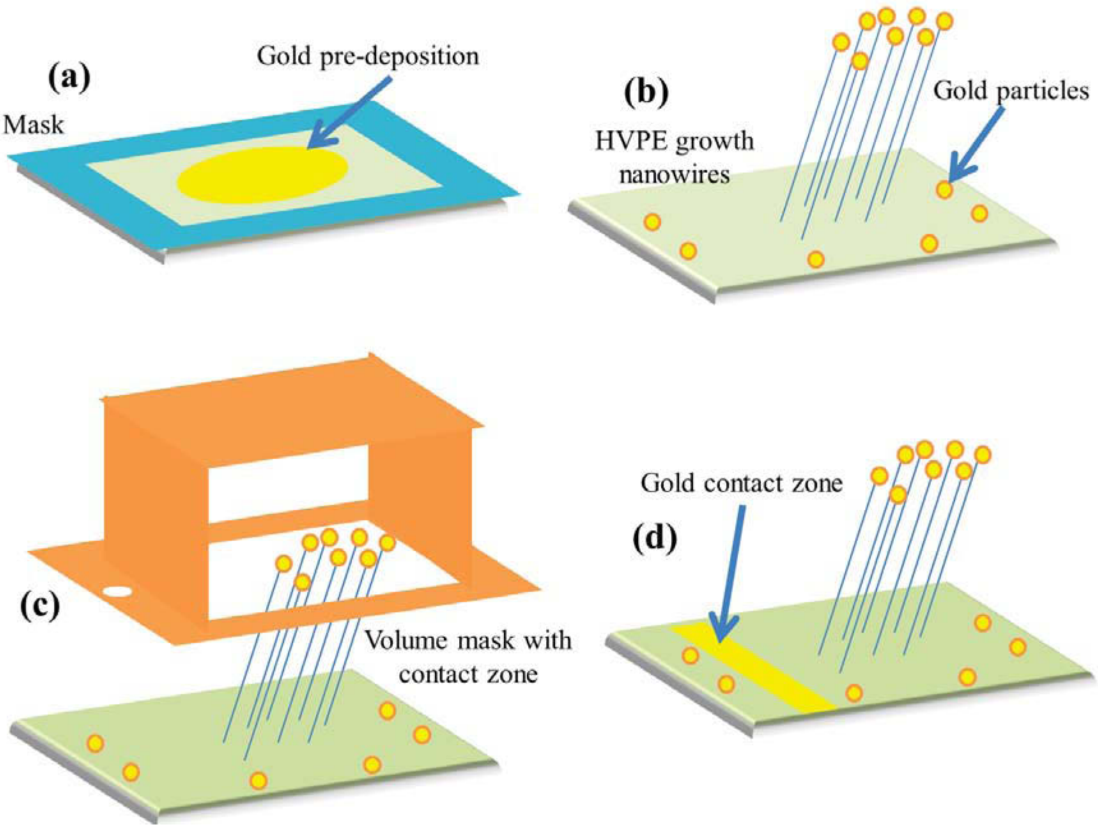

Fig. 2.12: Preparation of the nanowires electrode (e) of Fig. 2.10. (a) Gold deposition with a first mask on the GaAs (100) substrate; (b) HVPE Au-catalyzed nanowires growth; (c) gold contact zone deposition inside the evaporator with a second mask, to avoid metal contamination of the nanowires; (d) final step for gold contacts.

The gold contact zone shown in Fig. 2.12 (d) is the ohmic contact zone for nanowires. The five electrodes described in Fig. 2.10 were all tested by electrochemical analysis with Solartron 1250E/1287 system for cyclic voltammetry, and impedance spectroscopy analysis, to address the factors that affect power generation in MFCs. These measurements were realized in an electrochemical cell using three electrodes as shown schematically in Fig. 2.13. The three electrodes, working, reference and counter (auxiliary) electrodes, were immersed in a medium solution containing the supporting electrolyte. This electrolyte solution was prepared by mixing 100 ml of 0.5 M KNO_3 as the electrolyte support, 0.01 M iron (II) sulfate/iron (III) sulfate, and pH of 2 was adjusted with H_2SO_4.

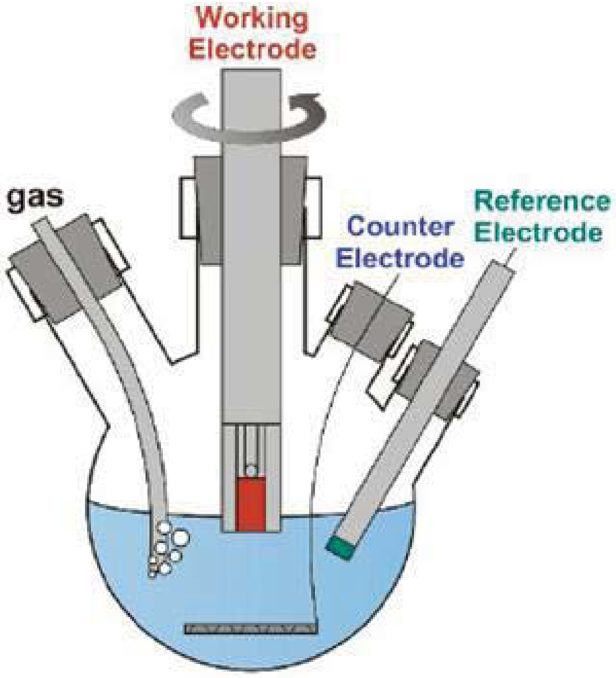

Fig. 2.13: Schematic setup of a three-electrode electrochemical cell. In these cells, the potential is controlled between the working and reference electrodes, while the current is measured between the working and counter (auxiliary) electrodes. The working electrode can be rotated to avoid limitation by transport of the analyte [30]. A magnetic agitator is used during the measurement instead of rotatable working electrode.

The working electrode refers to the GaAs electrodes presented in Fig. 2.10. Reference electrode provides a fixed potential to which the potential applied to the working electrode is controlled, and it consists of a saturated calomel electrode in this test. The counter electrode is often included, and it consists of a platinum wire. Because the reference electrode has a constant potential value, any change in the electrochemical cell is due to the working electrode and thus to the redox process. The three electrodes are connected to the Solartron 1250E/1287 electrochemical analysis system, which controls the potential applied to the working electrode [31]. The gas (nitrogen or argon) showed in Fig. 2.13 is used to deoxygenate the solution.

2.5.3 Cyclic voltammetry

Solartron 1287A potentiostat galvanostat was used to perform cyclic voltammetry (CV). CV test is a widely used electroanalytical method for electroactive species, it is known as a potential controlled method or sweep potential method. CV test will help us to study and to characterize the electron transfer interactions between microorganisms or microbial biofilms and MFC anodes [32-33]. Here we do the CV test with a scan rate of 50 mV.s^{-1} for five electrodes used as anode in the same medium solution, and the results are reported in Fig. 2.14.

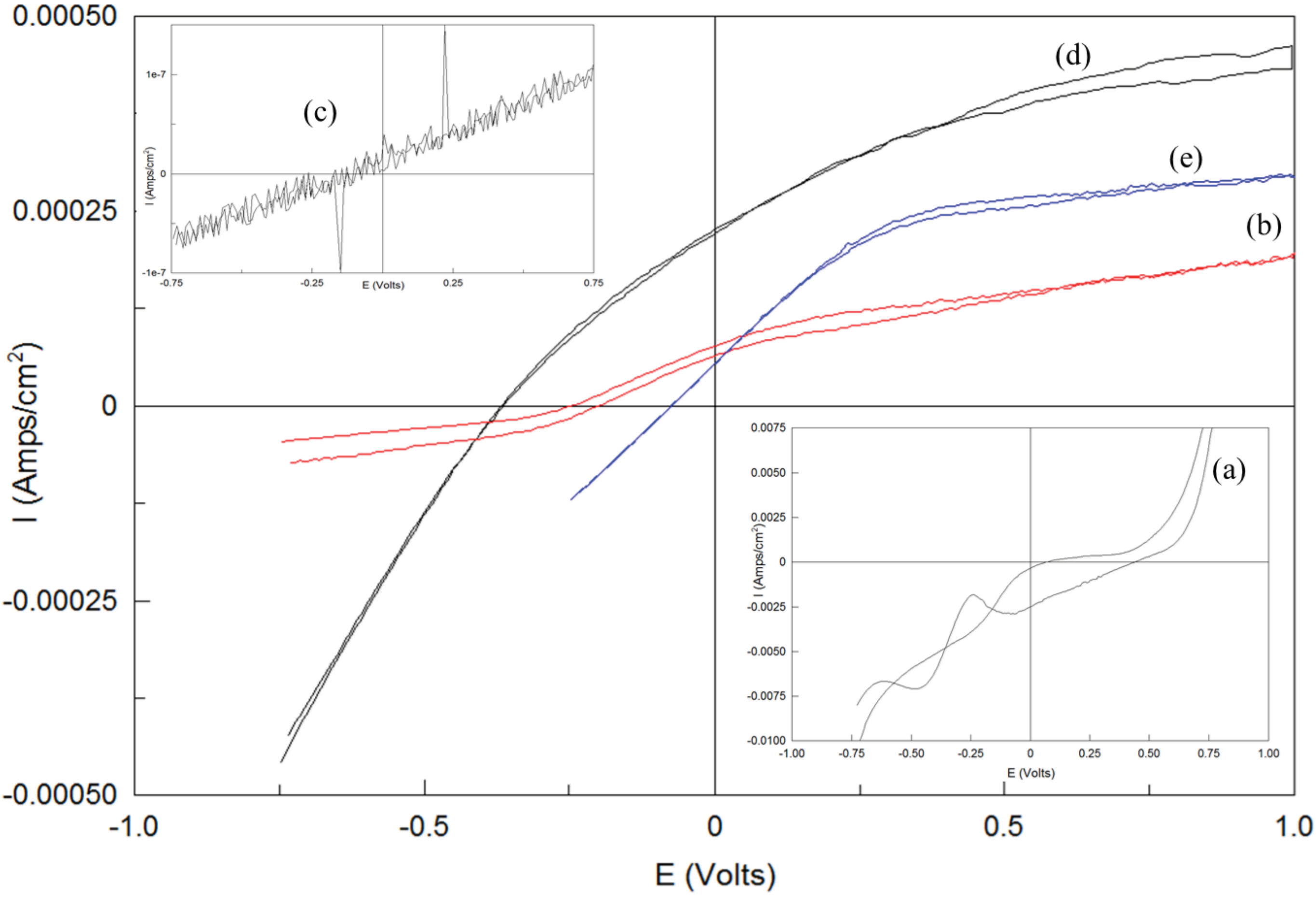

Fig. 2.14: Cyclic voltammetry analysis with five different anodes. I-V curve of the electrolyte redox reactions under triangle wave entrance potential signals from -0.75 to 0.75 V. (a)-(e) refer to the five electrodes in Fig. 2.10. Current (I) range for electrode (a) from -0.05 to 0.15 A.cm^{-2}, for (c) electrode from -1×10^{-7} to 1.5×10^{-7} A.cm^{-2}. Scan rate 50 mV.s^{-1}.

From Fig. 2.14, the peak current of (a) around 0.5 V, where the CV curve is mainly due to water oxidation, was much higher than other electrodes where the polarization resistance (calculated as the inverse of the slope of the I vs. E graph near the Open Circuit potential) is only $R_p = 168\,\Omega.cm^2$. (The units of Ohm.cm^2 here means the capability of our electrode for a given surface. The factors we measured like ion/electron conductivity, diffusion of gases are not linear as a function of the thickness of the electrode but are linear as a function of the surface.) This value is very reasonable for a heavy n-doped GaAs substrate. On the other hand, the very low current (level of 1×10^{-7} A.cm^{-2}) of (c) shows well the intrinsic semiconductor property of an undoped GaAs substrate.

We can also observe that the electrode (d) in Fig. 2.14 of planar layer grown by HVPE (around 7 µm-thick) exhibits a relatively high resistivity ($R_p = 2200\, \Omega.cm^2$) with respect to undoped substrates. This is due to its high carrier concentration (around 1.0×10^{16} cm^{-3}) because of unintentional residual doping inside the HVPE reactor. Due to de-oxidation and coverage of the biofilm, the performance of electrode (c) was encumbered dramatically comparing with electrode (e). And the HVPE nanowires electrochemistry ability was between electrodes (b) and (d). This result is reasonable related to complex interactions among the modules of the electrode (e), such as gold-catalyst, nanowires, GaAs scales, planar layer and Au-contact.

If we look at all the electrodes separately with standard CV curve, we can find that all the electrodes show a voltammogram with the typical sigmoidal characteristic, which is probably based on one single underlying redox center [34]. Also, several parameters on the micrometer scale can be easily found from all five semiconductor electrodes, such as diffusion depth, interface of nanowire and electrolyte.

Cyclic voltammetry analysis reveals the electron transfer kinetics, the redox reactions and electrode properties during the ramping potential on the working electrode. The next section will describe the second technique, so called Electrochemical Impedance Spectroscopy (EIS), where a sinusoidal potential is applied at different frequencies around certain equilibrium points that we chose from the CV curve. EIC is an efficient, non-intrusive and semi-quantitative technique to characterize the performance of bio-electrochemical systems such as microbial fuel cells. The contribution of impedance spectroscopy is very significant and appreciable especially in a highly heterogeneous system such as MFCs. The electrochemical interface of MFC is highly complex as the microbes colonize the electrode, or different materials combinations, leading to intricate electrochemical reactions. EIS is also a powerful method to investigate the dynamics of the bound or mobile charges in the bulk or interfacial region of such system [35]. The measured impedance response is simulated by an equivalent electronic circuit in order to be analyzed and correlated to physical properties. EIS analysis allows to describe the interface of the anode, its structure and the reactions taking place there [36].

2.5.4 Impedance spectroscopy analysis and simulation

Electrochemical impedance is measured by applying an AC (Alternating Current) potential to an electrochemical cell and by measuring the resulting current across the cell [37]. With the applied sinusoidal potential $E_t = E_0 + \Delta E sin(\omega t)$ (shown in Fig. 2.15(i)), the induced current is $I_t = I_0 + \Delta I \, sin(\omega t + \varphi)$, where E_t and I_t are the potential and the current at time t; E_0 and I_0 are the amplitudes of the CV curve; $\omega = 2\pi f$ is the radial frequency, and f is the frequency of the signal.

According to Ohm's law, the impedance of the system can be expressed as:

$$Z(\omega) = \frac{E_t}{I_t} = Z' + jZ'' \qquad (2.12)$$

The impedance $Z(\omega)$ has magnitude Z_0 and a phase shift φ. E_0 is the open circuit potential (OCP). An impedimetric spectrum is obtained when a small AC excitation voltage is applied to the system within a frequency range, and this induces an AC current response for each frequency value.

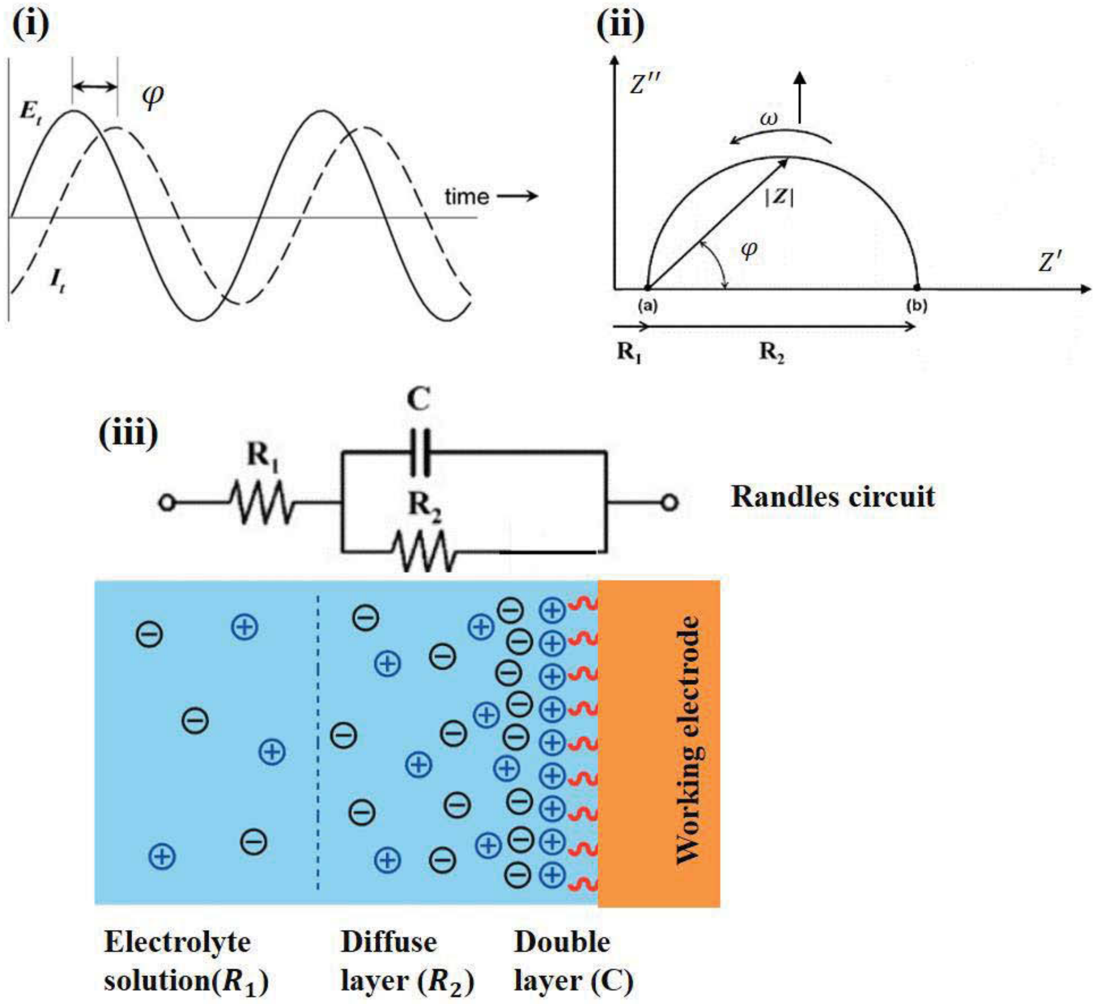

Fig. 2.15: (i) AC excitation signal applied and sinusoidal current response at an electrical system; (ii) a typical Nyquist diagram [38] with (iii) common equivalent electric circuit and its work modelling, R_1 is mainly the Ohmic resistance of the electrolyte solution, R_2 is the charge/electron transfer resistance or the polarization resistance, and C is the double later capacitance [39].

A common way to represent the impedance is a vector model with the real and imaginary axes (Fig. 2.15(ii)). Herein, all the components related to the formation of insulating layer (double layer, barrier) that generate a phase shift (capacitance) contribute to the imaginary part of the impedance Z'', while the other components that do not induce any phase shift (resistance) contribute to the real part Z' [38]. "Nyquist plot", in which the imaginary part Z'' is plotted versus the real part Z' of the impedance, is mostly used to represent impedimetric data. Each data point corresponds to a given frequency. In Fig. 2.15(ii), frequency goes down from left to right. The impedance spectrum profile has a semicircle beginning in the point corresponding to R_1 value (a) and ending in the point (b) corresponding to the sum $R_1 + R_2$ in Fig. 2.15(iii). The value of capacitance of the capacitor C can be obtained by the maximum value of imaginary impedance in the spectrum. The units of C is F/cm^2. Most of impedance spectra corresponding to electrochemical system can be fitted with this type of equivalent circuit: parameter R_1 represents the resistance of the electrolyte, R_2 corresponds in most cases to the polarization resistance between the solution and the electrode surface, and C is the capacitance of the double layer (due to the interface between the electrode and the electrolytic solution) [38]. As shown in Fig. 2.15(iii), R_1 represents the properties of the electrolytic solution and diffusion of the redox probe. R_1 will not be affected by target binding at the electrode surface. R_2 and C are related to the dielectric and insulating features at the electrode–electrolyte interface [39].

A Solartron 1250E impedance/gain-phase analyzer was used to perform the following studies. The measurements were conducted by Dr. Fabrice Audonnet (Institut Pascal, GePEB department) by using the same solution (described in 2.4.2) for frequencies going from 65335 Hz to 0.1 Hz with 10 points/decade. This frequency range is the most suitable working range for the five anodes studied in this section. The analysis is represented as Nyquist plot for previous electrodes response at the analytic redox potential.

One major limitation in the Nyquist plot is that the frequency cannot be explicit by simply looking at the plot. Bode plot overcomes this limitation since the impedance is plotted with the logarithmic frequency plotted on the x-axis and both the absolute value of impedance and the phase angle are plotted on the y-axis [35].

First of all, we perform a function test with a platinum electrode to ensure the reliability of our instrument and solutions. All the data plotting, equivalent circuit fitting and chi-squared value are given by Zview software. The results are represented with both Nyquist plot and Bode plot in Fig. 2.16.

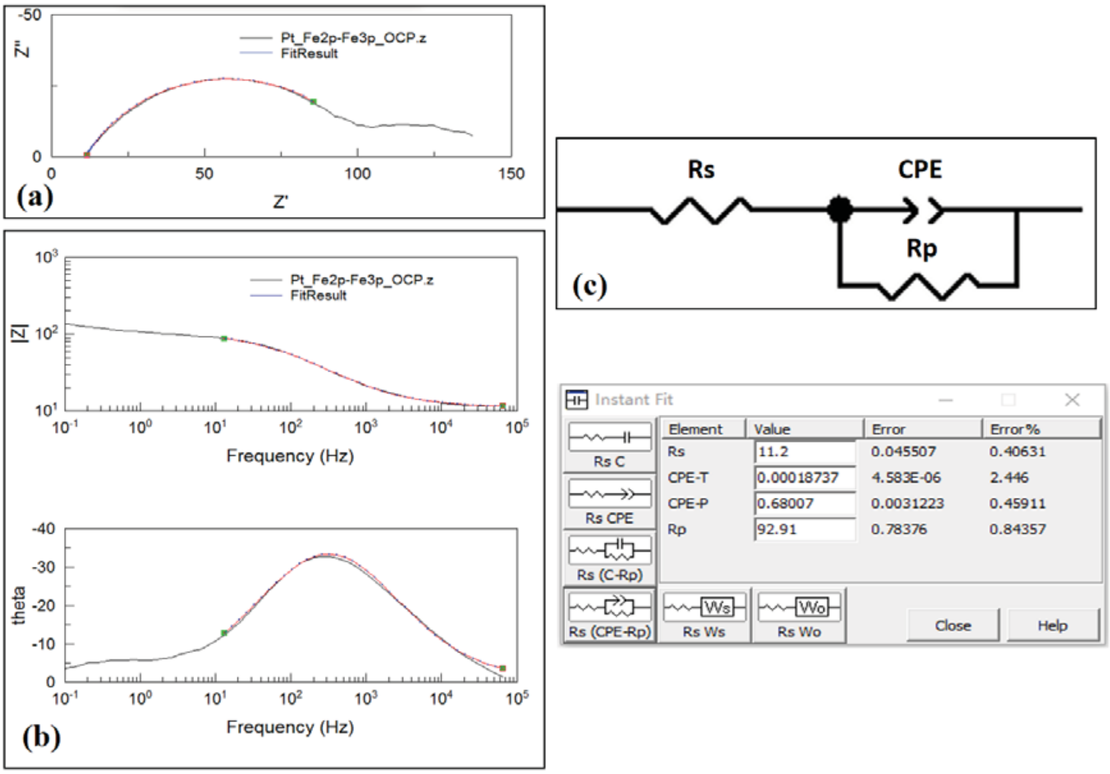

Element	Value	Error	Error%
Rs	11.2	0.045507	0.40631
CPE-T	0.00018737	4.583E-06	2.446
CPE-P	0.68007	0.0031223	0.45911
Rp	92.91	0.78376	0.84357

Fig. 2.16: EIS of a platinum electrode (black curve in (a) and (b)) and its instant fits (red curve in (a) and (b)). (a) is the Nyquist plot, (b) are the Bode plots, (c) is the equivalent instant fit circuit of the electrode, and instant fit results with chi-squared value showed lastly.

We can see from Fig. 2.16 (a) that the platinum electrode performs very similar Nyquist plot comparing with the theoretical one from maximum ω until 13 Hz (green spot in Fig. 2.16). Bode plot in Fig. 2.16 (b) shows that the resistivity magnitude is about $10^2\ \Omega.cm^2$, and only the contribution of one component appears from theta-Hz plot which is a standard sinusoid curve. An instant fit takes place from 65535 Hz to 13 Hz (neglecting the low frequency noise), the $Rs(CPE-Rp)$ equivalent circuit (Fig. 2.16(c)) fits well with EIS graphic. Because of the non-ideal behavior of most capacitors in electrochemical systems under study, the results in impedimetric spectra are semicircles of Nyquist diagram with a depressed and not symmetric shape. This is mainly due to the impact of different species reaching on the surface. To improve the fit of the experimental data, the use of a Constant Phase Element (CPE) instead of a capacitor is required [40-41].

The impedance of a CPE is given by:

$$Z(\omega) = (j\omega)^{-\alpha}/C \qquad (2.13)$$

where ω is the radial frequency. C is the capacitance, and α is an empirical coefficient, and $0 \leq \alpha \leq 1$. For a constant phase element exponent $\alpha < 1$, since $\alpha = 1$ corresponds to the ideal capacitor. Generally, the double layer (component C in Fig. 2.15(iii)) between the solution and the electrode surface is better fitted by a CPE than a capacitor.

The impedance analysis was applied to the electrodes reported in Fig. 2.10. We can first classify the five electrodes ((a) to (e) in Fig. 2.10) to facilitate the measurement interpretation. For example, electrode (a) would be the first layer of electrode (b); (c) will be the lower part of (d); meanwhile the electrode (d) is the first two-layer structures of electrode (e). Hence, the following EIS graphics and discussions will be given based on above referenced relation. Nyquist plot, Bode theta plot (most representative graphic to figure the electrode structure) and equivalent circuit are given. Low frequency noise is neglected for all the plots.

The EIS plots of (a) and (b) electrodes are given in Fig. 2.17.

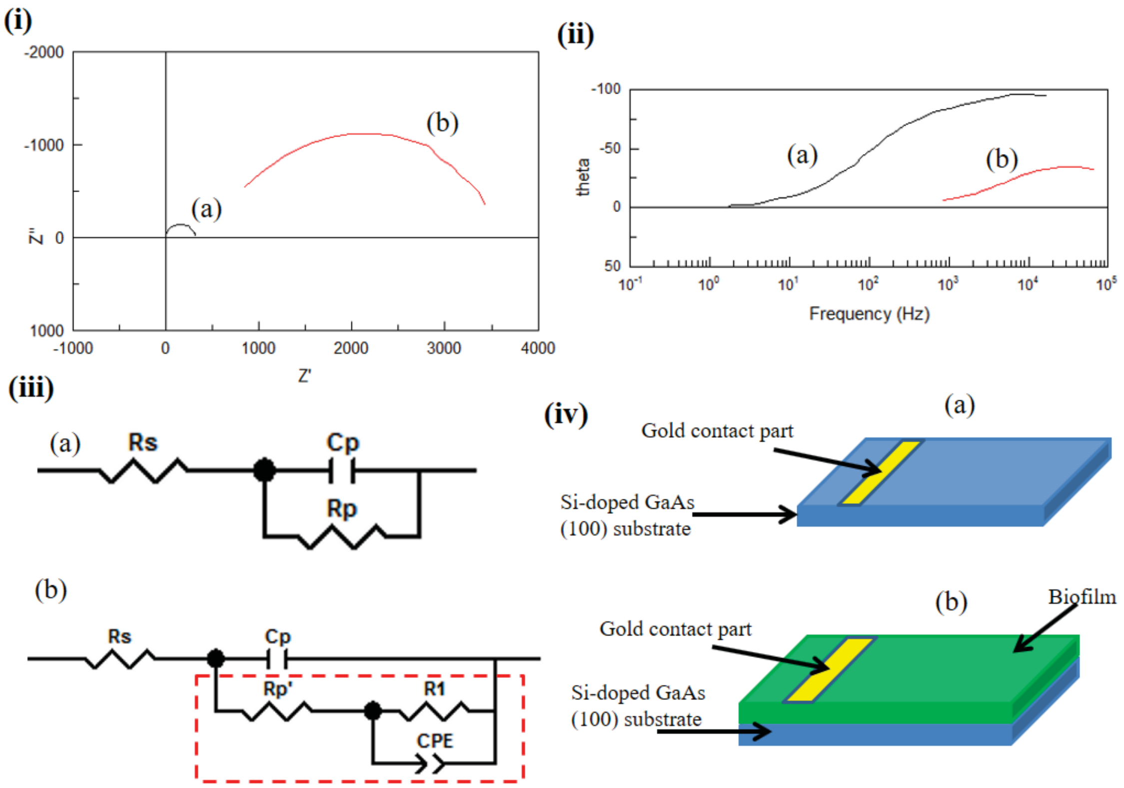

(v)

Equivalent circuit (iii)-(a)		Equivalent circuit (iii)-(b)	
Elements	Values	Elements	Values
Rp	310 Ω.cm²	Rp'	550 Ω.cm²
Rs	~ 0 Ω.cm²	$R1$	3167 Ω.cm²
C	~ 0	$\alpha - CPE$	0.799

Fig. 2.17: Si-doped GaAs (100) electrode (a) and biofilm covered-Si doped GaAs (100) electrode (b) (i) Nyquist plot, (ii) Bode theta plots, (iii) equivalent circuits and (iv) electrode structure and (v) fitting results of their components.

The Rs (solution resistance) of electrode (a) is nearly zero as shown in Fig. 2.17 (i) - (a), and can be well fitted with Cp/Rp system as Cp a pure capacitance. The value of Rp (polarization resistance) shown in (v) in electrode (a) is only about $310\ \Omega.cm^2$. On the contrary, since the occupation of biofilm on electrode (b) is very uniform, all the ions exchanges must traverse this biofilm to approach the GaAs surface. In that case, we cannot see neither the effect of Rs (too small compare with the Rp' for biofilm), nor the Cp (GaAs is totally covered by the biofilm). Therefore, the equivalent circuit of electrode (b) in Fig.

2.17(iii)–(b) can be considered as the $Rp'(CPE/R1)$ system in dotted frame. $Rp' = 550\,\Omega.cm^2$ is the resistivity of the biofilm, $R1 = 3167\,\Omega.cm^2$ is the polarization resistance of biofilm/GaAs interface.

The Nyquist and Bode plots of electrode (c) are shown in Fig. 2.18.

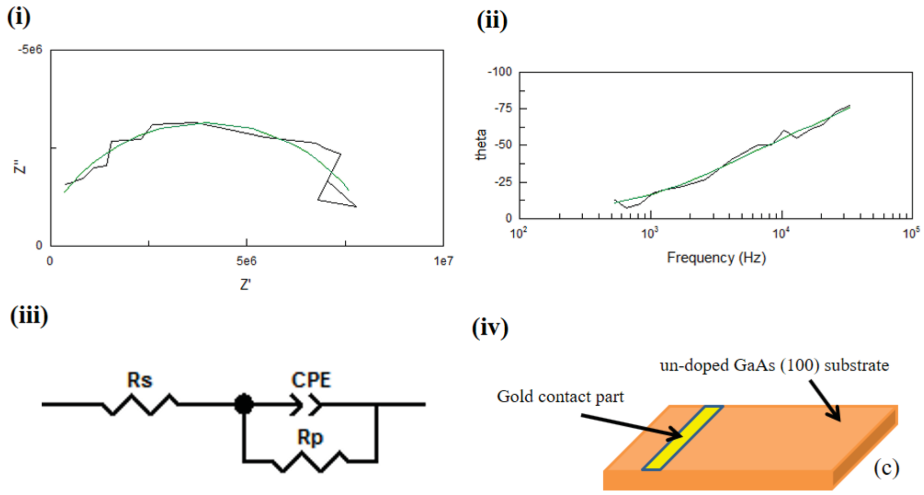

Fig. 2.18: Undoped GaAs (100) electrode (c) (i) Nyquist plot, (ii) Bode theta plot, (iii) equivalent circuits and (iv) electrodes structure.

Because of the blurred curve and a giant $Rp = 8\times10^6\,\Omega.cm^2$, electrode (c) is represented separately in Fig. 2.18. This is due to the intrinsic semiconductor property of electrode (c) as working electrode. Like the modelling of electrode (a), it can be simply modeled with the $Rs(CPE/Rp)$ equivalent circuit. In accordance, the Rs of electrode (c) is near zero, as described in electrode (a) for only the resistivity of electrolyte solution.

The two electrodes (d) and (e) show a structure of many components from the Nyquist and Bode theta plots, especially for the nanowire electrode (e). The Nyquist and Bode plots of electrodes (d) and (e) are shown in Fig. 2.19.

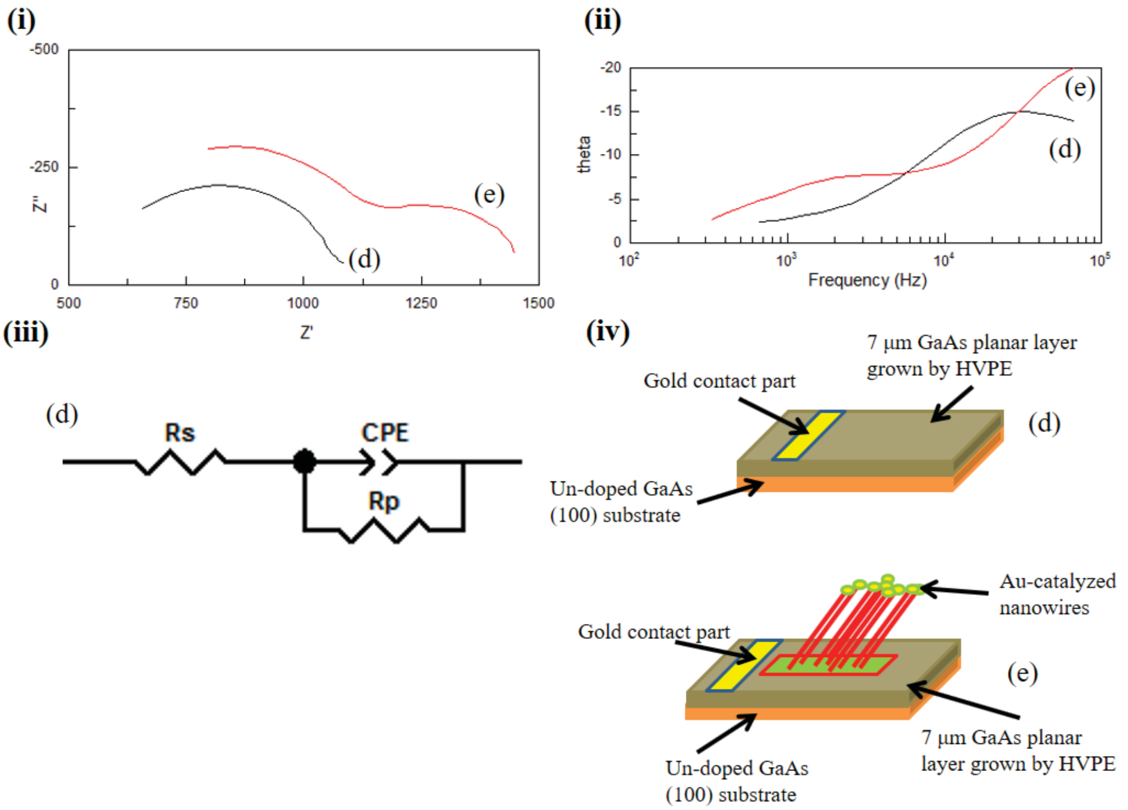

Fig. 2.19: Undoped GaAs (100) electrode with HVPE grown planar layer (d) and Au-catalyzed GaAs nanowires on u-doped GaAs (100) (e) (i)Nyquist plots, (ii)Bode theta plots, (iii) equivalent circuits for electrode (d) and (iv) electrodes structures.

Due to the unintentional doping from HVPE reactor (mentioned in section 2.4.2), the 7 µm-thick HVPE-grown planar layer presents a doping concentration of 1×10^{16}cm^{-3}. This doping reduces the electrode (d) Rp to $577\ \Omega.cm^2$ comparing with the electrode (c) $8\times10^6\ \Omega.cm^2$. Like in electrode (b) with the biofilm, the $Rs = 521\ \Omega.cm^2$ of electrode (d) is influenced by the 2D layer. We can see only one semi-circle in Fig. 2.19 (i)-(d). This indicates that all the exchanges of ions should pass the HVPE planar layer first, and this layer shows a homogeneity in charge exchange in the undoped GaAs substrate surface.

The Nyquist plot of electrode (e) in Fig. 2.19 (i) is the only curve which shows two semi-circles among all five electrodes. This indicates that two transfer mechanisms exist for ions exchange on the working electrode. Two possible equivalent circuits for the nanowire electrode (e) are proposed in Fig. 2.20 (i) and (ii).

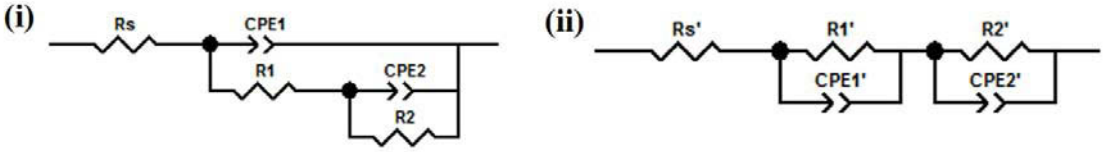

(iii)

Equivalent circuit (i)		Equivalent circuit (ii)	
Elements	Values	Elements	Values
Rs	495.6 Ω.cm^2	Rs'	495.9 Ω.cm^2
$R1$	682 Ω.cm^2	$R1'$	655 Ω.cm^2
$R2$	298.9 Ω.cm^2	$R2'$	325.8 Ω.cm^2
$\alpha - CPE1$	0.901	$\alpha - CPE1'$	0.901
$\alpha - CPE2$	0.900	$\alpha - CPE2'$	0.899

Fig. 2.20: Two possible equivalent circuits (i) and (ii) for Au-catalyzed GaAs nanowires on undoped GaAs (100) (e), and fitting results of their components (iii). $\Omega.\mathbf{cm^2}$ ***is the unit for all resistivity.***

The main difference between this two modeling is the exchange crossing for ions. Circuit (i) represents a one-channel case where all the diffusion will go through GaAs nanowires and then pass the planar layer, which is the typical "coating" representation. Circuit (ii) represents a two-channel situation where the diffusion can choose either nanowires or planar layer as their diffusion passage. $R1$ and $R1'$represent the resistivity of Au-catalyzed GaAs nanowires. If we look at the fitting results shown in Fig. 2.20 (iii), we can find that values for nanowires ($CPE1/R1$ and $CPE1'/R1'$) and planar layer ($CPE2/R2$ and $CPE2'/R2'$) are almost the same. This indicates that the electrochemical behavior of nanowires and planer layer exhibits the same tendency. Additionally, the planar layer has a lower resistivity compared with nanowires. As a matter of fact, the most likely situation is a combination of the two diffusion mechanisms. However at this stage, it is difficult to indicate which one is the dominant effect during the measurement.

A summary containing the structures of the five electrodes, equivalent circuits and fitting results is given in Table 2.2.

<table>
<tr><th>Electrodes structures</th><th>Equivalent circuits</th><th>$Rs, Rp\ and\ \alpha - CPE$</th></tr>
<tr><td>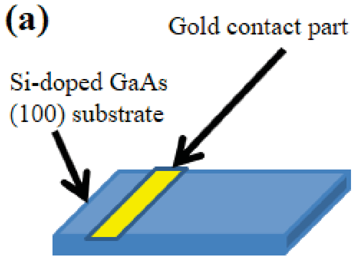 </td><td>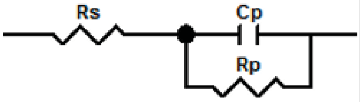 </td><td>$Rs = 0\ \Omega.cm^2$,
$Rp = 310\ \Omega.cm^2$,
$\alpha - CPE = 1$</td></tr>
<tr><td>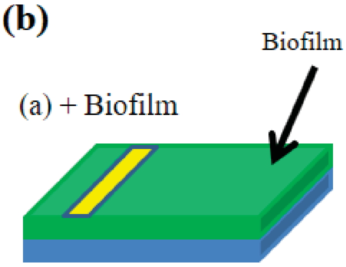 </td><td>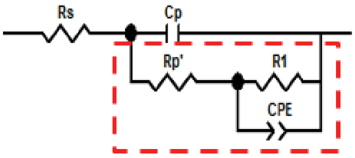 </td><td>$Rs = 550\ \Omega.cm^2$,
$Rp = 3167\ \Omega.cm^2$,
$\alpha - CPE = 0.800$</td></tr>
<tr><td>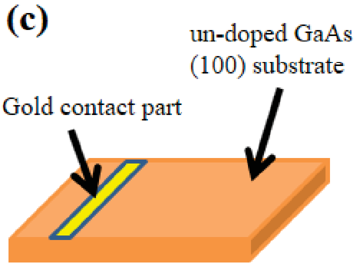 </td><td>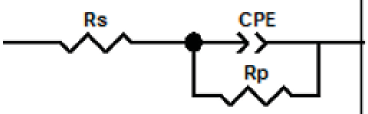 </td><td>$Rs = 0\ \Omega.cm^2$,
$Rp = 9E6\ \Omega.cm^2$,
$\alpha - CPE = 0.801$</td></tr>
<tr><td>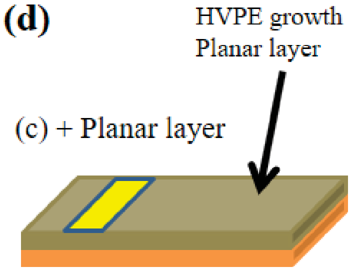 </td><td>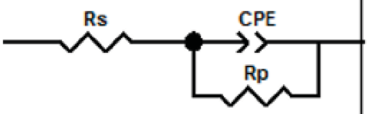 </td><td>$Rs = 521\ \Omega.cm^2$,
$Rp = 577\ \Omega.cm^2$,
$\alpha - CPE = 0.786$</td></tr>
<tr><td>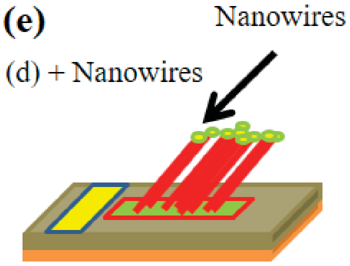 </td><td>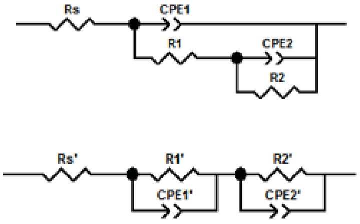 </td><td>$Rs = 496\ \Omega.cm^2$,
$Rp1 = 668\ \Omega.cm^2$,
$\alpha - CPE1 = 0.901$,

$Rp2 = 313\ \Omega.cm^2$,
$\alpha - CPE2 = 0.900$</td></tr>
</table>

Table 2.2: Summary of electrode structures, equivalent circuits and fitting results. For electrode (e), the fitting results of $Rp1/CPE1$ stand for nanowires and $Rp2/CPE2$ for the planar layer.

One can conclude from Table 2.2 that the doping level influences the polarization resistivity significantly. As shown for electrodes (a), (d) and (c), doping in (a) and (d) draws back Rp ten thousand times as compared with (c). The second conclusion is related to the surface state influence: the solution resistivity significantly changes with the morphology of the diffuse layer and the double layer on the working electrode. This property can be seen by comparing electrodes (a) and (b), (c) and (d), or (d) and (e). A further conclusion is that HVPE GaAs nanowires add more diffusion channels for electrolyte ions. This might increase the efficiency of ion diffusion to the working electrode. By summarizing these three points, the doping of the nanowires should enhance the efficiency of electrode (e). Thus, as a perspective before measurements in real conditions in a biological environment, the following section addresses the doping of GaAs nanowires by HVPE.

2.6 Perspective: GaAs nanowire doping with silane (n-type) and diethylzinc (p-type)

The feasibility of GaAs nanowire doping by HVPE was addressed during my PhD for the first time in the group. This section is dedicated to the *n*- and *p*- doping of gold-assisted HVPE-grown nanowires.

The experimental conditions were the standard conditions for temperature and vapor phase composition mentioned in 2.4.2. Dopant precursor during growth are silane for n-type doping and diethylzinc for p-type doping. The fluxes of the two precursors were set to: 5 and 10 cm^3/min for silane, which correspond to planar 2D layers with carrier concentrations of more than 1.0×10^{18} cm^{-3}; 30 and 80 cm^3/min for diethylzinc, corresponding to planar layers with carrier concentrations between 4×10^{18} to 2×10^{19} cm^{-3}. These doping concentrations for both n- and p- were calibrated by Hall Effect Measurements. Today, we do not know the mobility concentration for nanowires (testing in progress thanks to a collaboration with K. Lekhal from Nagoya University in Japan). However, the doping influences drastically the nanowire morphology, as shown in Fig. 2.21 for Si-doped nanowires:

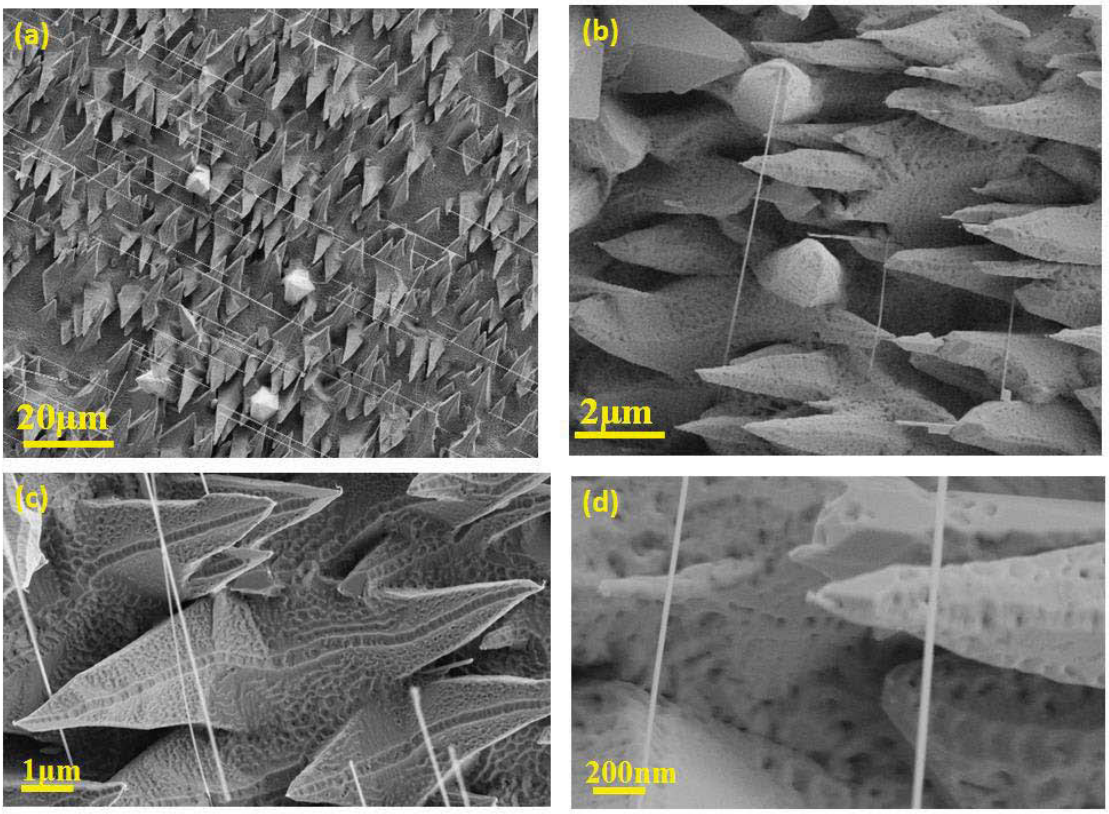

Fig. 2.21: (a) SEM image of undoped GaAs nanowires obtained after 1 hour of growth. (b) SEM image of doped GaAs nanowires with 10 cm^3/min of silane during 1 hour of growth. Note that the density of scales is constant but their length is much smaller for sample (b) than for sample (a), less than 20 µm. The density of nanowires decreases dramatically between (a) undoped, and (b) Si-doped. (c) and (d) Zooms of Si-doped structures. The surface of the scales is porous (see (d)).

The most significant effect of doping on samples is this porous effect on the surface of the scales (see Fig. 2.21). To our knowledge, this etching effect has never been reported yet. One possible explanation could be related to the incorporation of the doping elements during the growth of nanowires as shown in Fig. 2.22.

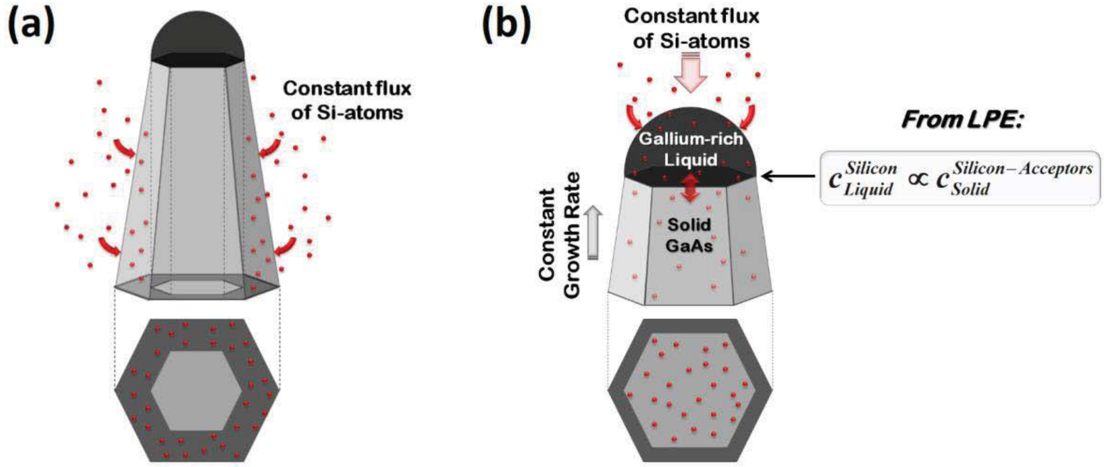

Fig. 2.22: Schematics of two doping mechanisms in nanowires: (a) through deposition on the side facets and (b) through the droplet [42].

The different incorporation pathways (a) through side facets deposition and/or (b) through the droplet seen in Fig. 2.22 might induce this porous effect. The final carrier concentration is still unknown yet.

Zn-atom doping, however, leads to a different post-growth surface morphology, as seen in Fig. 2.23.

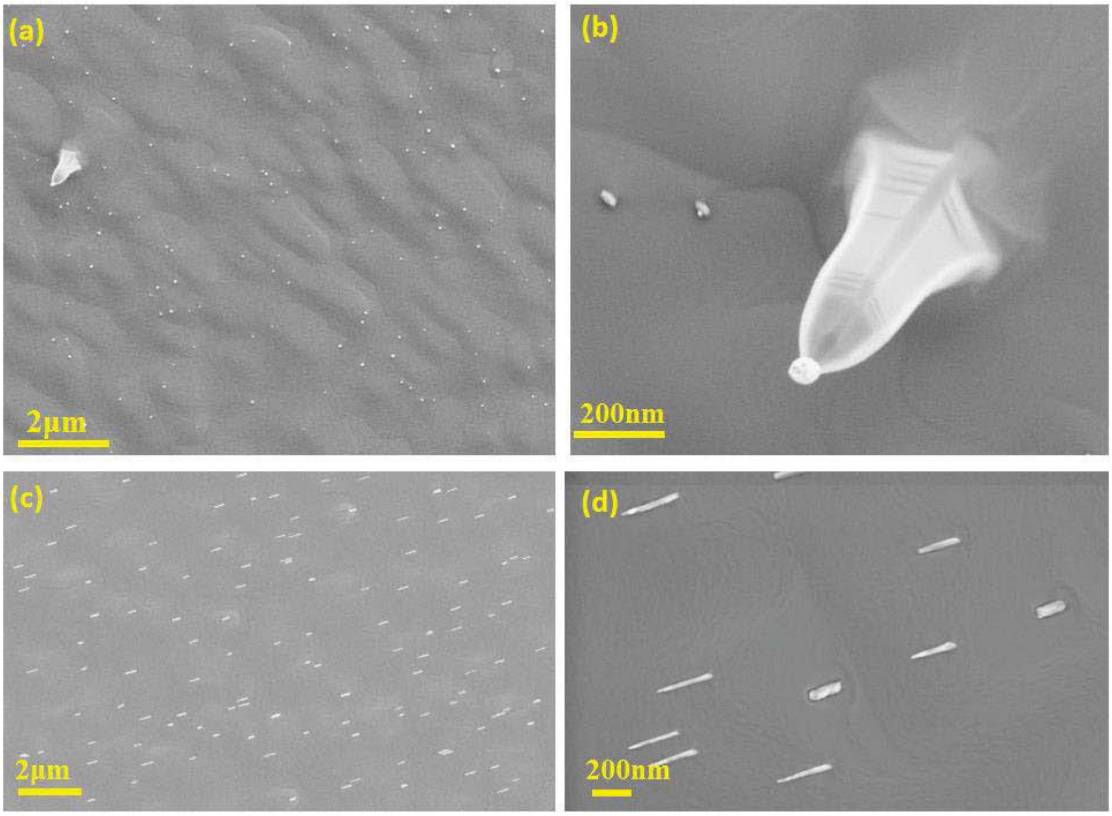

Fig. 2.23: SEM images of doped GaAs nanowires with 30 cm^3/min of diethylzinc (a) and (b) and 80 cm^3/min for (c) and (d).

We can clearly observe that the growth of scales was prevented by the Zn dopant. The nanowire growth was clearly initiated, a low density of NWs was observed. To the best of our knowledge, no such Zn doping effect has been reported for GaAs nanowire growth [43-44]. One possible explanation is that the formation of the scales is limited under Zn precursor, and only 2D growth is favored in this case. Further work will be carry out by the new PhD student pursuing the study.

2.7 Conclusion

In this chapter, we described the motivation for combining GaAs nanowires with biology. Thanks to a collaboration between several researchers from Institut Pascal with different skills in electronics, electrochemistry and biology, I was able to build a first MFC prototype based on GaAs NW array. We tried to develop a first simple MFC prototype with a GaAs substrate electrode. With a long duration measurement of several days inside a bacteria solution, we have obtained preliminary results about the electromotive force of bacteria in contact with GaAs substrates. To simulate with more accuracy the behavior of electron exchange between the bacteria and the nanowires, we decided to perform electrochemistry analysis. A reasonable value of this electromotive force was obtained. An accurate study of GaAs electrodes electrochemistry ability was carried out. Cyclic voltammetry and EIS measurements had shown the specific electrochemistry properties of each GaAs electrode. Another series of nanowire doping tests were conducted in order to reinforce the future nanowires electrode conductivity. The doping of the GaAs nanowires is crucial and we showed that there were critical issues related to the growth with silane and diethylzinc to be resolved, before fabrication of the final prototype working in real biological conditions.

References

[1] F. Akdeniz, A. Çağlar, and D. Güllü, “Recent energy investigations on fossil and alternative nonfossil resources in Turkey,” *Energy Convers. Manag.*, vol. 43, no. 4, pp. 575–589, Mar. 2002.

[2] S. J. Peighambardoust, S. Rowshanzamir, and M. Amjadi, “Review of the proton exchange membranes for fuel cell applications,” *Int. J. Hydrog. Energy*, vol. 35, no. 17, pp. 9349–9384, Sep. 2010.

[3] M. Rahimnejad, A. A. Ghoreyshi, G. Najafpour, and T. Jafary, “Power generation from organic substrate in batch and continuous flow microbial fuel cell operations,” *Appl. Energy*, vol. 88, no. 11, pp. 3999–4004, Nov. 2011.

[4] M. C. Potter, “Electrical Effects Accompanying the Decomposition of Organic Compounds,” *Proc. R. Soc. B Biol. Sci.*, vol. 84, no. 571, pp. 260–276, Sep. 1911.

[5] B. H. Kim, D. H. Park, P. K. Shin, I. S. Chang, and H. J. Kim, *Mediator-less biofuel cell*. Google Patents, 1999.

[6] H. J. Kim, S. H. Moon, and H. K. Byung, “A Microbial Fuel Cell Type Lactate Biosensor Using a Metal-Reducing Bacterium, Shewanella putrefaciens,” *J. Microbiol. Biotechnol.*, vol. 9, no. 3, pp. 365–367, 1999.

[7] N. Mokhtana, W. R. W. Daud, M. Rahimnejad, and G. D. Najafpouv, “Bioelectricity generation in biological fuel cell with and without mediators,” *World Appl. Sci. J.*, vol. 18, no. 4, pp. 559–567, 2012.

[8] K. Rabaey and W. Verstraete, “Microbial fuel cells: novel biotechnology for energy generation,” *Trends Biotechnol.*, vol. 23, no. 6, pp. 291–298, Jun. 2005.

[9] R. K. Thauer, K. Jungermann, and K. Decker, “Energy conservation in chemotrophic anaerobic bacteria.,” *Bacteriol. Rev.*, vol. 41, no. 1, p. 100, 1977.

[10] B. E. Logan, *Microbial fuel cells*. John Wiley & Sons, 2008.

[11] M. Rahimnejad, A. Adhami, S. Darvari, A. Zirepour, and S.-E. Oh, “Microbial fuel cell as new technology for bioelectricity generation: A review,” *Alex. Eng. J.*, vol. 54, no. 3, pp. 745–756, Sep. 2015.

[12] B. E. Logan *et al.*, “Microbial Fuel Cells: Methodology and Technology,” *Environ. Sci. Technol.*, vol. 40, no. 17, pp. 5181–5192, Sep. 2006.

[13] Y. Sharma and B. Li, “The variation of power generation with organic substrates in single-chamber microbial fuel cells (SCMFCs),” *Bioresour. Technol.*, vol. 101, no. 6, pp. 1844–1850, Mar. 2010.

[14] L. Huang, R. J. Zeng, and I. Angelidaki, “Electricity production from xylose using a mediator-less microbial fuel cell,” *Bioresour. Technol.*, vol. 99, no. 10, pp. 4178–4184, Jul. 2008.

[15] S. Wijeyekoon, T. Mino, H. Satoh, and T. Matsuo, “Effects of substrate loading rate on biofilm structure,” *Water Res.*, vol. 38, no. 10, pp. 2479–2488, May 2004.

[16] R. D. Cusick *et al.*, “Performance of a pilot-scale continuous flow microbial electrolysis cell fed winery wastewater,” *Appl. Microbiol. Biotechnol.*, vol. 89, no. 6, pp. 2053–2063, Mar. 2011.

[17] B. Logan, S. Cheng, V. Watson, and G. Estadt, “Graphite Fiber Brush Anodes for Increased Power Production in Air-Cathode Microbial Fuel Cells,” *Environ. Sci. Technol.*, vol. 41, no. 9, pp. 3341–3346, May 2007.

[18] Y. Zuo, S. Cheng, D. Call, and B. E. Logan, “Tubular Membrane Cathodes for Scalable Power Generation in Microbial Fuel Cells,” *Environ. Sci. Technol.*, vol. 41, no. 9, pp. 3347–3353, May 2007.

[19] B. Min and B. E. Logan, “Continuous Electricity Generation from Domestic Wastewater and Organic Substrates in a Flat Plate Microbial Fuel Cell,” *Environ. Sci. Technol.*, vol. 38, no. 21, pp. 5809–5814, Nov. 2004.

[20] L. J. Casarett, C. D. Klaassen, and J. B. Watkins, Eds., *Casarett and Doull’s essentials of toxicology*. New York: McGraw-Hill/Medical Pub. Div, 2003.

[21] P. Stoodley, K. Sauer, D. G. Davies, and J. W. Costerton, “Biofilms as Complex Differentiated Communities,” *Annu. Rev. Microbiol.*, vol. 56, no. 1, pp. 187–209, Oct. 2002.

[22] S. Debuy, “Développement de cathodes microbiennes catalysant la réduction du dioxygène,” Institut National Polytechnique de Toulouse, 2015.

[23] H. E. Jeong, I. Kim, P. Karam, H.-J. Choi, and P. Yang, “Bacterial Recognition of Silicon Nanowire Arrays,” *Nano Lett.*, vol. 13, no. 6, pp. 2864–2869, juin 2013.

[24] F. Qian, H. Wang, Y. Ling, G. Wang, M. P. Thelen, and Y. Li, “Photoenhanced Electrochemical Interaction between *Shewanella* and a Hematite Nanowire Photoanode,” *Nano Lett.*, vol. 14, no. 6, pp. 3688–3693, Jun. 2014.

[25] A. J. Bard, R. Parsons, J. Jordan, and International Union of Pure and Applied Chemistry, Eds., *Standard potentials in aqueous solution*, 1st ed. New York: M. Dekker, 1985.

[26] R. A. Sinton and A. Cuevas, “Contactless determination of current–voltage characteristics and minority-carrier lifetimes in semiconductors from quasi-steady-state photoconductance data,” *Appl. Phys. Lett.*, vol. 69, no. 17, p. 2510, 1996.

[27] M. R. Ramdani *et al.*, “Fast Growth Synthesis of GaAs Nanowires with Exceptional Length,” *Nano Lett.*, vol. 10, no. 5, pp. 1836–1841, avril 2010.

[28] E. Gil *et al.*, “Record Pure Zincblende Phase in GaAs Nanowires down to 5 nm in Radius,” *Nano Lett.*, vol. 14, no. 7, pp. 3938–3944, juillet 2014.

[29] E. Gil, Y. André, R. Cadoret, and A. Trassoudaine, “Hydride Vapor Phase Epitaxy for Current III–V and Nitride Semiconductor Compound Issues,” in *Handbook of Crystal Growth*, Elsevier, 2015, pp. 51–93.

[30] W. T. Hong, M. Risch, K. A. Stoerzinger, A. Grimaud, J. Suntivich, and Y. Shao-Horn, “Toward the rational design of non-precious transition metal oxides for oxygen electrocatalysis,” *Energy Env. Sci*, vol. 8, no. 5, pp. 1404–1427, 2015.

[31] A. lvarez-Lueje, M. Prez, and C. Zapat, “Electrochemical Methods for the In Vitro Assessment of Drug Metabolism,” in *Topics on Drug Metabolism*, J. Paxton, Ed. InTech, 2012.

[32] K. Rabaey, N. Boon, S. D. Siciliano, M. Verhaege, and W. Verstraete, “Biofuel Cells Select for Microbial Consortia That Self-Mediate Electron Transfer,” *Appl. Environ. Microbiol.*, vol. 70, no. 9, pp. 5373–5382, Sep. 2004.

[33] J. P. Busalmen, A. Esteve-Nuñez, and J. M. Feliu, “Whole Cell Electrochemistry of Electricity-Producing Microorganisms Evidence an Adaptation for Optimal Exocellular Electron Transport,” *Environ. Sci. Technol.*, vol. 42, no. 7, pp. 2445–2450, Apr. 2008.

[34] M. I. Montenegro, M. A. Queirós, and J. L. Daschbach, *Microelectrodes: Theory and Applications*. Dordrecht: Springer Netherlands, 1991.

[35] N. S. Ramaraja P Ramasamy, “Electrochemical Impedance Spectroscopy for Microbial Fuel Cell Characterization,” *J. Microb. Biochem. Technol.*, 2013.

[36] C. Gabrielli, “Méthodes électrochimiques: Mesures d’impédances,” *Tech. Ing. Corros. Vieil.*, no. P2210, 1998.

[37] J. S. Daniels and N. Pourmand, “Label-Free Impedance Biosensors: Opportunities and Challenges,” *Electroanalysis*, vol. 19, no. 12, pp. 1239–1257, Jun. 2007.

[38] A. Bonanni and M. del Valle, “Use of nanomaterials for impedimetric DNA sensors: A review,” *Anal. Chim. Acta*, vol. 678, no. 1, pp. 7–17, Sep. 2010.

[39] X. Luo and J. J. Davis, “Electrical biosensors and the label free detection of protein disease biomarkers,” *Chem. Soc. Rev.*, vol. 42, no. 13, p. 5944, 2013.

[40] E. Katz and I. Willner, “Probing Biomolecular Interactions at Conductive and Semiconductive Surfaces by Impedance Spectroscopy: Routes to Impedimetric Immunosensors, DNA-Sensors, and Enzyme Biosensors,” *Electroanalysis*, vol. 15, no. 11, pp. 913–947, Jul. 2003.

[41] H. Cai, Y. Xu, N. Zhu, P. He, and Y. Fang, “An electrochemical DNA hybridization detection assay based on a silver nanoparticle label,” *The Analyst*, vol. 127, no. 6, pp. 803–808, May 2002.

[42] B. Ketterer, “Raman Spectroscopy of GaAs Nanowires: Doping Mechanisms and Fundamental Properties,” École Polytechnique Fédérale de Lausanne, 2011.

[43] F. Yang *et al.*, “Zn-doping of GaAs nanowires grown by Aerotaxy,” *J. Cryst. Growth*, Oct. 2014.

[44] J. Jadczak *et al.*, “Unintentional High-Density p-Type Modulation Doping of a GaAs/AlAs Core–Multishell Nanowire,” *Nano Lett.*, vol. 14, no. 5, pp. 2807–2814, mai 2014.

Conclusion

In recent years, GaAs nanowires and nanostructures, which exhibit high mobility and direct band gap, have attracted a great attention for future electronic, optoelectronic and energy devices. Silicon remains the dominant material for information and communication technologies due to its low cost and mature processing procedures. Today, intense research is made to integrate GaAs semiconductors with Si to enable novel functional devices that can take advantage of the benefits offered by both materials. In this context, this thesis was dedicated to the growth of GaAs nanowires and nanostructures by Hydride Vapor Phase Epitaxy (HVPE) on silicon substrates, in order to study the capability of the HVPE process to integrate III-V structures on the silicon platform.

First, we have demonstrated the growth of self- catalyzed GaAs nanowires by HVPE on un-patterned Si (111) substrates at a low temperature of 600 °C with extremely high $GaCl/AsH_3$ flow ratios. Such growth conditions enable to successfully overcome the main issues related to HVPE and MOVPE synthesis of gold-free GaAs nanowires: namely, the low decomposition efficiency of gallium precursors and effectively arsenic-rich atmosphere in the reactor. Nanowires 10 μm long were grown in 10 min-processes and were almost free of structural defects. The nanowires were found strongly tapered at the beginning but then became straight with minimum radius of only 5 nm. A model that explains well the experimental findings was developed. We speculate that the nanowire growth is catalyzed by the gallium droplets that nucleate on the SiO_2/Si (111) surface under appropriate conditions and then rapidly swell to the size of the order of 100 nm before the very first nanowire monolayer can form. This process defines the initial nanowire radius. When the gallium droplets are brought away from the substrate, surface diffusion of gallium is disabled and the droplets shrink under excessive arsenic influx. However, the Gibbs-Thomson curvature effect largely enhances the arsenic desorption from very small droplets. Thus, the nanowires acquire a stationary radius and continue growing straight.

Beside the nanowires, regular nanometer scale GaAs polyhedrons were found as by-products grown on the same substrate. These structures have attracted our attention because of their high density and well defined crystal facets. The feasibility of such structures opens the possibility to integrate GaAs nanocrystals on silicon. The initial nucleation of these structures is due to the presence of nano-holes in the SiO_2 generated by the chemical cleaning of the substrate. Wulff construction was built to model the crystallographic mechanism that governs the growth of this nano-polyhedrons. Finally, we have investigated the feasibility of hybrid HVPE/CBE or MOVPE processes. As a conclusion to the first part of my PhD, we gave the first demonstration of cost-effective gold-free HVPE-growth protocol for the synthesis of GaAs nanostructures and nanowires on silicon substrate. It may be useful for the further development of HVPE, hybrid HVPE/MBE or HVPE/MOVPE processes to fabricate GaAs-based photonic nanostructures on silicon.

In the second part of the PhD work, we have described the motivation of the use of GaAs nanowires for biology components. Thanks to a collaboration between several researchers from Institut Pascal with different skills in electronics, electrochemistry and biology, we built the first microbial fuel cell (MCF) prototype with GaAs substrate electrode. With a long duration measurement of several days inside a bacteria solution, we have obtained the preliminary results giving the numerical value of the electromotive force of the bacteria in contact with electrodes made of planar GaAs substrate. To address with more accuracy the behavior of the electron exchange between the bacteria and the GaAs electrode, a study based on electrochemistry ability was carried out. Cyclic voltammetry and EIS measurements-have been performed to establish the specific electrochemistry properties of several GaAs electrodes made of doped and undoped planar layers or nanowires. Preliminary HVPE n and p doping experiments were conducted in order to reinforce the future nanowires electrode conductivity.

The self-catalyzed HVPE growth of GaAs nanowires and nano-polyhedrons on silicon and their potential application in bioenergy were described in this thesis. In the future, the HVPE group of Institut Pascal will continue to develop the growth of GaAs nanowires on silicon substrates through metal catalyst and catalyst-free approaches in order to improve the density of the nanowires. The doping of GaAs nanowires will be also performed since, as it was demonstrated in this report, it will be crucial for the fabrication of the final MFC prototype which will work in real biological conditions.

Résumé en français

Synthèse de nanofils et de nanostructures de GaAs par épitaxie en phase vapeur par la méthode aux hydrures (HVPE) sur substrat silicium. Application des nanofils GaAs aux piles microbiennes.

La communauté scientifique exprime actuellement un fort intérêt pour les micro- et nanofils de semiconducteurs GaAs pour des applications de la spintronique, de la photonique quantique, de capteurs chimiques ou de piles à combustible biologique [1-4]. La valeur élevée du rapport surface/volume de ces objets ainsi que la sensibilité de leurs propriétés optiques ou de transport aux effets de surface, en font des candidats à fort potentiel. La synthèse de tels objets est effectuée par des méthodes de croissance où le matériau épitaxié est libéré des contraintes dues au substrat et peut être mis en œuvre sur des supports à très faible coût comme les substrats de silicium.

Deux méthodes de croissance ont été mises en œuvre durant ma thèse pour l'épitaxie des nanofils ou nano-objets par HVPE. La première est la croissance via un catalyseur métallique par la voie Vapeur-Liquide-Solide (VLS). Une particule métallique préalablement formée sur le substrat sert de catalyseur. La deuxième méthode est également basée sur un procédé VLS, mais via un catalyseur. Le catalyseur est l'élément III lui-même, le gallium dans le cas de la croissance de GaAs. Les deux méthodes de croissance sont les techniques les plus utilisées aujourd'hui pour synthétiser les fils et nanofils à base de semiconducteurs III-V par les procédés d'épitaxie les plus connus MBE (Molecular Beam Epitaxy) ou MOVPE (Organometallic Vapor Phase Epitaxy).

Le procédé HVPE, utilisé durant mes travaux de thèse, a été développé dans les années 1970 pour les premières croissances de couches planaires III-V [5-8]. Progressivement abandonné par les épitaxieurs, il a connu un regain d'intérêt vingt ans plus tard pour la synthèse de couches très épaisses de GaN à vocation de quasi-substrats. C'est une méthode de croissance proche de l'équilibre thermodynamique qui utilise des précurseurs chlorés, lui procurant une sélectivité intrinsèque parfaite, la croissance du cristal étant gouvernée par les cinétiques de surface. Aujourd'hui, l'Institut Pascal (IP) est le seul laboratoire au monde à développer la croissance de nanofils de GaAs par HVPE. Les premiers résultats, publiés précédemment par le groupe et très encourageants, avaient montré la capacité de ce procédé pour la synthèse par VLS de nanofils III-V ultra-longs, de qualité cristallographique excellente, et avec de très grandes vitesses de croissance axiale de plus de 120 $\mu m.h^{-1}$ [9].

Durant ma thèse, j'ai développé la croissance auto-catalysée de nanofils et des nanoobjets de GaAs par HVPE sur substrat silicium et initié la faisabilité d'utiliser un substrat constitué de nanofils de GaAs comme électrode dans une pile microbienne.

Ce manuscrit, qui s'organise en deux chapitres, décrit les principaux résultats obtenus.

Dans la première partie, qui a constitué l'une des mes principales missions durant ce doctorat, je présente la croissance auto-catalysée de nanofils de GaAs, sur substrat de silicium. A mon arrivée, le groupe HVPE de l'IP avait la maîtrise de la croissance sélective de GaAs (SAG-HVPE) [10-11] ainsi que la croissance de nanofils de GaAs par procédé VLS suite à un dépôt contrôlé de catalyseur or sur les substrats de GaAs. Cependant, la forte demande d'intégration de semi-conducteurs III-V sur la plate-forme de silicium par les industriels a initié plusieurs études de croissance de nanofils de GaAs [12-13]. A l'IP nous avons démarré la croissance auto-catalysée de nanofils de GaAs sur substrats silicium lors de ma thèse. Ainsi le chapitre1 de ce manuscrit décrit un état de l'art des différentes techniques de croissance utilisées pour les nanofils de GaAs sur substrat silicium. Une deuxième partie décrit la mise en œuvre du procédé HVPE via une étude thermodynamique afin de trouver les conditions favorables à la croissance de nanofils de GaAs sur substrat silicium. Ensuite, une partie consacrée à la modélisation théorique de la croissance des nanofils de GaAs est présentée. La dernière partie du chapitre est dédiée à la croissance de structures de GaAs de morphologie de polyèdres sur silicium par HVPE. Ces structures sont synthétisées simultanément que les fils de GaAs. Ce chapitre propose également le développement d'un procédé hybride MOVPE/HVPE. Des reprises de croissance ont été effectuées par procédé HVPE sur des structures MOVPE de GaAs synthétisés au LPN C2N Marcoussis (collaboration avec le Dr. Charles Renard) sur des substrats silicium.

Le deuxième chapitre est dédié au développement d'un prototype d'une pile à combustible microbienne (MFC) en utilisant comme anode un substrat de nanofils de GaAs. La fonctionnalité de ce prototype (MFC), qui utilise un micro-organisme actif en tant que biocatalyseur dans un compartiment d'anode anaérobie pour la production de bioélectricité, est discutée. Des mesures en électrochimie de voltampérométrie cyclique (CV) et de spectroscopie d'impédance électrochimique (EIC) ont été effectuées afin de mesurer avec précision la réponse de l'anode dans un milieu de PH contrôlé.

Chapitre 1: GaAs auto-catalysée nanofils sur silicium par HVPE

L'Epitaxie en phase vapeur (VPE) à base de précurseur gazeux chlorure a été développée dans les années 1960 pour la croissance de la première épi-couche de semiconducteurs III-V. La HVPE est un procédé où l'élément du groupe V est fourni directement par les hydrures AsH_3, PH_3, ou NH_3, en utilisant HCl gazeux pour fabriquer des éléments III.

La méthode aux hydrures a été abandonnée dans les années 80 au profit de la MOVPE et de la MBE qui ont été développées à l'échelle industrielle et se sont imposées pour la réalisation d'hétérostructures composants des III-V. Depuis les années 90, la HVPE connaît un regain d'intérêt grâce à la filière nitrure. Les fortes vitesses de croissance atteintes par le procédé HVPE (jusqu'à plusieurs centaines de µm/h) en ont fait un candidat idéal pour la fabrication de quasi-substrats de GaN. L'introduction d'étapes de croissance sélective dans la réalisation de structures III-N a également boosté la HVPE pendant quelques années (1990 à 2000). Aujourd'hui, l'Institut Pascal est le seul laboratoire universitaire français possédant deux réacteurs HVPE « home-made » dédiés à la croissance des semiconducteurs III-V et III-N.

Un schéma des bâtis HVPE de l'Institut Pascal est donné en Fig. 1. Réalisée entièrement en quartz, l'enceinte de réaction d'un réacteur HVPE est composée de trois parties : la première est appelée zone source, en référence à la source de gallium, qui permet la production de l'espèce GaCl, précurseur en élément III (gallium). Le flux vecteur composé d'azote N_2 ou/et 'hydrogène H_2 est aussi introduit en zone source. La deuxième est la zone de mélange où l'hydrure est introduit et où se produit le mélange des gaz précurseurs en éléments III et V. Ces deux premières zones sont isolées ou communiquent l'une avec l'autre par l'intermédiaire d'une vanne tiroir. Cela permet notamment de préparer et stabiliser le flux de l'espèce GaCl avant croissance sans que le substrat n'y soit exposé. La troisième et dernière partie est la zone de dépôt des gaz. C'est dans cette zone que le substrat est placé en vue de la croissance. Le flux total et la géométrie du réacteur sont ajustés afin d'assurer un mélange homogène en phase vapeur et un flux laminaire au-dessus de substrat [14].

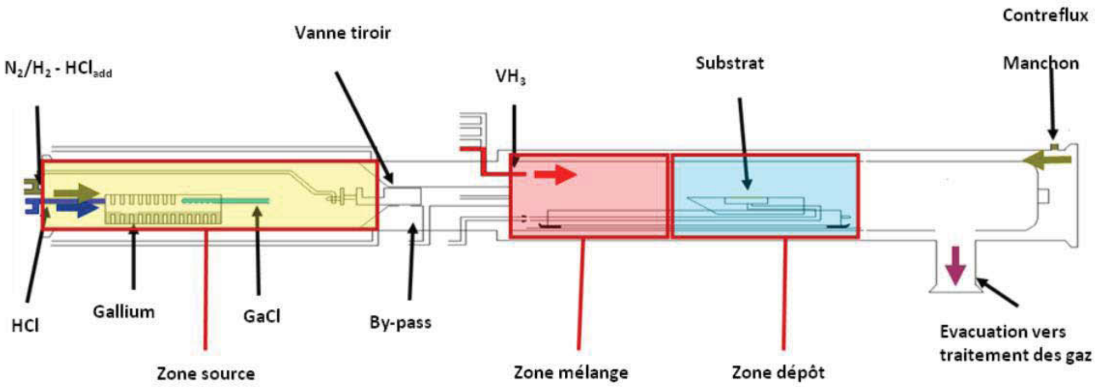

Fig.1. Schéma type d'un bâti HVPE de l'Institut Pascal pour la croissance des semiconducteurs III-V.

La croissance des semi-conducteurs III-V par HVPE implique des molécules GaCl gazeuses synthétisées à l'intérieur d'un réacteur à quartz dans zone source, en utilisant des flux HCl réagissant avec Ga liquide à haute température pour créer des chlorures comme GaCl. L'élément V est transporté sous forme d'arsine (AsH_3). Lors de l'entrée dans le réacteur à paroi chaude, ces hydrures se décomposent complètement en molécules $As_2 \leftrightharpoons As_4$ à la température de croissance et la pression atmosphérique [15-16]. La réaction de croissance globale de GaAs dans l'atmosphère H_2 peut être donnée comme suit :

$$GaCl_g + \frac{1}{4}As_{4g} + H_{2g} \leftrightharpoons GaAs + HCl_g + \frac{1}{2}H_{2g}$$

Dans le procédé HVPE, il n'y a pas de retard cinétique à l'évolution de la réaction, qui peut avoir lieu dans le sens du dépôt sur le substrat, comme dans le sens d'une attaque de la surface du substrat par variation de la composition de la phase vapeur [17-18]. Le paramètre de sursaturation γ de la phase vapeur définit l'état d'avancement de la réaction de dépôt par rapport à l'équilibre à la température T. Cet équilibre thermodynamique est caractérisé par une constante d'équilibre $K_i^{eq}(T)$.

La sursaturation est exprimée à partir des pressions partielles des éléments gazeux participant à la croissance :

$$K_i^{eq}(T) = \exp\left(\frac{-\Delta G(T)}{kT}\right) = \left(\frac{a_{HCl_g} a_{GaAs}}{a_{GaCl_g} a_{As_{4g}}^{1/4} a_{H_{2g}}^{1/2}}\right)_{eq} = \frac{[HCl]_{eq}}{[GaCl]_{eq}[As_4]_{eq}^{1/4}[H_2]_{eq}^{1/2}}$$

Et

$$\gamma + 1 = \frac{[HCl]K_{eq}(T)}{[GaCl][As_4]^{1/4}[H_2]^{1/2}}$$

Où $\Delta G(T)$ représente la variation de l'enthalpie libre de la réaction à la température de croissance T, calculée à partir des tables de données thermodynamiques relatives aux espèces impliquées dans la réaction.

$\gamma = 0$ correspond à l'équilibre de la réaction,

$\gamma > 0$ correspond à un dépôt forcé,

$\gamma < 0$ correspond à une attaque forcée.

Les pressions partielles des espèces gazeuses sont déterminées à partir de la résolution d'un système d'équations des constantes d'équilibre, de conservation de la matière et de pression totale (1 atmosphère). D'un point de vue statistique, les constantes d'équilibre $K_i^{eq}(T)$de la réaction de dépôt considérée à l'équilibre peuvent s'exprimer à partir des fonctions de partition sous la forme ci-dessous :

$$K_i^{eq}(T) = \frac{z_{D_S} z_{C_g}}{z_{A_g} z_{B_g}}$$

Chaque fonction gazeuse de partition est le produit des fonctions de partition de translation, de rotation et de vibration de l'espèce considérée. La fonction de partition des espèces en surface ou des espèces cristallines est celle de vibration.

La thermodynamique macroscopique permet d'identifier les espèces chimiques en présence et de déterminer le sens d'évolution de la réaction. La thermodynamique statistique permet de modéliser les cinétiques des processus mis en jeu qui gouvernent la croissance épitaxiale. Ces cinétiques de surface incluent les cinétiques d'adsorption et de désorption des espèces gazeuses sur la surface, les cinétiques de décomposition des ad-molécules et les cinétiques de diffusion des ad-atomes ou ad-molécules jusqu'aux sites cristallins [19-10].

La méthode de croissance VLS permet une conception ascendante sophistiquée de la morphologie et de la structure cristalline influençant les propriétés résultantes des nanofils. Des gouttelettes d'or ont été utilisées comme catalyseur pour initier la croissance III-V nanofils par MOVPE. Et fonctionnent également bien dans HVPE comme cela a été démontré par l'IP en 2010. Cependant, l'or peut contaminer les nanofils et n'est pas bien adapté pour l'intégration avec les plateformes électroniques au silicium. Par conséquent, des efforts considérables ont été consentis pour développer des techniques de croissance exemptes d'or lorsque le procédé VLS est catalysé par des métaux du groupe III plutôt que par de l'or. C'est dans ce contexte que j'ai mené les travaux présentés dans ce premier chapitre. Je propose ci-dessous un bref état de l'art des principaux résultats obtenus par les procédés MBE et MOVPE pour la croissance auto-catalysée en gallium.

La croissance de nanofils par VLS gallium catalysée en MBE a été introduite par A. Fontcuberta i Morral et al. [20-21] Nanofils de GaAs ont été obtenus sur wafer GaAs (111) B et (001) recouverte de SiO_2 d'une épaisseur de 6 nm.. Les principaux paramètres régissant la croissance de nanofils par procédé MBE sont exposés : la couche d'oxyde fournit des sites de nucléation ; offre également des caractéristiques de mouillage favorisant la formation de gouttelettes Ga ; un taux de croissance axiale limité par l'arsenic (contrôlé par la pression d'As_4) et enfin les adatomes de Ga dans gouttelettes Ga accélère la vitesse de croissance.

Les premiers travaux de modélisation de ce régime de croissance ont été proposés par le professeur V.G. Dubrovskii et al. [22] Ils proposent un modèle prédisant le nouveau mode VLS avec l'extension latérale de certains de nos nanofils vers leurs sommets, induite par la nucléation de paroi latérale à partir des gouttelettes entourant les nanofils. Des travaux plus récents de ce même groupe [20-21] proposent un modèle théorique pour la thermodynamique qui régit la croissance des nanofils et l'énergie de surface [23-26]. Alors que la croissance VLS catalysée par l'indium des nanofils InAs et des hétérostructures de nanofils à base d'InAs a été démontrée avec succès par MBE [27-28] et MOVPE [29-30], la croissance de MOVPE catalysée par le gallium pour les nanofils de GaAs reste une tâche très difficile et ne produit pas de structures ayant une morphologies et une qualité cristalline satisfaisantes et comparables à celles obtenues par MBE. Les limitations technologiques sont dues aux températures élevées (au moins supérieures à 600 °C) requises pour le craquage de précurseurs de gallium organométallique et combinées à une atmosphère riche en arsenic dans le réacteur MOVPE. De telles conditions ne favorisent pas la nucléation initiale et la stabilité supplémentaire des gouttelettes de gallium liquide [31-32]. Compte tenu de ces limitations, il est extrêmement difficile de trouver des conditions appropriées en MOVPE pour la croissance en régime VLS catalysée au gallium et les nanofils de GaAs obtenus jusqu'à présent sont limités en longueur (typiquement moins de 1 µm) [33].

La plage de température les plus favorable à la croissance auto-catalysée Ga et reportés par les procédé MBE et MOVPE se situe entre 550 °C à 620 °C. Ces températures sont nécessaires pour stabiliser des gouttelettes de gallium à la surface de Si [25-26][34-37]. Cependant, il existe une différence notable entre le procédé HVPE et le procédé MOVPE qui réside dans la nature de l'élément III. La HVPE utilise des molécules de GaCl synthétisées à l'intérieur du réacteur dans la zone en amont du substrat à haute température (T> 700 °C). La décomposition du GaCl est beaucoup plus difficile entre 600 °C et 700 °C. Dans ce manuscrit des calculs thermodynamiques des constantes d'équilibre de formation du gallium liquide sont donnés et analysés. Le protocole expérimental mis au point pour la croissance de fils de GaAs nécessite une étape de nettoyage chimique des substrats. Des substrats de Si (111) non patternés ont été nettoyés chimiquement en utilisant de l'acide fluorhydrique (HF) à 1% pendant 7 minutes afin d'éliminer partiellement la couche de SiO_2 native et de favoriser la présence de sites de nucléation pour les gouttelettes de gallium. Les substrats ont ensuite été immédiatement introduits dans le réacteur HVPE à température ambiante. La croissance de GaAs a été effectuée à 600 °C à pression atmosphérique avec le gaz H_2 comme gaz vecteur. La pression partielle de AsH_3 a été délibérément fixée à des valeurs très faibles entre 1,5 et 30 Pa, tandis que la pression partielle de GaCl se situait entre de 265 et 660 Pa. Les rapports de flux atomiques III/V obtenus sont de 11 à 222, bien plus élevés que les rapports utilisés dans procédés MBE et MOVPE. Ce travail expérimental a été couplé à un travail de modélisation théorique effectué par le Professeur V.G. Dubrovskii (Academy of Science et IOFFE Saint Patersbourg). Ce modèle basé sur la croissance catalysée de nanofils par les gouttelettes de gallium présentes sur la surface SiO_2 / Si (111) dans des conditions appropriées et détaillées dans le chapitre 1 du manuscrit a permis d'identifier l'origine du mécanisme de croissance.

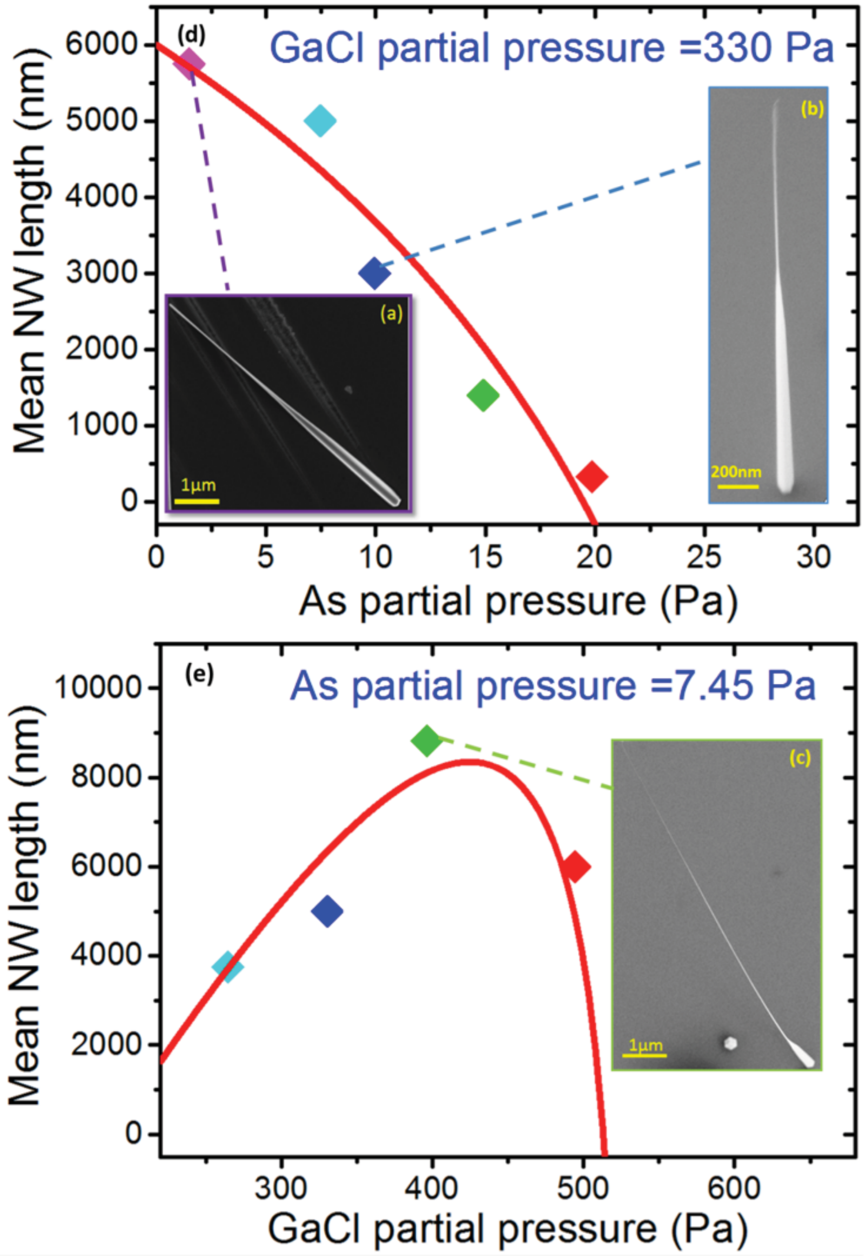

Fig.2: Images SEM des nanofils GaAs synthétisés à 600 ° C et 10 min de temps de croissance à III / V = 222 (a), III / V = 33 (b), III / V = 55 (c). On peut voir une cristallite de GaAs (c). Les valeurs expérimentales sont représentées par des losanges et les fits théoriques par les courbes (d) Evolution de la longueur moyenne des nanofils en fonction de la variation de la pression partielle d'As pour une pression partielle de GaCl fixée à 330 Pa. (e) Evolution de la longueur moyenne des nanofils en fonction de la variation de la pression partielle GaCl pour une pression partielle d'AsH_3 fixée à 7,45 Pa

Les Fig.2 (a) et (b) montrent les images de microscopie électronique à balayage (SEM) de nanofils GaAs obtenus avec un rapport atomique III/V de 44 et 22 après 10 min de croissance. Des études de post-croissance révèlent la présence de nanofils de GaAs avec des cristallites de GaAs de tailles différentes (Fig.2 (c)). Tous les nanofils sont orientés le long de la direction [111]. Les nanofils ont des longueurs différentes sur un même échantillon. Par exemple, pour des pressions partielles d'AsH_3 de 7,45 Pa et de GaCl de 330 Pa. La vitesse de croissance moyenne (c'est-à-dire la longueur moyenne des nanofils divisée par le temps de croissance total de 10 min) est estimée à 30 µm/h pour les nanofils de longueur de 5 µm (Fig.2 (a)) et 60 µm/h pour les nanofils les plus longs (Fig.2 (c)).

La Fig.2 (d) montre la variation de la longueur moyenne des nanofils en fonction de la pression partielle AsH_3 à une température de croissance fixe de 600 °C et de la pression partielle GaCl fixée de 330 Pa. Cette longueur diminue progressivement avec l'augmentation de AsH_3, à AsH_3 = 1,5 Pa à seulement 330 nm à AsH_3 = 20 Pa. Une augmentation supplémentaire d'AsH_3 à 30 Pa conduit à la suppression de toute croissance de nanofils.

Ce comportement est très inhabituel car, dans le cas de la MBE, il a été démontré que la vitesse de croissance des nanofils axiaux augmente presque linéairement avec le flux d'arsenic. De plus, dans le cas du MBE, la vitesse de croissance des nanofils axiaux n'est pas influencée par le flux de gallium qui ne modifie que la taille des gouttelettes [21][24][38-39].

Les images de microscopie électronique à transmission haute résolution (HRTEM) de nanofils GaAs typiques épitaxiés par HVPE puis séparés mécaniquement du substrat sont données en Fig.3.

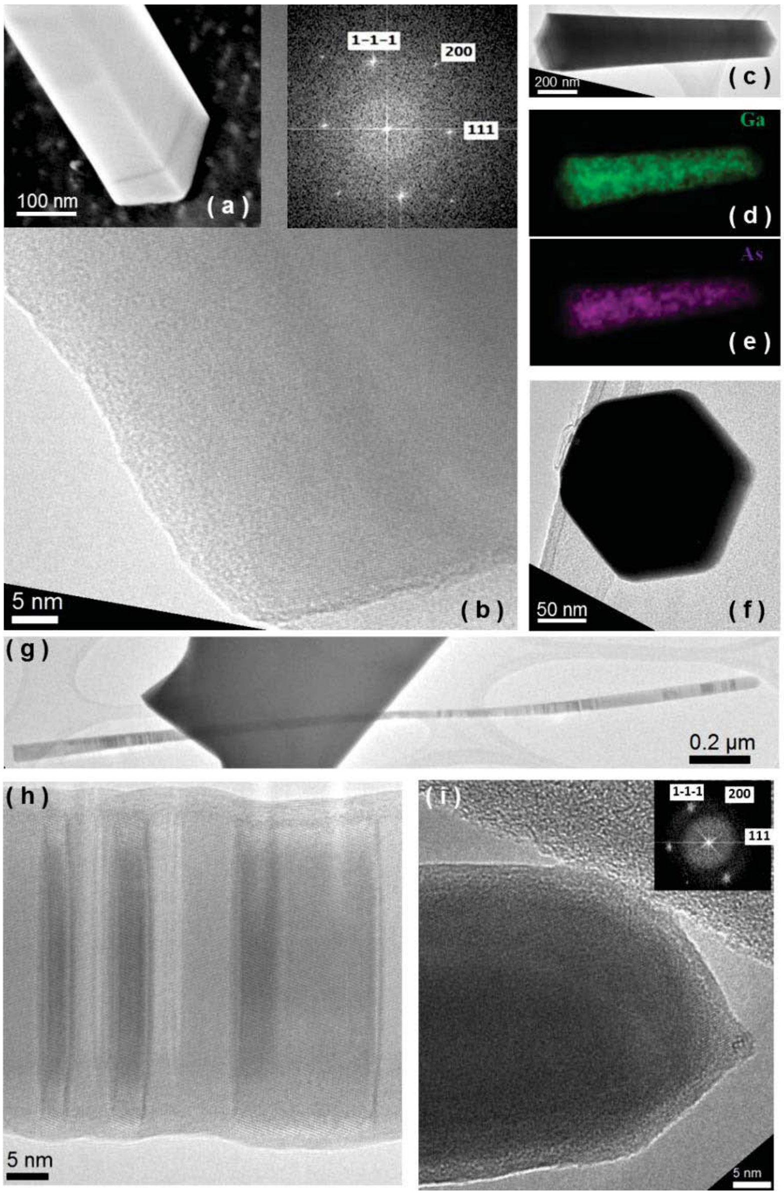

Fig 3. (a) Image effectuée à l'interface entre le nanofil GaAs et le substrat de Si (111) ; (c) image TEM d'un nanofil de GaAs épais (dimension de base = 300 nm); (b) image HRTEM correspondante à la partie inférieure du nanofil; La FFT en insert révèle la structure zincblende sans défauts;(d-e) cartographies EDX de gallium et d'arsenic; (f) image TEM d'une vue de nanofils le long de l'axe de croissance mettant en évidence la forme hexagonale de la base;(g) image TEM d'un nanofil GaAs de 2,4 μm de longueur;(h) Fautes de type twins dans la structure cubique dans la partie centrale du nanofil présentée en (g); (i) structure zinc blende pure au sommet du nanofil.

En conclusion, nous avons démontré pour la première fois la faisabilité de la croissance des nanofils GaAs par HVPE auto-catalysée Ga sur des substrats de Si (111) non patternés à basse température de 600 °C et avec des rapports de débit GaCl / AsH_3

très élevés. Un modèle qui explique bien les résultats expérimentaux a été développé. En particulier, nous supposons que la croissance des nanofils est catalysée par les gouttelettes de gallium qui nucléent sur la surface de SiO_2/Si (111) dans les conditions appropriées et ensuite gonflent rapidement à la taille de l'ordre de 100 nm avant que la première monocouche de nanofil ne puisse se former. Ce processus définit le rayon initial des nanofils. Ensuite, la diffusion de surface du gallium est désactivée et les gouttelettes rétrécissent sous un influx d'arsenic excessif. Cependant, l'effet de courbure de Gibbs-Thomson améliore largement la désorption de l'arsenic à partir de très petites gouttelettes. En conséquence, les nanofils acquièrent un rayon stationnaire et continuent de croître droit. Dans l'ensemble, nos résultats donnent la première démonstration d'un protocole de croissance sans catalyseur or, qui s'avère économique pour obtenir des nanofils de GaAs par épitaxie en phase vapeur. Il peut être utile pour le développement ultérieur de HVPE, MOVPE et HVPE/MOVPE hybride dédiés à la fabrication de nanostructures photoniques à base de GaAs sur silicium [40].

Le nanofil n'est pas la seule structure de GaAs développée sur le substrat de silicium. On a observé également la présence de nanostructures de géométrie polyèdre de GaAs. Avec une densité élevée et des facettes cristallines parfaitement définies. Nous avons observé la formation de ces polyèdres GaAs pour toutes les conditions expérimentales indiquées dans le chapitre 1 pour la température de croissance à 600 °C.

Les résultats post-croissance sont représentés en Fig. 4.

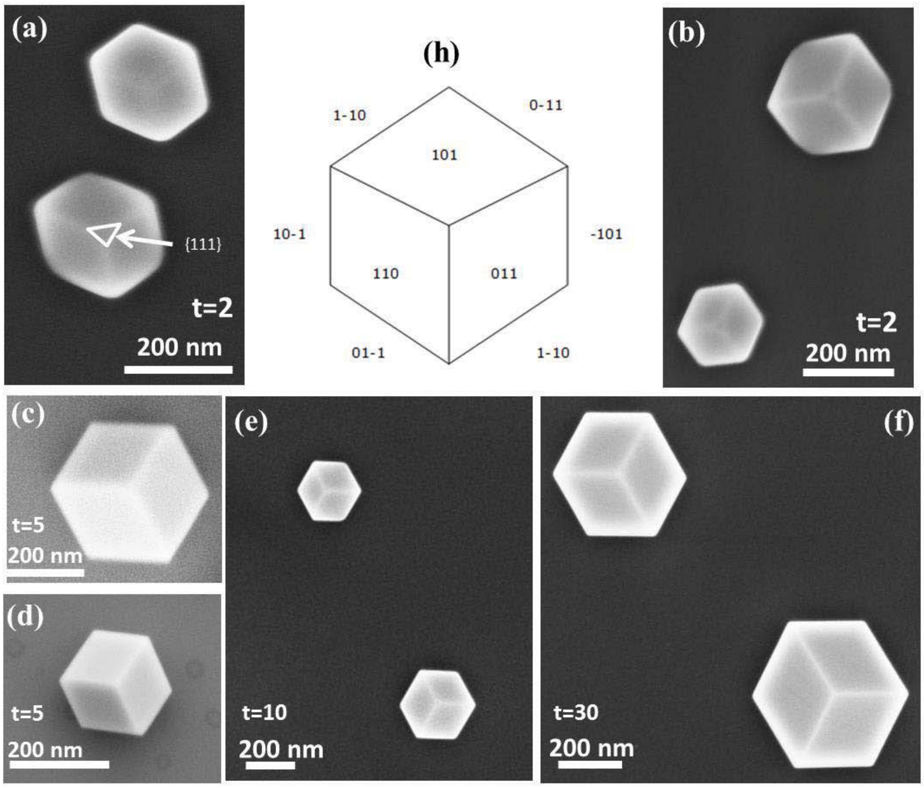

Fig. 4: SEM vue de dessus des GaAs nano polyèdres synthétisés par HVPE sur Si (111), t est la durée de croissance en minute. Le rapport III/V est le rapport atomique. (a) III / V = 37, t = 2 min. (b) III / V = 53 t = 2 min. (c) et (d) III / V = 44, t = 5 min. (e) III / V = 44, t = 10 min. (f) III / V = 44, t = 30 min. (h) schéma illustrant les facettes cristallines du nano polyèdre de GaAs et les 9 facettes de la famille {110}.

La Fig. 4 montre l'influence du rapport III/V et de la durée de croissance sur la formation du polyèdre GaAs par HVPE sur Si (111). La même morphologie de post-croissance et l'orientation de la facette ont été obtenues en changeant le rapport III/V de 37 en Fig. 5 (a) à 53 en Fig. 5 (b), même à 222. Tous les nano polyèdres sont délimités par les facettes {110}. Les facettes {111} au sommet indiquent que la croissance des structures inachevées en raison de la concurrence des deux vitesses des facettes {111} et {110} de GaAs. Cependant, pour un temps de croissance supérieure à 5 min, toutes les facettes {111} disparaissent.

Une simulation graphique basée sur une construction Wulff simple par WinXMorph [41] est effectuée afin de comprendre l'origine de la formation des 9 facettes {110}. Des travaux antérieurs montrent les vitesses de croissance des facettes GaAs {100}, {110} et {111} à 730 °C avec un rapport III/V =égal à 9 sont anisotropes. Ces vitesses ont été mesurées grâce à des épitaxies sur des couches planaires de substrats GaAs (100), (110) et (111). Pour les simulations présentées en figure 5, les vitesses de de croissance ont été calibrées à partir d'expériences de croissance effectuées à 714 °C avec un rapport III/V égal à 1, où 46,38 $\mu m.h^{-1}$ pour la direction [100] 24,52 $\mu m.h^{-1}$ pour la direction [111] ; 17,66 $\mu m.h^{-1}$ pour [110]. Par conséquent, les rapports des vitesses de croissance à 600 °C pour ces trois directions peuvent être exprimés comme suit : $R_{[110]}: R_{[111]}: R_{[100]} = 1: 1.4: 2.6$. Les résultats de la simulation sont représentés en Fig. 5.

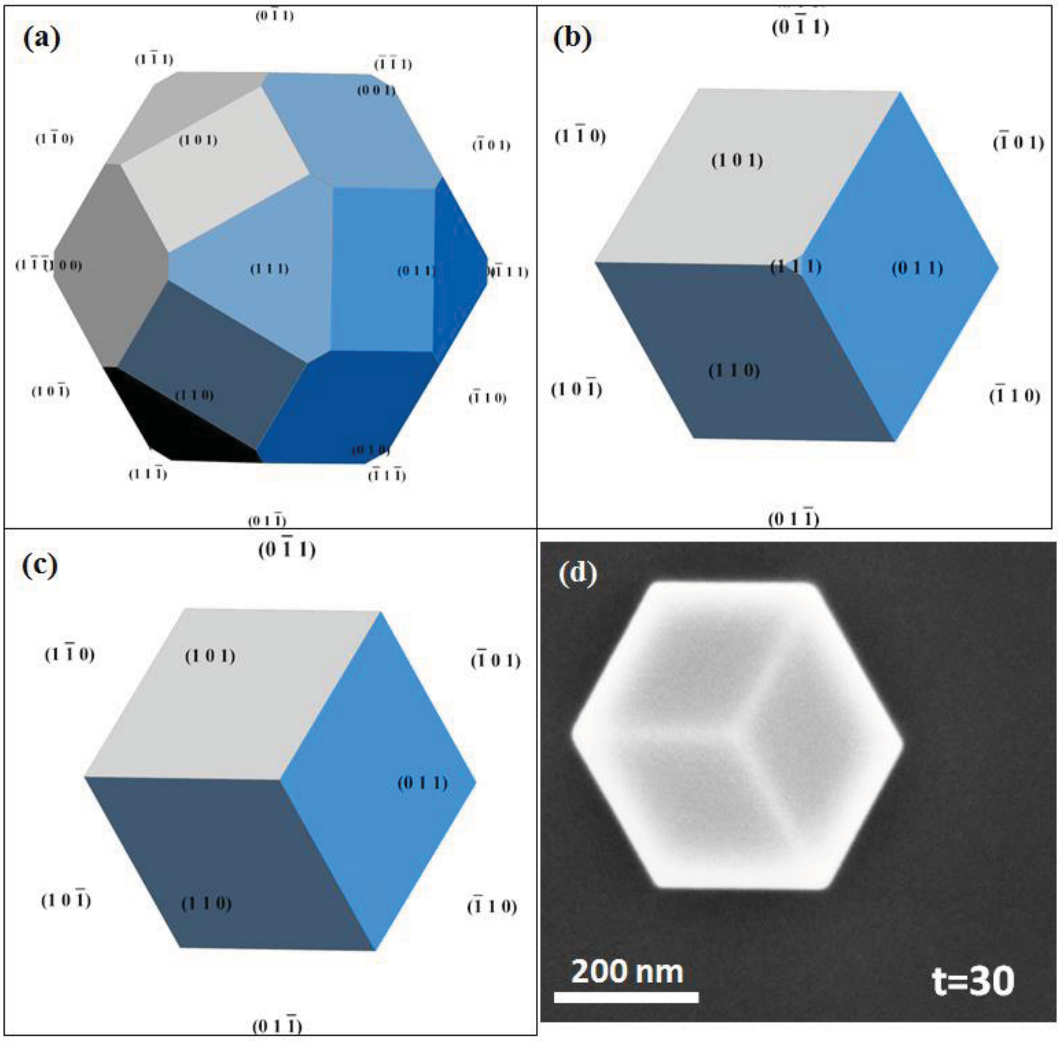

Fig. 5. Projection de Wulff par WinXMorph en direction (111) de la (a)-(c) et (d) image SEM des HVPE GaAs polyèdres. Simulation obtenue par la croissance isotrope selon les rapports de vitesse (a) $R_{[110]}: R_{[111]}: R_{[100]} = 1: 1: 1$, (b) $R_{[110]}: R_{[111]}: R_{[100]} = 1: 1.2: 2.6$, et (c) $R_{[110]}: R_{[111]}: R_{[100]} = 1: 1.4: 2.6$ avec facette {111} disparu, (d) condition de croissance anisotrope réelle à III/V = 44, t = 30 min.

La formation de ces nanopolyèdres démontre le potentiel de la HVPE pour l'intégration de GaAs sur substrat silicium en un seul procédé de croissance.

Dans la chapitre 1, nous nous sommées intéressés au développement de procédés de croissance hybrides HVPE/ MOVPE et HVPE/ CBE (Molecular Beam

Epitaxy). Une première étude de reprise de croissance HVPE sur les cristaux nanométriques de GaAs synthétisés par CBE sur substrat Si (111) a été réalisée (Fig. 6).

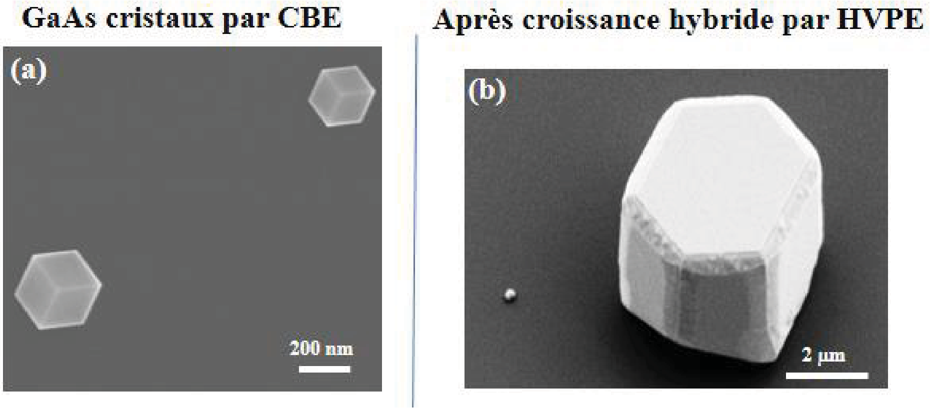

Fig. 6: Images SEM des cristaux de GaAs CBE (a) et leur reprise de croissance HVPE (b) sur substrat Si (111).

Chapitre 2: Mise au point d'un prototype de piles à combustible microbiennes (MFC) à base de nanofils de GaAs

Ce travail a été réalisé dans le cadre du projet LABEX IMOBS3 (Innovative Mobility Smart and Sustainable Solutions) sous le thème 3 consacré au processus de production et de mobilité énergétique. Les travaux présentés dans ce chapitre sont le résultat d'une collaboration étroite entre plusieurs chercheurs de l'Institut Pascal, avec le Dr P. Fontanille et le Dr F. Audonnet de l'axe GePEB (Génie des Procédés, Energétique et Biosystèmes), et le Dr C. Varenne de l'axe Photon. Ces résultats ont permis de concevoir et de tester un prototype de pile à combustible microbienne (MFC) à base d'échantillons de nanofils. Ce chapitre du manuscrit décrit dans une première partie le principe de fonctionnement d'une, pile à combustible microbienne (MFC) qui utilise un microorganisme actif comme biocatalyseur dans un compartiment anodique anaérobie pour la production de bioélectricité [42].

La deuxième partie est consacrée à des caractérisations électrochimiques basées sur la mesure du potentiel de Nernst d'une couche de GaAs en contact avec un milieu biologique. Ces mesures ont permis de valider la présence d'un échange d'électrons entre le biofilm de la bactérie (*Algoriphagus yeomjeoni*) et une anode composée d'une couche de GaAs dopée à 2.0×10^{18} cm^{-3}. Ces mesures ont ensuite été réalisées sur différentes anodes synthétisées par HVPE soit sous forme de couches planaires de GaAs soit sous forme de nanofils de GaAs. Une solution électrochimique étalon contenant des ions (Fe^{3+}/Fe^{+2}) et à pH contrôlée a été utilisée afin d'identifier les réactions d'oxydo-réduction qui se produisent à la surface du semiconducteurs GaAs. Enfin une dernière partie est dédiée à des mesures par spectroscopie d'impédance pour modéliser l'interface d'échange d'électrons à la surface des substrats (couche planaire de GaAs ou nanofils de GaAs) en milieu aqueux.

En général, les MFC sont des dispositifs qui utilisent des bactéries comme catalyseurs pour oxyder des matières organiques et inorganiques et générer du courant. Un schéma de principe d'une MFC est présenté en Fig. 7

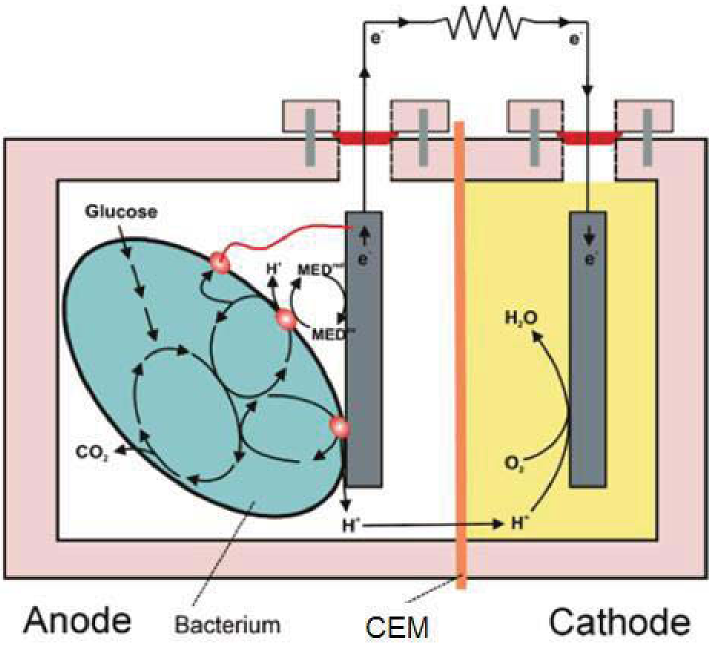

Figue. 7 : Principes de fonctionnement d'un MFC. Une bactérie dans le compartiment anodique transfère des électrons obtenus à partir d'un donneur d'électrons (glucose) vers l'électrode anodique. Ceci se produit soit par contact direct, soit via des nanofils, ou par navettes mobiles d'électrons (petites sphères représentent la navette associée à la membrane finale). Pendant la production d'électrons, les protons sont également produits en excès. Ces protons migrent à travers la membrane d'échange de cations (CEM) dans la chambre de la cathode. Les électrons diffusent de l'anode par une résistance externe (ou charge) vers la cathode où ils réagissent avec l'accepteur final d'électrons (oxygène) et les protons [43].

Notre premier prototype MFC a été conçu de manière très simplifiée. Recouvert par un coffret biologique et aseptisé. L'installation MFC contient comme suit : a) une couche planaire de GaAs (100) comme électrode d'anode ; b) l'électrode de calomel saturée comme électrode de référence ; c) une solution de bactéries (*Algoriphagus yeomjeoni*) comme source de réaction ; d) un bain-marie pour maintenir le système entier à 30 °C.

Il y a un signal très faible de cathode détecté dans ce système et on peut considérer que ce prototype a une cathode de type mélange air-liquide. Cela présente un rendement très limité par surface de contact entre le semiconducteur et le biofilm. L'interface air-liquide (solution de bactéries) fournit l'oxygène dissous à l'électrode, et le substrat de GaAs (100) comporte a une partie dans l'air qui joue un rôle de cathode d'air. Avec un potentiomètre numérique, nous avons mesuré la tension de ce circuit ouvert est à $185\ mV$. Ce qui est cohérent avec les calculs théoriques présentés dans le rapport.

Cependant, la pollution de la solution microbienne reste un facteur influent important pour la mesure du potentiel électrique. Et il s'agit d'un défaut intrinsèque lié à la conception du prototype MFC. Il sera corrigé en utilisant le récipient scellé pour empêcher la contamination de l'air à l'avenir. Pour mieux comprendre la fonctionnalité de l'électrode GaAs en milieu aqueux, nous avons réalisé une série d'analyses électrochimiques avec différents types d'électrodes GaAs.

Pour tester des propriétés plus spécifiques d'anodes différentes, cinq échantillons de GaAs (sur la figure 8, y compris l'électrode dopante précédemment) ont été préparés pour tester leur compatibilité électrochimique et la faisabilité d'effectuer des mesures en milieu aqueux.

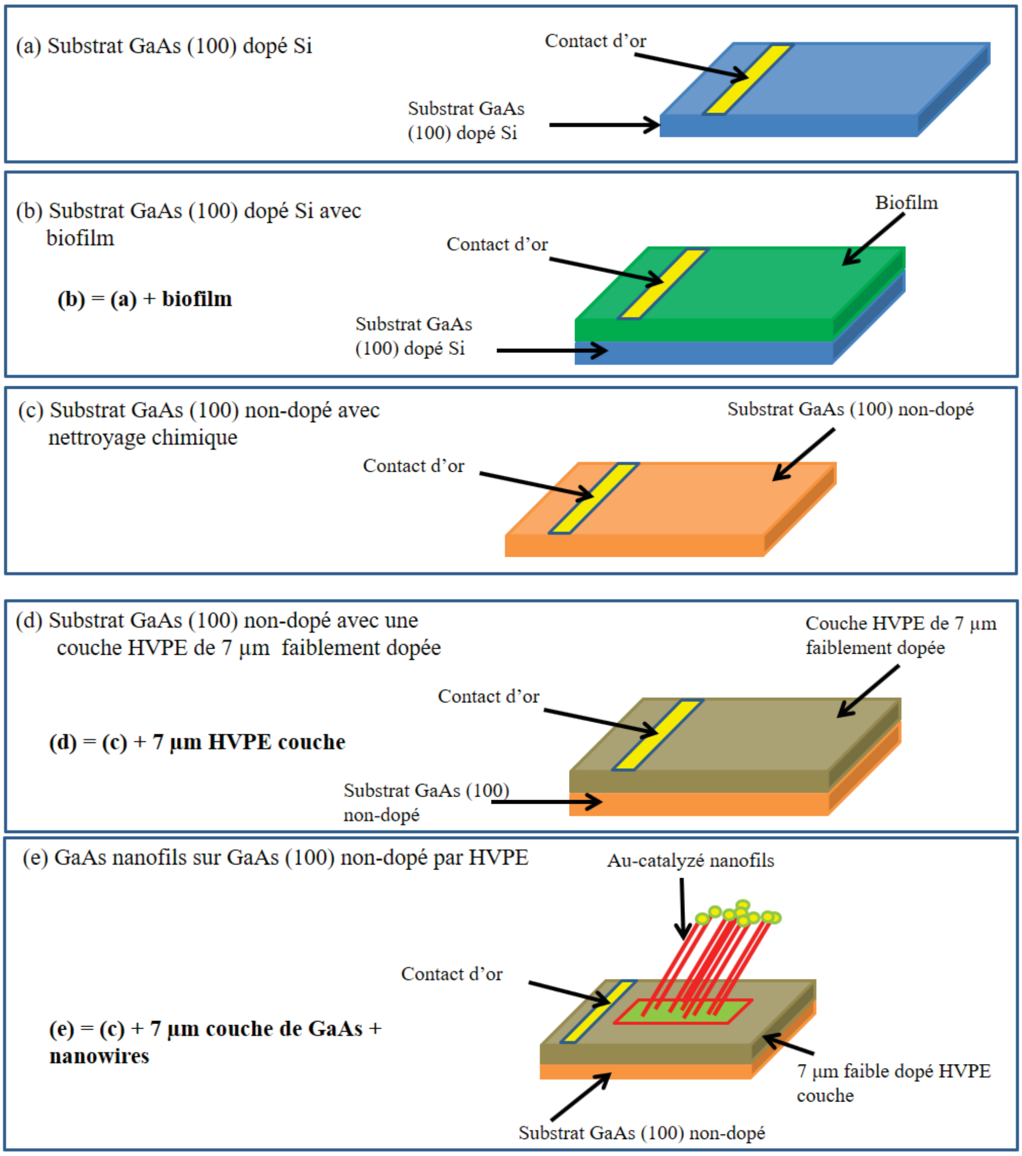

Figue. 8: Résume des cinq électrodes GaAs testées pour leur compatibilité électrochimique.

Deux mesures d'électrochimie ont été effectuées ici. Le premier est appelé voltampérométrie cyclique (CV). Le test CV est une méthode électro-analytique largement utilisée pour les espèces électro-actives. Il est connu comme méthode potentiellement contrôlée ou méthode de balayage potentiel. Le test CV nous aidera à étudier et à caractériser les interactions de transfert d'électrons entre microorganismes ou biofilms microbiens et anodes MFC [44-45]. Le test CV expose la cinétique de transfert d'électrons, les réactions redox et les propriétés des électrodes pendant le potentiel de rampe sur l'électrode de travail.

Nous appliquerons ensuite la seconde technique, appelée spectroscopie d'impédance électrochimique, basée sur la voltampérométrie cyclique, où un potentiel sinusoïdal est appliqué à différentes fréquences autour de certains points d'équilibre que nous avons choisis à partir de la courbe CV. La spectroscopie d'impédance électrochimique (EIC) est une technique efficace, non intrusive et semi-quantitative pour caractériser les performances des systèmes bio-électrochimiques tels que les piles à combustible microbiennes. La contribution de la spectroscopie d'impédance est très significative et appréciable surtout dans un système très hétérogène tel que les MFC. L'interface électrochimique du MFC est très complexe car les microbes colonisent l'électrode, ou des combinaisons de matériaux différents, conduisant à des réactions électrochimiques complexes. La spectroscopie d'impédance électrochimique (EIS) permet d'étudier la dynamique des charges mobiles de ce système [46]. Pour être analysée et corrélée aux propriétés physiques, la réponse d'impédance mesurée est simulée dans un circuit électronique équivalent. L'analyse EIS permet de décrire l'interface de l'anode, sa structure et les réactions qui s'y déroulent [47].

On peut résumer dans figure 9 que les circuits équivalents et des paramètres importants pour les cinq électrodes GaAs.

On peut conclure de la figure 9 que le niveau de dopage influe significativement sur la résistivité de la polarisation. Comme le montrent les électrodes (a) (d) et (c), le dopant en (a) et (d) ramène *Rp* dix mille fois par rapport à (c). La seconde conclusion que l'on peut livrer est l'influence de l'état de surface : la résistivité de la solution varie significativement avec la morphologie de la couche diffusion sur l'électrode de travail. Cette propriété peut être vue en comparant l'électrode (a) et (b), (c) et (d), ou (d) et (e). Une autre conclusion est que les nanofils GaAs de HVPE ajoutent plus de passages de diffusion pour des ions d'électrolyte. Ceci pourrait augmenter l'efficacité de la diffusion ionique sur l'électrode de travail. En résumant ces trois points ci-dessus, le dopage des nanofils devrait améliorer la réactivité/efficacité de l'électrode (e).

Electrodes GaAs	Circuits equivalent	$Rs, Rp\ et\ \alpha - CPE$
(a) 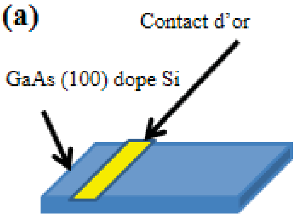	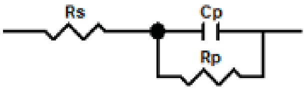	$Rs = 0\ \Omega.cm^{-1}$, $Rp = 310\ \Omega.cm^{-1}$, $\alpha - CPE = 1$
(b) 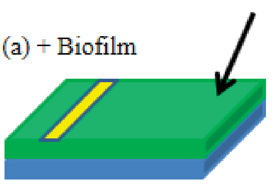	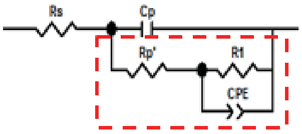	$Rs = 550\ \Omega.cm^{-1}$, $Rp = 3167\ \Omega.cm^{-1}$, $\alpha - CPE = 0.800$
(c) 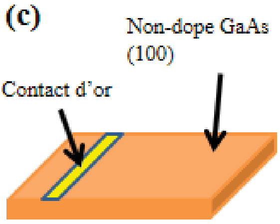	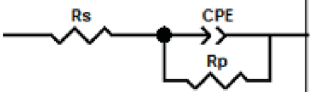	$Rs = 0\ \Omega.cm^{-1}$, $Rp = 9E6\ \Omega.cm^{-1}$, $\alpha - CPE = 0.801$
(d) 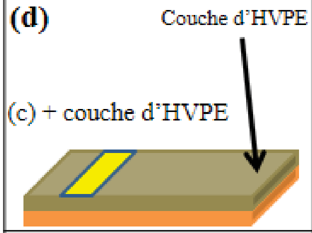	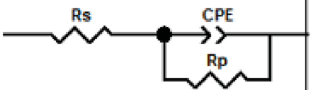	$Rs = 521\ \Omega.cm^{-1}$, $Rp = 577\ \Omega.cm^{-1}$, $\alpha - CPE = 0.786$
(e) 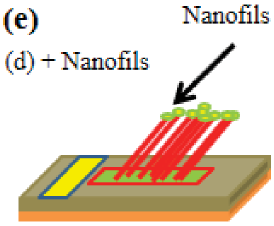	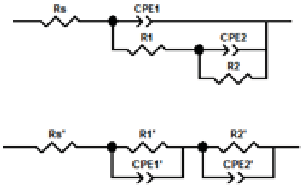	$Rs = 496\ \Omega.cm^{-1}$, $Rp1 = 668\ \Omega.cm^{-1}$, $\alpha - CPE1 = 0.901$, $Rp2 = 313\ \Omega.cm^{-1}$, $\alpha - CPE2 = 0.900$

Fig. 9 : Résumé des structures d'électrodes, des circuits équivalents et des résultats d'ajustage. Pour l'électrode (e), les résultats de montage de $Rp1/CPE1$ représentent les nanofils et $Rp2/CPE2$ pour la couche.

[1] K. L. Schulte *et al.*, "Metalorganic vapor phase growth of quantum well structures on thick metamorphic buffer layers grown by hydride vapor phase epitaxy," *J. Cryst. Growth*, vol. 370, pp. 293–298, May 2013.

[2] T. Earles *et al.*, "Low-strain, quantum-cascade-laser active regions grown on metamorphic buffer layers for emission in the 3.0–4.0 µm wavelength region," *IET Optoelectron.*, vol. 8, no. 2, pp. 25–32, Apr. 2014.

[3] J. Simon, D. Young, and A. Ptak, "Low-cost $III_{x/}V$ solar cells grown by hydride vapor-phase epitaxy," 2014, pp. 0538–0541.

[4] S. Lourdudoss, "Heteroepitaxy and selective area heteroepitaxy for silicon photonics," *Curr. Opin. Solid State Mater. Sci.*, vol. 16, no. 2, pp. 91–99, Apr. 2012.

[5] M. Takikawa, "Two-dimensional electron gas in a selectively doped InP/In0.53 Ga0.47As heterostructure grown by chloride transport vapor phase epitaxy," *Appl. Phys. Lett.*, vol. 43, no. 3, p. 280, 1983.

[6] C. Guedon, J. Le Bris, and J. L. Gentner, "Control of interface formation during growth of InGaAs/InP heterostructures by chloride vapour phase epitaxy," *J. Cryst. Growth*, vol. 79, no. 1–3, pp. 909–913, Dec. 1986.

[7] D. W. Shaw, "Influence of Substrate Temperature on GaAs Epitaxial Deposition Rates," *J. Electrochem. Soc.*, vol. 115, no. 4, p. 405, 1968.

[8] D. W. Shaw, "Epitaxial GaAs Kinetic Studies: {001} Orientation," *J. Electrochem. Soc.*, vol. 117, no. 5, p. 683, 1970.

[9] K. Grüter, M. Deschler, H. Jürgensen, R. Beccard, and P. Balk, "Deposition of high quality GaAs films at fast rates in the LP-CVD system," *J. Cryst. Growth*, vol. 94, no. 3, pp. 607–612, Mar. 1989.

[10] E. Gil-Lafon, J. Napierala, D. Castelluci, A. Pimpinelli, R. Cadoret, and B. Gérard, "Selective growth of GaAs by HVPE: keys for accurate control of the growth morphologies," *J. Cryst. Growth*, vol. 222, no. 3, pp. 482–496, Jan. 2001.

[11] N. D. Nguyen *et al.*, "(Invited) Selective Epitaxial Growth of III-V Semiconductor Heterostructures on Si Substrates for Logic Applications," 2010, pp. 933–939.

[12] K. Tomioka, Y. Kobayashi, J. Motohisa, S. Hara, and T. Fukui, "Selective-area growth of vertically aligned GaAs and GaAs/AlGaAs core–shell nanowires on Si(111) substrate," *Nanotechnology*, vol. 20, no. 14, p. 145302, Apr. 2009.

[13] K. Tomioka, T. Tanaka, S. Hara, K. Hiruma, and T. Fukui, "III/V Nanowires on Si Substrate: Selective-Area Growth and Device Applications," *IEEE J. Sel. Top. Quantum Electron.*, vol. 17, no. 4, pp. 1112–1129, Jul. 2011.

[14] K. L. Schulte, W. L. Rance, R. C. Reedy, A. J. Ptak, D. L. Young, and T. F. Kuech, "Controlled formation of GaAs pn junctions during hydride vapor phase epitaxy of GaAs," *J. Cryst. Growth*, vol. 352, no. 1, pp. 253–257, Aug. 2012.

[15] M. Harrous, L. Chaput, A. Bendraoui, M. Cadoret, C. Pariset, and R. Cadoret, "Phosphine and arsine decomposition in CVD reactors for InP and InGaAs growth," *J. Cryst. Growth*, vol. 92, no. 3–4, pp. 423–431, Oct. 1988.

[16] F. Lassalle, A. Porte, J. L. Laporte, C. Pariset, and M. Cadoret, "Growth of GaInAs/InP by the vapor phase epitaxy hydride method," *Mater. Res. Bull.*, vol. 23, no. 9, pp. 1285–1297, Sep. 1988.

[17] E. Gil-Lafon, J. Napierala, A. Pimpinelli, R. Cadoret, A. Trassoudaine, and D. Castelluci, "Direct condensation modelling for a two-particle growth system: application to GaAs grown by hydride vapour phase epitaxy," *J. Cryst. Growth*, vol. 258, no. 1–2, pp. 14–25, Oct. 2003.

[18] A. Pimpinelli, R. Cadoret, E. Gil-Lafon, J. Napierala, and A. Trassoudaine, "Two-particle surface diffusion-reaction models of vapour-phase epitaxial growth on vicinal surfaces," *J. Cryst. Growth*, vol. 258, no. 1–2, pp. 1–13, Oct. 2003.

[19] J. Leitner, J. Stejskal, V. Flemr, and P. Voňka, "Thermodynamic aspects of the preparation of AlAs and $Ga_{1-x}Al_xAs$ epitaxial layers in hydride and chloride systems," *J. Cryst. Growth*, vol. 144, no. 1–2, pp. 1–8, Nov. 1994.

[20] A. Fontcuberta i Morral, C. Colombo, G. Abstreiter, J. Arbiol, and J. R. Morante, "Nucleation mechanism of gallium-assisted molecular beam epitaxy growth of gallium arsenide nanowires," *Appl. Phys. Lett.*, vol. 92, no. 6, p. 063112, 2008.

[21] C. Colombo, D. Spirkoska, M. Frimmer, G. Abstreiter, and A. Fontcuberta i Morral, "Ga-assisted catalyst-free growth mechanism of GaAs nanowires by molecular beam epitaxy," *Phys. Rev. B*, vol. 77, no. 15, Apr. 2008.

[22] V. G. Dubrovskii, G. E. Cirlin, N. V. Sibirev, F. Jabeen, J. C. Harmand, and P. Werner, "New Mode of Vapor−Liquid−Solid Nanowire Growth," *Nano Lett.*, vol. 11, no. 3, pp. 1247–1253, Mar. 2011.

[23] G. Omanakuttan, S. Stergiakis, A. Sahgal, I. Sychugov, S. Lourdudoss, and Y. T. Sun, "Epitaxial lateral overgrowth of $GaxIn_{1-x}P$ towards coherent GaxIn1−xP/Si heterojunction by hydride vapor phase epitaxy," 2016, pp. 1–2.

[24] F. Glas, M. R. Ramdani, G. Patriarche, and J.-C. Harmand, "Predictive modeling of self-catalyzed III-V nanowire growth," *Phys. Rev. B*, vol. 88, no. 19, Nov. 2013.

[25] F. Matteini, G. Tütüncüoğlu, D. Rüffer, E. Alarcón-Lladó, and A. Fontcuberta i Morral, "Ga-assisted growth of GaAs nanowires on silicon, comparison of surface SiOx of different nature," *J. Cryst. Growth*, vol. 404, pp. 246–255, Oct. 2014.

[26] F. Matteini, G. Tütüncüoglu, H. Potts, F. Jabeen, and A. Fontcuberta i Morral, "Wetting of Ga on SiO_x and Its Impact on GaAs Nanowire Growth," *Cryst. Growth Des.*, p. 150529153811003, May 2015.

[27] G. Koblmüller *et al.*, "Self-induced growth of vertical free-standing InAs nanowires on Si(111) by molecular beam epitaxy," *Nanotechnology*, vol. 21, no. 36, p. 365602, Sep. 2010.

[28] T. Grap, T. Rieger, C. Blömers, T. Schäpers, D. Grützmacher, and M. I. Lepsa, "Self-catalyzed VLS grown InAs nanowires with twinning superlattices," *Nanotechnology*, vol. 24, no. 33, p. 335601, Aug. 2013.

[29] X. Wang, W. Du, X. Yang, X. Zhang, and T. Yang, "Self-catalyzed growth mechanism of InAs nanowires and growth of InAs/GaSb heterostructured nanowires on Si substrates," *J. Cryst. Growth*, vol. 426, pp. 287–292, Sep. 2015.

[30] B. Mandl *et al.*, "Au-Free Epitaxial Growth of InAs Nanowires," *Nano Lett.*, vol. 6, no. 8, pp. 1817–1821, août 2006.

[31] W. M. Haynes, *CRC Handbook of Chemistry and Physics, 95th Edition*. CRC Press, 2014.

[32] C. Chatillon and D. Chatain, "Congruent vaporization of GaAs(s) and stability of Ga(l) droplets at the GaAs(s) surface," *J. Cryst. Growth*, vol. 151, no. 1–2, pp. 91–101, mai 1995.

[33] Breuer, S, Karouta, F., Tan, H.H., and Jagadish, C., "MOCVD growth of GaAs nanowires using Ga droplets," in *IEEE*, Melbourne, VIC, 2012, pp. 39–40.

[34] A. M. Munshi *et al.*, "Position-Controlled Uniform GaAs Nanowires on Silicon using Nanoimprint Lithography," *Nano Lett.*, vol. 14, no. 2, pp. 960–966, février 2014.

[35] S. Ermez, E. J. Jones, S. C. Crawford, and S. Gradečak, "Self-Seeded Growth of GaAs Nanowires by Metal–Organic Chemical Vapor Deposition," *Cryst. Growth Des.*, vol. 15, no. 6, pp. 2768–2774, Jun. 2015.

[36] P. Krogstrup, R. Popovitz-Biro, E. Johnson, M. H. Madsen, J. Nygård, and H. Shtrikman, "Structural Phase Control in Self-Catalyzed Growth of GaAs Nanowires on Silicon (111)," *Nano Lett.*, vol. 10, no. 11, pp. 4475–4482, Nov. 2010.

[37] S. Bietti *et al.*, "Self-assisted GaAs nanowires with selectable number density on Silicon without oxide layer," *J. Phys. Appl. Phys.*, vol. 47, no. 39, p. 394002, Oct. 2014.

[38] G. Priante, S. Ambrosini, V. G. Dubrovskii, A. Franciosi, and S. Rubini, "Stopping and Resuming at Will the Growth of GaAs Nanowires," *Cryst. Growth Des.*, vol. 13, no. 9, pp. 3976–3984, Sep. 2013.

[39] V. G. Dubrovskii, "Group V sensitive vapor–liquid–solid growth of Au-catalyzed and self-catalyzed III–V nanowires," *J. Cryst. Growth*, vol. 440, pp. 62–68, Apr. 2016.

[40] G. Avit *et al.*, "GaN Rods Grown on Si by SAG-HVPE toward GaN HVPE/InGaN MOVPE Core/Shell Structures," *Cryst. Growth Des.*, vol. 16, no. 5, pp. 2509–2513, May 2016.

[41] W. Kaminsky, "From CIF to virtual morphology using the *WinXMorph* program," *J. Appl. Crystallogr.*, vol. 40, no. 2, pp. 382–385, Apr. 2007.

[42] M. Rahimnejad, A. A. Ghoreyshi, G. Najafpour, and T. Jafary, "Power generation from organic substrate in batch and continuous flow microbial fuel cell operations," *Appl. Energy*, vol. 88, no. 11, pp. 3999–4004, Nov. 2011.

[43] K. Rabaey and W. Verstraete, "Microbial fuel cells: novel biotechnology for energy generation," *Trends Biotechnol.*, vol. 23, no. 6, pp. 291–298, Jun. 2005.

[44] K. Rabaey, N. Boon, S. D. Siciliano, M. Verhaege, and W. Verstraete, "Biofuel Cells Select for Microbial Consortia That Self-Mediate Electron Transfer," *Appl. Environ. Microbiol.*, vol. 70, no. 9, pp. 5373–5382, Sep. 2004.

[45] J. P. Busalmen, A. Esteve-Nuñez, and J. M. Feliu, "Whole Cell Electrochemistry of Electricity-Producing Microorganisms Evidence an Adaptation for Optimal Exocellular Electron Transport," *Environ. Sci. Technol.*, vol. 42, no. 7, pp. 2445–2450, Apr. 2008.

[46] N. S. Ramaraja P Ramasamy, "Electrochemical Impedance Spectroscopy for Microbial Fuel Cell Characterization," *J. Microb. Biochem. Technol.*, 2013.

[47] C. GABRIELLI, "Méthodes électrochimiques: Mesures d'impédances," *Tech. Ing. Corros. Vieil.*, no. P2210, 1998.

Résumé

Nous avons proposé d'étudier le potentiel de l'outil d'épitaxie HVPE (Hydride Vapour Phase Epitaxy) pour la croissance de nanofils de GaAs. La morphologie nanofil permet au matériau épitaxié de libérer les contraintes dans le cas de l'hétéroépitaxie et de mettre en œuvre des procédés de croissance sur des substrats à faible coût comme les substrats de silicium. Dans ce contexte, j'ai effectué la croissance auto-catalysée de nanofils et des nanoobjets de GaAs par HVPE sur substrat silicium. La HVPE utilise des molécules de GaCl synthétisées à l'intérieur du réacteur dans la zone en amont du substrat à haute température (T> 700 °C). La décomposition du GaCl est beaucoup plus difficile entre 600 °C et 700 °C. Dans ce manuscrit des calculs thermodynamiques des constantes d'équilibre de formation du gallium liquide sont donnés et analysés. Les rapports de flux atomiques III/V obtenus sont de 11 à 222, bien plus élevés que les rapports utilisés dans procédés MBE et MOVPE. Ce travail expérimental a été couplé à un travail de modélisation théorique. Une étude de la faisabilité d'utiliser un substrat constitué de nanofils de GaAs comme électrode dans une pile microbienne a également été initiée.

Mots clés : nanofils GaAs, croissance auto-catalysée, épitaxie, HVPE, pile microbienne

Abstract

III-V semiconductor nanowires exhibit excellent electrical and optical properties in laterally confined geometry which is very promising for monolithic integration of photonic nanodevices on silicon substrates. Hydride Vapor Phase Epitaxy (HVPE) process growth was therefore developed in this thesis for the growth of GaAs nanowires. This report is organized into two chapters.

The first chapter introduces the state-of-the-art of self-catalyzed GaAs nanowires and nano-structures on silicon substrate. We have demonstrated the growth of self - catalyzed GaAs nanowires by HVPE on un-patterned Si (111) substrates at a low temperature of 600 °C with extremely high GaCl/AsH$_3$ flow ratios. A model that explains well the experimental findings was developed. The second part proposes the design of a Microbial Fuel Cell (MFC) prototype based on GaAs nanowire samples. A MFC prototype based on GaAs nanowire and substrate was developed.

Key words: GaAs nanowires, self-catalyzed growth, Epitaxy, HVPE, Microbial Fuel Cell